

POLITECNICO DI TORINO

Corso di Laurea Magistrale
in Ingegneria Civile Idraulica

Tesi di Laurea Magistrale

**Experimental analysis of extreme wave
groups acting on offshore lighthouses**



Relatore

Alessandro Antonini (University of Plymouth)

Candidato

Matteo Simbola

Correlatore

Cecilia Surace (Politecnico di Torino)

Anno Accademico 2017/2018

Sessione II

This page was intentionally left blank

ABSTRACT

(EN) The main purpose of the following thesis project is the analysis of offshore lighthouses based on natural rocks. Despite the advent of technology and the considerable improvements that have been made to maritime navigation methodologies, lighthouses continue to have an extremely important role. The territory of the United Kingdom, due to its morphology, own a large number of offshore lighthouses that continue to perform their role very well and which are assiduously analysed and verified so that they never cease their service. The department of Coastal Engineering of the University of Plymouth has therefore decided to carry out an experimentation project, called "STORMLAMP", in order to derive the effects of extreme wave groups on offshore structures. The main purpose of the department and the research team was to apply the results to the Eddystone Lighthouse, located about 20-25 km from the south-east coast of Plymouth.

It will be presented in the following document, the experimentation project was based on four main phases. The first phase was the analysis of the climatic conditions affecting the area under examination, for which the necessary information provided by the UK authorities were extracted. Applying the "Peak Over Threshold" (POT) methodology, extreme events were obtained and a laboratory plan was done. Moreover, a specific analysis of the methodologies for the choice of the threshold and time lag was carried out, in order to point out the independent events. This phase was crucial for the goodness of the fitting of the Generalized Pareto Distribution (GPD) and to provide an adequate overview of extreme events. The principles of Froude's similarity, the groups of extreme waves have been organized.

Subsequently, the most appropriate theoretical methodology was developed to undertake the experimentation, therefore reference was made to the available publications on that topic and, obviously, to the theoretical bases on which general hydraulics and maritime engineering are based. Among all, the "New wave theory" stands out and offered the most suitable methods of focusing waves and generate those needed amplitude peaks that could suitably hit the model. An equally important role is given to the "Hilbert-Huang transformation" (HHT), which gave the possibility to perform an accurate analysis of the recorded signals for the various equipment used.

The third phase was the realisation of the model. Also in this case the principles of Froude's similitude was used. The experimentation was performed in a tank of the laboratory of the University of Plymouth, which made available both the necessary equipment and the entire staff for their monitoring and the realisation of the entire model. The instruments used are the pressure transducers, the load cell, a high-speed camera and the thirteen wave gauge that have allowed the continuous observation of the water level in the tank.

The results extracted are:

- Run-up: the use of the high-speed camera and a consequent analysis of the images allowed to generate the run-up variation with time;
- Variation of water level: the wave -gauge allowed to obtain the variation of the water level in the surrounding area to the model with which the analysis could be refined by defining the behaviour of the wave before hitting the structure;
- Forces: the examination of both the force acting in the direction of the wave motion (F_y) and the consequent moment (M_x) were set up.

The experimentation has led to useful conclusions in the field of offshore construction design and the use of "New wave theory" for this type of tests.

(IT) Il seguente progetto di tesi presenta come scopo principale l'analisi di fari offshore fondati su rocce naturali. Nonostante l'avvento della tecnologia e i notevoli miglioramenti che sono stati apportati alle metodologie di navigazione marittima, i fari continuano a svolgere un ruolo estremamente importante. Il territorio del Regno Unito, per via della sua conformazione, è proprietario di un gran numero di fari offshore che continuano a svolgere egregiamente il proprio ruolo e che assiduamente sono oggetto di analisi e verifiche affinché non cessino mai il loro servizio. Il dipartimento di Ingegneria Costiera dell'Università di Plymouth ha pertanto deciso di portare avanti un progetto di sperimentazione, denominato "STORMLAMP", da cui possa derivare un'analisi degli effetti che i gruppi di onde estreme possono apportare alla struttura. Lo scopo principale del dipartimento e del team di ricerca è l'applicazione dei risultati all'Eddystone Lighthouse, sito a circa 20/25 km dalla costa sud-est di Plymouth.

Come verrà presentato nel seguente elaborato, il progetto di sperimentazione è stato fondato su quattro fasi principali. La prima fase è stata l'analisi delle condizioni climatiche che

interessano l'area presa in esame, per cui sono state estratte le informazioni necessarie fornite dalle autorità britanniche. Applicando la metodologia del “*Peak Over Threshold*” (POT), sono stati ricavati gli eventi estremi che necessitassero di un'analisi in laboratorio. Inoltre, è stata svolta un'apposita analisi delle metodologie applicabili alla scelta della soglia e del lasso di tempo affinché gli eventi potessero essere tra loro indipendenti. Tale fase è stata indispensabile per poter garantire un'efficace adattamento della Generalised Pareto Distribution (GPD) e per fornire una panoramica adeguata degli eventi estremi. Grazie ai principi della similitudine di Froude sono stati organizzati i gruppi di onde estreme da testare.

Successivamente è stata elaborata la metodologia teorica più adatta per la sperimentazione da intraprendere, dunque si è fatto riferimento alle pubblicazioni disponibili in merito e, ovviamente, alle basi teoriche su cui l'idraulica generale e l'ingegneria marittima si fondano. Tra tutte spicca la “*New wave theory*”, da cui si è ricavata la metodologia di focalizzazione delle onde per la generazione delle ampiezze di picco con cui sollecitare il modello. Un ruolo altrettanto importante è stato svolto dalla “*Hilbert-Huang transformation*” (HHT), con cui si è potuta eseguire un'accurata analisi dei segnali registrati dalle varie apparecchiature adoperate.

La terza fase è stata la realizzazione del modello. Anche in questo caso ci si è affidati ai principi della similitudine di Froude. La sperimentazione è stata eseguita in una vasca del laboratorio dell'Università di Plymouth, la quale ha messo a disposizione sia le necessarie apparecchiature che l'intero staff per il loro monitoraggio e la realizzazione dell'intero modello. Gli strumenti utilizzati sono i trasduttori di pressione, la cella di carico, una high-speed camera e le tredici wave-gauge che hanno permesso la continua osservazione del livello idrico nella vasca.

I risultati estratti sono:

- Run-up: grazie all'uso della high-speed camera e di una conseguente analisi delle immagini si è potuta ricomporre la variazione temporale del run-up sul modello;
- Variazione del pelo libero: le wave-gauge hanno permesso di ottenere la variazione del pelo libero nell'area circostante al modello con cui si è potuta affinare l'analisi definendo il comportamento dell'onda prima dell'impatto con la struttura;
- Forze: è stata impostata l'analisi sia della forza agente nella direzione del moto dell'onda (F_y) che il momento conseguente (M_x).

La sperimentazione ha portato ad utili conclusioni nel campo della progettazione di costruzioni offshore e sull'uso della "New wave theory".



AKNOWLEDGMENTS

Con questo progetto di tesi si conclude un lungo percorso di cinque anni che mi ha spesso tenuto occupato e lontano dalla mia città.

In primo luogo sento necessario ringraziare la mia famiglia, mio padre, mia madre e mia sorella. Nonostante il percorso sia stato impegnativo mi sono sempre sentito fortunato per il loro sostegno e per aver sempre creduto in me e nei miei obiettivi.

Vorrei ringraziare la mia ragazza, Paola, che oramai da 9 anni mi affianca su ogni scelta e in ogni momento di difficoltà. Non ho trovato solo una ragazza ma una persona su cui ciecamente contare, più volte dimostrando di essere sempre la prima a credere in me.

Con grande piacere ringrazio il mio relatore, professor Alessandro Antonini, che mi ha pienamente coinvolto nel progetto di ricerca che ho intrapreso ed è riuscito a trasmettermi la passione per questo lavoro. Alla stessa maniera ringrazio la professoressa Cecilia Surace per il supporto nel periodo all'estero e l'intero staff del Coastal Engineering Department dell'University of Plymouth che mi ha dato la grande occasione di lavorare in questo progetto.

Gli anni di studio mi hanno tenuto lontano da molti amici e colleghi ma ugualmente mi hanno permesso di incontrarne di nuovi. Pertanto vorrei fare un ringraziamento generale a tutti coloro che mi sono stati vicino, anche se per poco tempo, contribuendo positivamente a questo mio percorso.

TABLE OF CONTENT

ABSTRACT	III
ACKNOWLEDGMENTS	VII
TABLE OF CONTENT	VIII
LIST OF TABLES	X
LIST OF FIGURES.....	XI
CHAPTER I: INTRODUCTION	1
1.0 Lighthouse History	1
1.1 Technical Aspects	2
1.1.0 Structural Features.....	2
1.1.1 The Lights in Lighthouses.....	3
1.1.2 The Importance of Lighthouses.....	4
1.2 Eddystone Rocks	4
1.3 Main Purposes	7
CHAPTER II: WAVE CLIMATE	9
2.0 Introduction	9
2.1 Theoretical Basis	9
2.1.0 Extreme Values Analysis (EVA)	9
2.1.1 Block Annual Maxima	11
2.1.2 Peaks Over Threshold (POT)	13
2.2 Data Analysis and Results.....	16
CHAPTER III: THEORETICAL BASIS.....	23
3.0 Hydraulic Modelling	23
3.0.1 Dimensional Homogeneity.....	23
3.0.2 Similarity with Froude Constant	24
3.1 Progressive Small-Amplitude Waves.....	26
3.1.1 Characteristics of Progressive Waves	26
3.1.2 Kinematics of Wave Motion	27
3.2 Wave Forces	30
3.2.1 Steady Flow Term	32
3.2.2 Unsteady Flow Term.....	33
3.2.3 The Morison Equation.....	34
3.2.4 Oumeraci Theory.....	35
3.3 New Wave	38
3.4 Methods of Data-Analysis.....	41
3.4.1 The Empirical Mode Decomposition (EMD).....	41
3.4.2 The Ensemble Empirical Mode Decomposition (EEMD)	44
3.4.3 The Duhamel Integral.....	46

CHAPTER IV: PHYSICAL MODELLING	53
4.0 Laboratory Set-up	53
4.1 Results	62
4.1.1 Wave Gauges and Run-Up	64
4.1.2 Forces and Load Distribution	68
CHAPTER V: CONCLUSIONS	75
APPENDIX A: MATLAB CODES	77
REFERENCES	85

LIST OF TABLES

Table 1: Monthly percentage of availability hourly significant wave height measurements of buoy 62103.....	17
Table 2: Parameters estimated.....	21
Table 3: Scale size factors.....	25
Table 4: Dynamic parameters of the model	46
Table 5: Wave gauges characteristics	56
Table 6: Load cell calibration matrix	57
Table 7: Focus positions adopted for the tests	62
Table 8: Test plan for a peak period of 1.2 seconds	63

LIST OF FIGURES

Figure 1: Pharos of Alexandria, Egypt	1
Figure 2: Fresnel Lens	4
Figure 3: Map of Lighthouses in UK.....	5
Figure 4: Section of Smeaton's Tower.....	6
Figure 5: The five lighthouses built on the Eddystone Rocks	7
Figure 6: Example of a time series of significant wave height (Caires, 2011).....	10
Figure 7: Example of identification of extreme values above a threshold (Caires, 2011)	14
Figure 8: Directional waverider buoy (left), wind measurement (right)	16
Figure 9: Wind from direction relative true north, from 2009 to 2016 (EMODnet).....	17
Figure 10: Time series of the available H_s and T_m measurements of buoy 62103	18
Figure 11: Quality check process	19
Figure 12: Variation of the estimates of σ , ξ and 1/50yr H_s return values.....	20
Figure 13: Empirical plot of the quantiles of the data versus the quantiles of the distribution	20
Figure 14: Progressive wave (McCormick, 2010).....	27
Figure 15: Water particle velocities and accelerations (Dean & Darlymple, 2008).....	28
Figure 16: Variation of hyperbolic functions (Atzeni, 2011)	29
Figure 17: Elliptical form of water trajectory (Dean & Darlymple, 2008)	30
Figure 18: Particle trajectory with different depths (Dean & Darlymple, 2008).....	30
Figure 19: Potential flow around the cylinder (Dean & Darlymple, 2008).....	31
Figure 20: Calculation of the steady flow's horizontal component (Dean & Darlymple, 2008).....	32
Figure 21: Measured pressure distributions around cylinders (Dean & Darlymple, 2008)	33
Figure 22: Inertia coefficient (Dean & Darlymple, 2008).....	34
Figure 23: Splash due to breaking waves impact (Wienke & Oumeraci, 2005)	35
Figure 24: Definition sketch of the group of planes (Wienke & Oumeraci, 2005).....	36
Figure 25: Curling factor λ against yaw angle α (Wienke & Oumeraci, 2005).....	37
Figure 26: Oblique impact (Wienke & Oumeraci, 2005).....	37
Figure 27: Ocean surface elevation at a given point (Tromans, Anaturk, & Hagemeyer, 1991).....	39

Figure 28: Most probable extreme surface displacement (Tromans, Anaturk, & Hagemeyer, 1991).....	40
Figure 29: Evolution of the expected ocean surface elevation in space and time (Tromans, Anaturk, & Hagemeyer, 1991).....	40
Figure 30: Example of test data (Huang & Shen, 2014)	41
Figure 31: The data with upper and lower envelopes (Huang & Shen, 2014).....	42
Figure 32: The original data (blue) and the residue (red) (Huang & Shen, 2014).....	43
Figure 33: Representation of the n -empirical modes (Huang & Shen, 2014)	44
Figure 34: EMD application on data affect by noise (Huang & Shen, 2014).....	45
Figure 35: The prototype single degree of freedom (Fabula, 1957)	46
Figure 36: Free vibration of the model.....	47
Figure 37: Generic impulse time series (Fabula, 1957)	47
Figure 38: Half-sine wave impulse (Fabula, 1957).....	48
Figure 39: Rectangular impulse (Fabula, 1957).....	48
Figure 40: Triangular shape impulse (Fabula, 1957)	49
Figure 41: Generic triangular impulse shape (Fabula, 1957).....	49
Figure 42: Impulse shapes comparison (Fabula, 1957).....	50
Figure 43: Description of the Duhamel integral (Fabula, 1957)	50
Figure 44: Wave tank cross-section scheme (not scaled)	53
Figure 45: Shoal characteristics of the first tests carried out	53
Figure 46: Shoal cross-section scheme (not scaled).....	54
Figure 47: Photo of the shoal in the laboratory tank	54
Figure 48: Scaled model of the lighthouse.....	55
Figure 49: Photo of the model fixed with steel beams	55
Figure 50: Wave gauges positioning scheme	56
Figure 51: Photos of the wave gauges set-up.....	57
Figure 52: Load cell installation above the model	58
Figure 53: High speed imaging Fastcam SA4.....	58
Figure 54: Frame of the calibration process with the chessboard	59
Figure 55: Intrinsic parameter transformation (Matlab)	60
Figure 56: Camera intrinsic matrix and pixel skew (Matlab)	60
Figure 57: Radial and tangential distortion of the lenses (Matlab)	60
Figure 58: Undistorted frame with example of run-up on the model.....	61

Figure 59: Comparison between Pierson-Moskowitz ($\gamma = 1$) and Jonswap spectrum ($\gamma = 3.3$).....	63
Figure 60: Comparison of wave-gauges data ($T_p = 1.2$ s, $\gamma = 1$, crest focus, central shelf)	64
Figure 61: Run-up plot ($T_p = 1.96$ s, $\gamma = 1$, trough focus, toe11).....	65
Figure 62: Comparison of run-up and WG6 ($T_p = 1.85$ s, $\gamma = 1$, trough focus, toe back slope).....	65
Figure 63: Comparison between run-up and wave gauge 6 against peak period	66
Figure 64: Run-up/maximum wave crest high vs water depth/peak wave length (2D)	67
Figure 65: Run-up/maximum wave crest high vs water depth/peak wave length (3D)	67
Figure 66: Run_n_01, force/moment and wave gauge against frequency.....	68
Figure 67: Run_n_01, wave gauge and force comparison	69
Figure 68: Run_n_01, correction applied on the force and bending moment	70
Figure 69: Run_n_01, components of the Hilbert transformation and residual signal.....	70
Figure 70: Run_n_01, signal decomposition according to the HHT (first attempt).....	71
Figure 71: Run_n_01, signal decomposition according to the HHT (second attempt)	72
Figure 72: Run_n_01, comparison after the correction of the raw signal	73

CHAPTER I: INTRODUCTION

1.0 Lighthouse History

Many years ago, people decided to explore the waters by boat. During the day they could find their way back to the landing place by looking for a pile of rocks that had been left there. But how could they find their way home at night? Since much of the shore-line looked very similar, friends had to light a bonfire on a high point to guide them to the right landing area. Our first lighthouses were actually given to us by Nature herself; sailors sometimes used landmarks such as glowing volcanoes to guide them. One of the Seven Wonders of the Ancient World as a lighthouse: the famous *Pharos of Alexandria*, Egypt. It is the first one that is recorded in history. Those records tell us that it was the tallest one ever built (137 meters about) and used an open fire at the top as a source of light.



Figure 1: Pharos of Alexandria, Egypt

It would seem superfluous but we should wonder: what is a lighthouse? It is a high tower with a bright light at the top, located at an important or dangerous place regarding navigation. The two main purposes of a lighthouse are to serve as navigational aid and to warn boats of dangerous areas. It is like a traffic sign on the sea. Lighthouses can be found in a variety of places, on rocky cliffs or sandy shoals on land, on a wave swept reef in the sea, and at entrances to harbours and bays. During the middle age times, Roman lighthouses

fell into disuse, but, as navigation improved, lighthouses gradually expanded into Western and Northern Europe. One of the oldest working in Europe is Hook Lighthouse located in Ireland.

The United Kingdom is a big island which concentrates a large percentage on sea trade, therefore the process of lighting its coastal areas is one that has been continuing since the Dark Ages. The administration of all the lighthouses, buoys and beacons of England, Wales and Scotland is the responsibility of just two organisations: the Corporation of Trinity House and the Commissioners of Northern Lighthouses. By far the elder of the two is Trinity House, which is empowered to construct and maintain the buoys, beacons and lighthouses around the coasts of England and Wales. Sadly, many details of the early history of Trinity House have been lost owing to the devastations of the Civil War and the Great Fire of London. However, it is probable that the organisation as we know it evolved from one of the seaman's guilds or associations which were in existence in the Middle Ages.

The modern era of lighthouses began at the turn of the 18th century, as lighthouse construction boomed in lockstep with burgeoning levels of transatlantic commerce. Advances in structural engineering and new efficient lighting equipment allowed for the creation of larger and more powerful lighthouses.

1.1 Technical Aspects

1.1.0 Structural Features

The nature and intensity of external forces in a large measure dictate the materials of construction. The forces expected to be encountered also depend on the geographic location of the site. Super-structures are made of granite, brick, skeleton steel structures and reinforced concrete. One aspect of the type of foundation to be used is dictated by the depth of water which is encountered. The superstructure in combination with the subsoil conditions governs the type of foundation to be used: screw pile foundations or gravity foundations. Wave swept structures are located on sites where wave action must be taken into consideration; two general types have been successfully used: solid masonry towers, wherein the mass of masonry counteracts the external forces created by wave and wind actions, and open skeleton towers, so designed that the structure offers the least possible resistance to the kinetic energy produced by the waves (Nicholson, 1988).

1.1.1 The Lights in Lighthouses

The first lights were beacon fires, lit on hillsides and later in towers or church towers. The light was non constant and they produced a lot of smoke. Early lighthouses also used wood but gradually they switched to coal which produced less smoke and give a more consistent light. At that time a single lighthouse could consume 300 tons or more of coal a year.

The Argand lamp, invented by Aimé Argand, revolutionized lighthouse illumination with its steady smokeless flame. This was an oil lamp that had a steady smokeless flame. This worked by having a circular wick and air going up the centre and outside, inside a glass chimney, allowing better combustion. In 1901 the vaporised oil burner was invented by Arthur Kitson, and later improved by David Hood at Trinity House, Tizio et al., 2015. The light produced was six times the brightness of previous lights. This burner worked by burning vaporizing kerosene under pressure mixed with air through an incandescent mantle. South Foreland Lighthouse was the first to successfully use an electric light in 1875 (Nicholson, 1988).

Lighthouse optics really started with the Argand lamp, which was the first reliable and predictable light form, with the first practical lighthouse system in 1777 developed by William Hutchinson from Liverpool. Known as the catoptric system, it comprised a parabolic reflector concentrating light into a beam. This was achieved by a large number of small pieces of silvered glass (mirrors). This lasted well. Next came polished metal versions that were brighter and cheaper to produce but deteriorated quickly. The Fresnel catadioptric system was a step forward. French physicist and engineer Augustin-Jean Fresnel developed the multi-part Fresnel lens for use in lighthouses. His design allowed for the construction of lenses of large aperture and short focal length, without the mass and volume of material that would be required by a lens of conventional design. A Fresnel lens can also capture more oblique light from a light source, thus allowing the light from a lighthouse equipped with one, to be visible over greater distances.

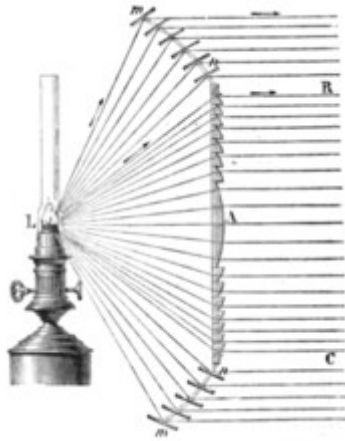


Figure 2: Fresnel Lens

In recent times, many Fresnel lenses have been replaced by rotating aerobeacons which require less maintenance. In modern automated lighthouses, this system of rotating lenses is often replaced by a high intensity light that emits brief omnidirectional flashes (concentrating the light in time rather than direction). These lights are similar to obstruction lights used to warn aircraft of tall structures. Recent innovations are "Vega Lights", and initial experiments with *light-emitting diode* (LED) panels.

1.1.2 The Importance of Lighthouses

It is well known that 95 percent of the UK's international trade is transported by sea. Although mariners are making ever greater use of satellite based navigation technologies, lighthouses continue to have a crucial role to play in safety navigation. We all know computers can crash very easily, some solar activities can affect GPS, there's a lot of reasons why technologies can fail.

1.2 Eddystone Rocks

There are many lighthouses around the UK, as we can see in Figure 3, and almost 20 of them are frequently exposed to wave action. The Eddystone Lighthouse is the one generally regarded as the most famous lighthouse in the world. It is located on the dangerous Eddystone Rocks which were so feared by mariners entering the English Channel that they often hugged the coast of France to avoid the danger.



Figure 3: Map of Lighthouses in UK

The first lighthouse on Eddystone Rocks was an octagonal wooden structure built by Henry Winstanley. It survived its first winter but was in need of repair, and was subsequently changed to a dodecagonal stone clad exterior on a timber framed construction with an octagonal top section as can be seen in Figure 5. This stone-clad wooden structure was swept away by the great storm of 1703.

Following the destruction of the first lighthouse, Captain John Lovett acquired the lease of the rock and commissioned John Rudyerd to design the new lighthouse, built as a conical wooden structure around a core of brick and concrete. On the night of 2 December 1755, the top of the lantern caught fire, probably through a spark from one of the candles used to illuminate the light.

During the life of Rudyerd's tower, the ownership of Eddystone had changed hands. Since 1724 the chief shareholder was Robert Weston. Determined to have a structure that would out-last the previous three, he contacted the Royal Society to ask their advice as to its constructor. Without hesitation they at once recommended one man who, as a result of his efforts on the Eddystone, was to change the whole science of pharology in years to come. His name was John Smeaton. Study of Winstanley's and Rudyerd's towers led him to the conclusion that his two main problems would be to make sure that the structure was heavy

enough to resist any displacement by the waves, and also strong enough to prevent it vibrating during times of storm. To overcome these problems, he had taken a bold decision early in his planning, namely, to build his tower entirely out of the stone. Rather than repeating Rudyerd's design of a sloping cylinder, he enlarged the diameter of the base and made the tower sides slope inwards in a concave curve, gradually becoming nearer to parallel as the height increased. This was a design of rare perception, a design which was to make the name of Smeaton legend amongst future lighthouse engineers.

Smeaton's lighthouse was 18 m high and had a diameter at the base of 8 m and at the top of 5 m. In 1841 major renovations were made and it continued in use until 1877 when it was discovered that rocks upon which it stood were becoming eroded. Each time large waves struck the lighthouse it shook from side to side.

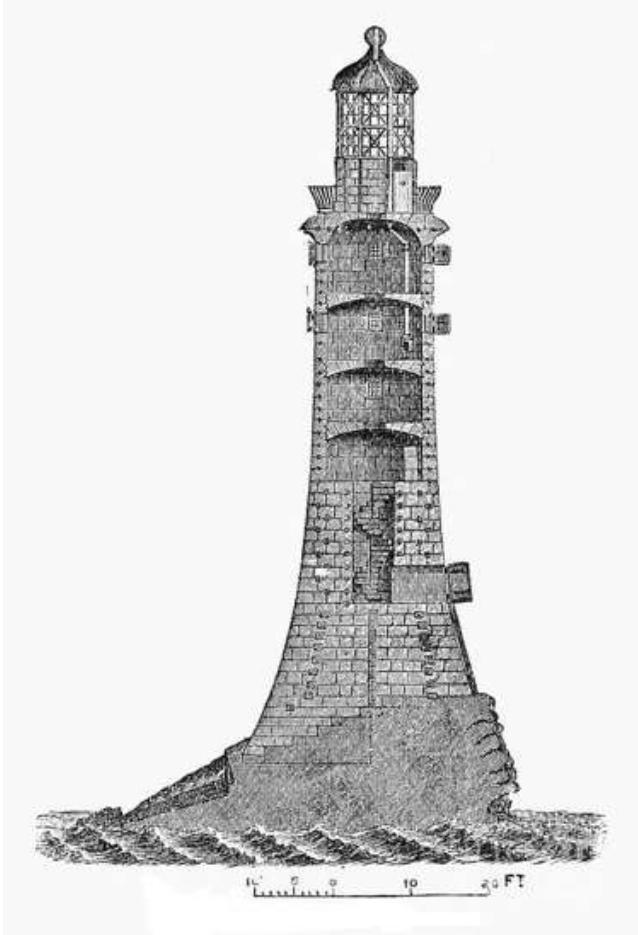


Figure 4: Section of Smeaton's Tower

Smeaton's lighthouse was rebuilt on Plymouth Hoe as a memorial and nowadays it represents one of the most important monuments of the city of Plymouth. The foundations of the tower remain, close to the new and more solid foundations of the current lighthouse.

At the beginning of the 19th century, the lighthouse was visited on several occasions by Robert Stevenson, Chief Engineer to the Northern Lighthouse Board in Edinburgh. On one of these visits signs became apparent that all might not be well with the tower. The situation was obviously serious; nearly 1000 tons of granite were resting on a piece of rock that was slowly but surely being eaten away by the sea.

The current, fourth, lighthouse was designed by James Douglas and it is the largest tower to be built on the reef, standing some 30 meters above sea level. The light was lit in 1882 and is still in use. The tower has been changed by construction of a helipad above the lantern, to allow maintenance crews access, (Nicholson, 1988).

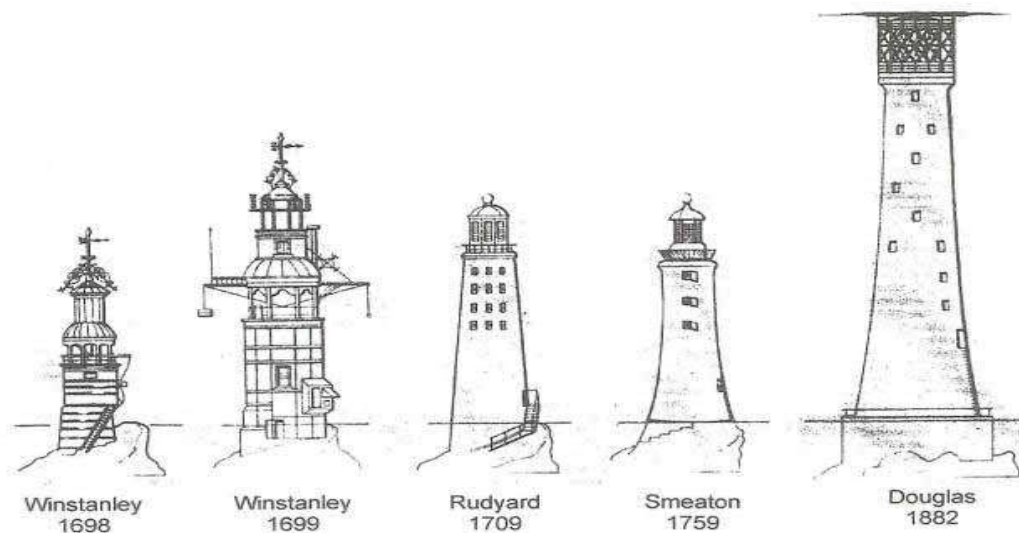


Figure 5: The five lighthouses built on the Eddystone Rocks

1.3 Main Purposes

The following thesis project aims at the analysis of extreme wave groups acting on offshore lighthouses built on natural rocks. The effects that extreme wave groups have on offshore structures are numerous and all of them deserve a separate analysis. The tests have been carried out in the laboratory of Coastal Engineering of the University of Plymouth. Although the instruments used during the experimentations were many, thus lots of information were extracted, this thesis is focused on the analysis of effects of the run-up on the structure.

The experimentations treated are part of an important research project carried out by the Coastal Engineering department of the University of Plymouth, called STORMLAMP (STructural behaviour Of Rock Mounted Lighthouses At the Mercy of imPulsive waves). In this particular case, the tests performed follow an initial thesis project where only the two dimensional effects of interaction between waves and structure were considered.

CHAPTER II: WAVE CLIMATE

2.0 Introduction

In coastal environment waves, tides, currents and winds are the important parameters, which need to be considered for any developments. In many situations, wave is the single most important parameter which influences design considerations. The wind energy in the offshore region is transported to the coast in the form of waves, which constantly agitate the coastal region. The waves cause dynamic impact on coastal structures, which they must withstand. Also, the waves influence navigation of ships, as well as ship motions at berth affecting the operations of berths. At the coast, the waves result in movement of sand along the shore causing erosion or accretion of the shoreline. The waves stir up the sediments at the bed and bring them into suspension, which are transported by currents, which may lead to siltation in harbours and approaches. Therefore, understanding of the mechanism of waves is important to coastal engineers (Vaidya).

A coastal structure must remain standing when hit by the most severe waves, currents, and winds that can reasonably be expected during its intended lifetime. Waves, currents and winds are basic elements of the physical environment. In this structural sense, good coastal engineering is always sensitive to the environment (Galvin, 1982).

2.1 Theoretical Basis

2.1.0 Extreme Values Analysis (EVA)

Design conditions are expressed in terms of the structure's performance under unusual or 'extreme' conditions. It is often the case that an offshore structure is designed to resist a condition so unusual that no similar condition may be found in available measurements or records. One way to proceed is to fit a probability distribution to the measurements and extrapolate this to find the conditions corresponding to the rarity of the required event. The range of probability distributions that are used for design and the methods for fitting them to the measurements have been the subject of much study.

All these variables are continuous functions of time. However, measurements are taken at fixed intervals resulting in a discrete set of values over time, or, a time series. Typically, wave and water level records are available at hourly or three-hourly intervals, although this can vary according to the instrument and processing adopted. Suppose we have a time series of significant wave heights (Figure 6).

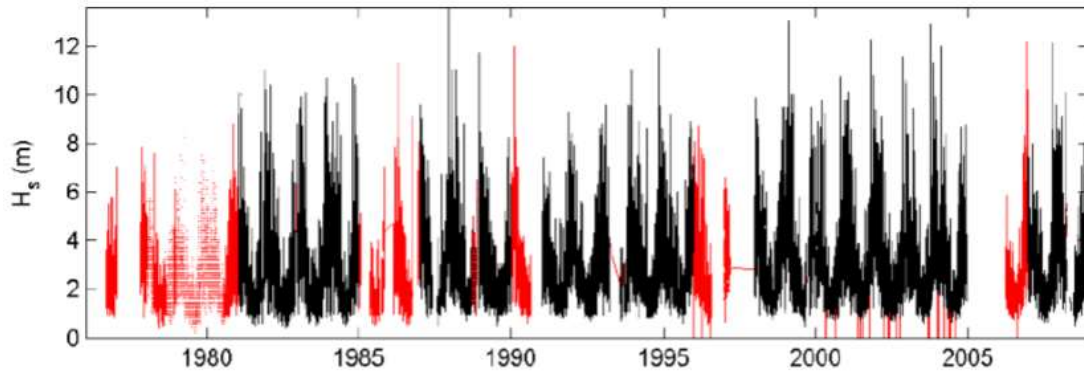


Figure 6: Example of a time series of significant wave height (Caires, 2011)

Each point of the time series can be considered to be an individual event with duration equal to the interval between successive points. For many of the statistical manipulations it is required that the events are independent. A convenient check is to calculate the autocorrelation function of the time series; if this drops rapidly from its value of 1 at zero lag, then the assumption that events are independent is reasonable (Reeve, Chadwick, & Fleming, 2004).

Considering a time series of values that we take as being random and independent, and which have the same distribution at each time point. The distribution of the maximum of a sequence of size N is the Generalised Extreme Value distribution (GEV). The asymptotic behaviour of the distribution of maximum values was investigated by Fisher and Tippett (1928) who found three types of limiting distribution. The GEV encompasses all three types. The only requirement is that values that are well separated in time are approximately independent. These conditions are typically satisfied by all sea variables. If X obeys the GEV (μ, σ, δ) distribution it has the distribution function

$$P(X \leq x) = \exp \left\{ - \left[\frac{1 - \delta(x - \mu)^{\frac{1}{\delta}}}{\sigma} \right] \right\} \quad [2.1]$$

where

μ : location parameter;

σ : scale parameter;

δ : shape parameter.

The level, x_p , exceeded with probability P , i.e. $P(X > x_p) = P$, is given by

$$x_p = \mu + \sigma \left\{ \frac{[\log(1 - P)^\delta + 1]}{\delta} \right\} \quad [2.2]$$

Two limiting distributions that are often used instead of the GEV distribution, but which are special cases of the GEV distribution are the Weibull and Gumbel distributions. These correspond to $\delta > 0$ and $\delta = 0$ respectively.

If x follows the 2-parameter Weibull distribution it obeys

$$F(x) = 1 - e^{-\left(\frac{x}{\lambda}\right)^k} \quad [2.3]$$

And if it follows the Gumbel distribution it obeys

$$F(x) = e^{-e^{-\frac{(x-u)}{\xi}}} \quad [2.4]$$

And if it follows the 3-parameter Weibull distribution it obeys

$$F(x) = 1 - e^{-\left(\frac{x-\theta}{\lambda}\right)^k} \quad [2.5]$$

In the above, u and θ are location parameters, λ and ξ are scale parameters that are greater than zero, and k is a shape parameter.

The theoretical justification for the GEV provides a basis for extrapolation beyond the data to long return period events; however, its biggest drawback is that it is wasteful of data when applied to annual maxima. The number of data points on which to fit the distribution corresponds to the number of years of data, often a few tens of points. Smith (1986) developed a means of using the largest values in a year to mitigate this problem to some extent. An alternative approach is to use all the large values in the sequence, not just the annual maximum observations (Reeve, Chadwick, & Fleming, 2004).

Thus, two different methods could be applied: the block annual maxima and the peaks over threshold (POT).

2.1.1 Block Annual Maxima

In order to explain the basic ideas, let's define $M_n = \max\{X_1, \dots, X_n\}$, where X_1, X_2, \dots, X_n is a sequence of independent random variables having a common distribution function F . In its simplest form, the *extremal types theorem* states the following: if there exist sequences of constants $\{\sigma_n > 0\}$ and $\{\mu_n\}$ such that $P\{\sigma_n M_n + \mu_n \leq z\} \rightarrow G(z)$ as $n \rightarrow$

∞ , where G is a *non-degenerate cumulative distribution function*¹, then G must be a generalized extreme value (GEV) distribution, which is given by

$$G(z) = \begin{cases} \exp\left\{-\left[1 + \xi\left(\frac{z - \mu}{\sigma}\right)\right]^{-\frac{1}{\xi}}\right\}, & \text{for } \xi \neq 0 \\ \exp\left\{-\exp\left[-\left(\frac{z - \mu}{\sigma}\right)\right]\right\}, & \text{for } \xi = 0 \end{cases} \quad [2.6]$$

where z take values in three different sets according to the sign of ξ : $z > \mu - \sigma/\xi$ if $\xi < 0$ (the domain of z has a lower bound), $z < \mu - \sigma/\xi$ if $\xi < 0$ (the domain of z has an upper bound), and $-\infty < z < \infty$ if $\xi = 0$.

In other words, if the sequence of distribution functions of (normalizations of) the maximum value in a random sample of size n converges to a (single) distribution function as n tends to infinity, then that distribution function must be a GEV distribution. Moreover, this and other results of extreme value theory hold true even under general dependence conditions (Coles, 2001).

One of the main applications of extreme value theory is the estimation of the once per m year (1/ m -yr) return value, the value which is exceeded on average once every m years. The 1/ m -yr return value based on the Annual Block Maxima method, z_m , is given by

$$z_m = \begin{cases} \mu - \frac{\sigma}{\xi} \left(1 - \left\{-\log\left(1 - \frac{1}{m}\right)\right\}^{-\xi}\right), & \text{for } \xi \neq 0 \\ \mu - \sigma \ln\left\{-\log\left(1 - \frac{1}{m}\right)\right\}, & \text{for } \xi = 0 \end{cases} \quad [2.7]$$

The sample sizes of annual maxima data are usually small, so that model estimates, especially return values, have large uncertainties. This has motivated the development of more sophisticated methods that enable the modelling of more data than just block maxima. These methods are based on two well-known characterizations of extreme value distributions: one based on exceedances of a threshold, and the other based on the behaviour of the r largest, for small values of r , observations within a block.

¹ A distribution function is said to be degenerate if it allocates probability 1 to a single point.

2.1.2 Peaks Over Threshold (POT)

In this work, the Peak Over Threshold method has been applied having a good number of daily measures. The POT (peak over threshold) method provides a soundly based solution to extrapolation problems. The method is particularly suited for dealing with realizations of stochastic processes which is approximately stationary or can be split in stationary parts. It consists of fitting the GPD (Generalized Pareto Distribution) to the peaks of clustered excesses over a threshold, defined as amount by which observations exceed a given threshold, and calculating return values (Ferreira & Guedes Soares, 1998).

Under very general conditions this procedure ensures that the data can have only three possible distributions (the three forms of the GPD given below) and, moreover, that observations belonging to different peak clusters are approximately independent. In the POT method, the peak excesses over a high threshold u of a time series are assumed to occur in time according to a Poisson process with rate λ_u and to be independently distributed as a GPD, whose distribution function is given by

$$F_u(y) = \begin{cases} 1 - \left(1 + \xi \frac{y}{\sigma_u}\right)^{-\frac{1}{\xi}}, & \text{for } \xi \neq 0 \\ 1 - \exp\left(-\frac{y}{\sigma_u}\right), & \text{for } \xi = 0 \end{cases} \quad [2.8]$$

The two parameters of the GPD are called the scale (σ_u) and shape (ξ) parameters. When $\xi = 0$ the GPD is said to have a type I tail and amounts to the exponential distribution with mean σ_u ; when $\xi > 0$ it has a type II tail and it is the Pareto distribution; and when $\xi < 0$ it has a type III tail and it is a special case of the beta distribution (Caires, 2011). If $\xi < 0$, as it has been seen in the GEV, the support of the GPD was an upper-bound, $-\tilde{\sigma}/\xi$, which is defined as the upper end-point of the GPD. Thus, since in the equation [2.8] $x < -\sigma_u/\xi$ when $\xi < 0$, all the extreme values u modelled by the GPD cannot be greater than $-\sigma_u/\xi$. Consequently, it means that the variable of interest is

$$x^* = u - \frac{\sigma_u}{\xi} \quad [2.9]$$

The quantity x^* is to be thought such as the upper-limit of the variable of interest (e.g. of H_s).

The 1/m-yr return value based on a POT/GPD analysis, z_m , is given by

$$z_m = \begin{cases} u + \frac{\sigma_u}{\xi} \{(\lambda_u m)^\xi - 1\}, & \text{for } \xi \neq 0 \\ u + \sigma_u \log(\lambda_u m), & \text{for } \xi = 0 \end{cases} \quad [2.10]$$

The equation [2.10] is obtained from the [2.8] solving $1 - F(y) = 1/(\lambda_u m)$ for y and then adding the threshold u to the result.

If previously it has been possible to identify a probability distribution associate to the maximum annual values (GEV), in this case it is possible to identify and introduce a probability distribution that can be adapted to all values that exceed the defined threshold u . According to the two methods, POT and Block Maxima, the parameters of the distributions are actually correlated. In particular, the same parameter is the same for the GEV and GPD while the two scale parameters are related by the following equation

$$\sigma_u = \sigma + \xi(u - \mu) \quad [2.11]$$

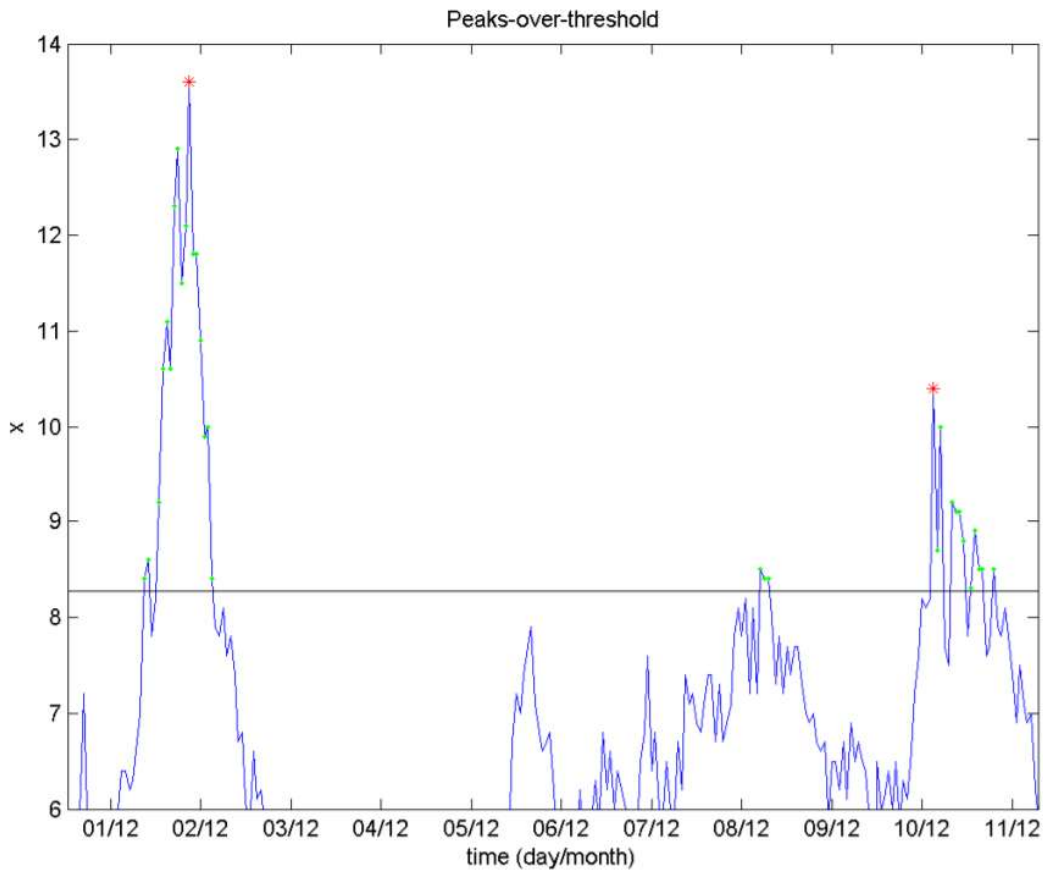


Figure 7: Example of identification of extreme values above a threshold (Caires, 2011)

As previously mentioned, one of the fundamental aspects in the application of this method is the independence of the various elements extracted from the original data. Therefore, a declustering method is applied. The extracted peaks are unified within independent groups so that all the values that falls in the same group can be considered to be related to the same meteoric event. These groupings could be done also in terms of time steps, in the following analysis a reference of 48 hours was considered in order to define two successive peaks independently. Figure 7 shows the procedure for identifying the clusters (storms).

Secondly, the choice of the threshold must be made in an accurate manner. This choice represents a trade off between bias and variance: a threshold that is too low violates the asymptotic behaviour shown in the model, leading to bias; a too high threshold would generate fewer extremes with which to estimate the model, leading to high variance.

An important property of the POT method is the stability of the threshold, in fact if the GPD is a good approximation for the extremes extracted according to a threshold u_0 then a GPS can equally be applied for a threshold $u > u_0$. Furthermore, assuming that the two distributions have the same shape parameter, it is possible to derive the following relation between scale parameters

$$\sigma_u = \sigma_{u_0} + \xi(u - u_0) \quad [2.12]$$

that can be re-written such as

$$\sigma^* = \sigma_u - \xi u \quad [2.13]$$

Subsequently, once the threshold u_0 has been found, the scale and shape parameters tend to remain constant for higher threshold values. This approach is often used to identify the minimum threshold to extract the maximum number of extreme events.

An alternative method for fitting the data to the GPD is the r-largest method. It is not commonly used in the most common costal engineering practises, it briefly consists of extracting the r-largest values per year and fitting the r-largest distribution (Coles, 2001). The choice of r is analogous to the choice of threshold in the POT method.

Finally, at the end of this theoretical part of the chapter, it is worth pointing out that the analyses made so far only refer to stationary events, so not variable with time. Therefore, it is a notable simplification, but, for further applications, it is however possible to take into

account the non-stationary of the phenomena by imposing the time dependence of the various parameters.

2.2 Data Analysis and Results

The data used for the following analyses were extracted from EMODnet (www.emodnet-physics.eu/map/) from buoy 62103 (Latitude: 49.9N, Longitude: 29W) in NetCDF format. The European Marine Observation and Data Network (EMODnet) is a network of organisations supported by the EU's integrated maritime policy. These organisations work together to observe the sea, process the data according to international standards and make that information freely available as interoperable data layers and data products.

Unfortunately, marine data collection, storage and access in Europe has been carried out in a fragmented way for many years. Most data collection has focused on meeting the needs of a single purpose by a wide range of private and public organisations, often in isolation from each other. For this reason, the analysis have been performed considering the buoy 62103 since it is the only one with an effective number of information in order to carry out a good analysis of extreme wave heights.



Figure 8: Directional waverider buoy (left), wind measurement (right)

The information given by the database are numerous but only some of them are useful for the purposes of the following approach. The wave propagation can be initially defined by the wind distribution and its intensity near the considered area.

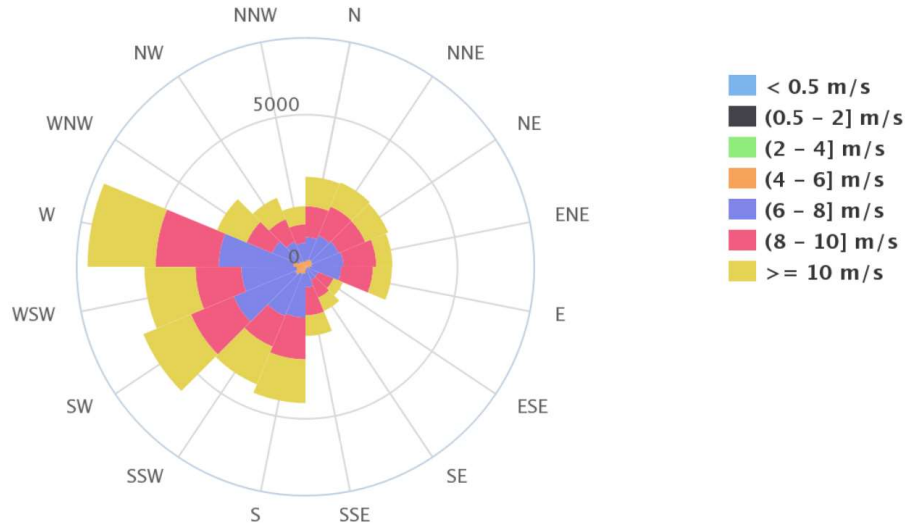


Figure 9: Wind from direction relative true north, from 2009 to 2016 (EMODnet)

Figure 9 is only a general presentation of the sea behaviour, the most important information is clearly provided by the temporal variation of the wave heights recorded.

Data is available from 2007 to 2017 but with few gaps. The following table (Table 1) gives the percentage of availability hourly measurements obtained.

	Jan	Feb	Mar	Apr	May	Jun	Jul	Aug	Sep	Oct	Nov	Dec
2007	0.00%	0.00%	0.00%	0.00%	100.00%	11.11%	80.65%	0.00%	99.86%	100.00%	100.00%	100.00%
2008	99.46%	100.00%	99.87%	100.00%	98.92%	99.44%	99.46%	99.60%	99.31%	99.87%	100.00%	99.33%
2009	100.00%	100.00%	99.46%	99.17%	100.00%	100.00%	100.00%	94.76%	99.58%	99.87%	99.86%	99.60%
2010	98.25%	99.85%	90.73%	92.22%	99.87%	96.67%	98.39%	98.79%	98.19%	100.00%	99.72%	98.92%
2011	99.46%	100.00%	100.00%	99.86%	99.46%	100.00%	98.66%	100.00%	100.00%	96.91%	95.97%	98.25%
2012	99.46%	97.56%	90.99%	96.67%	93.15%	91.67%	92.47%	95.70%	99.72%	100.00%	99.72%	98.39%
2013	99.60%	98.07%	97.04%	99.86%	99.60%	98.61%	97.85%	95.03%	97.50%	95.70%	82.50%	80.78%
2014	95.56%	95.83%	92.61%	95.00%	90.59%	97.08%	96.10%	96.77%	96.25%	95.30%	99.86%	96.77%
2015	98.92%	99.26%	96.51%	99.86%	96.77%	99.72%	96.64%	96.77%	99.86%	97.18%	100.00%	97.18%
2016	96.64%	99.86%	100.00%	100.00%	100.00%	99.72%	99.87%	99.60%	99.58%	98.79%	100.00%	99.33%
2017	100.00%	0.00%	0.00%	0.00%	0.00%	0.00%	0.00%	0.00%	0.00%	0.00%	0.00%	0.00%

Table 1: Monthly percentage of availability hourly significant wave height measurements of buoy 62103

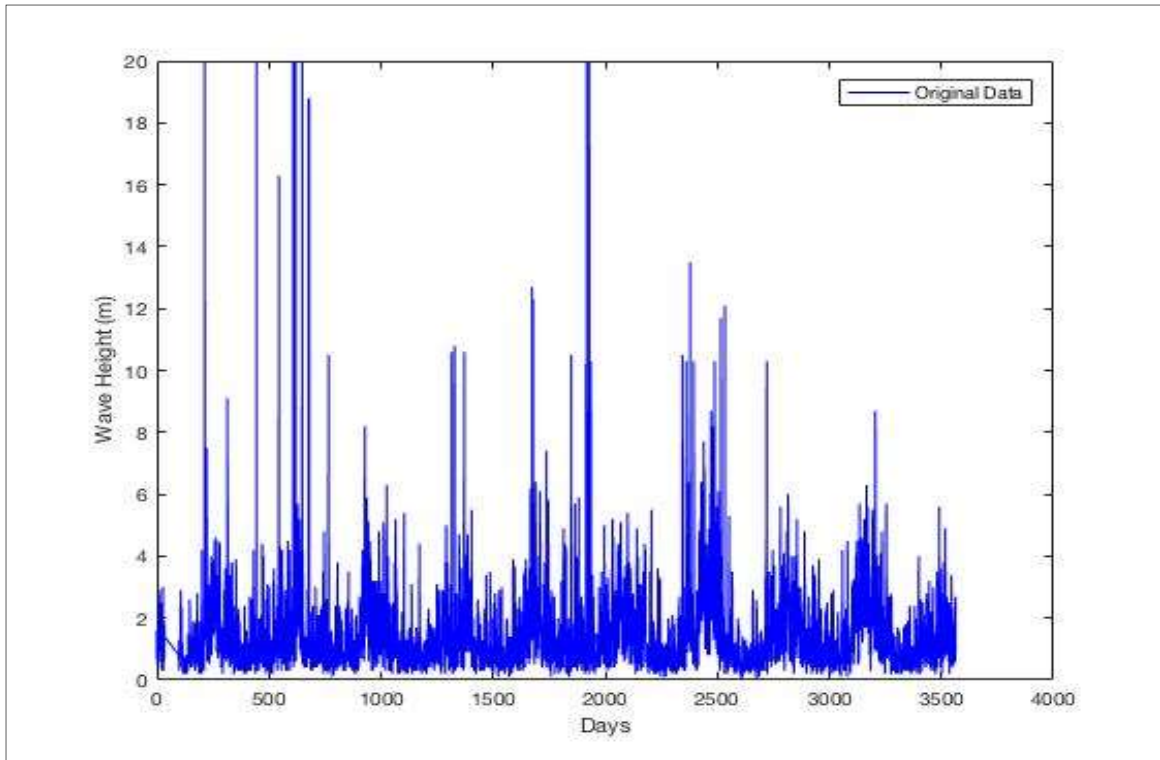


Figure 10: Time series of the available H_s and T_m measurements of buoy 62103

In order to perform a correct analysis of the data, it has been necessary to carry out some quality checks. The following quality checks were carried out:

- The years where measurements are few or insufficient for a meaningful analysis were discarded;
- In order to maintain the same sampling of data, the years with only 3-hourly observations, instead of hourly observations, were discarded;
- Repeated data were discarded;
- The time series was controlled for outliers: observations that deviate more than 7 times the standard deviation of the monthly data from its mean, or more than 3 times the standard deviation of the monthly data from the previous observation.

The quality check process has been automated according to three steps. A representation of the final results obtained is shown in Figure 11.

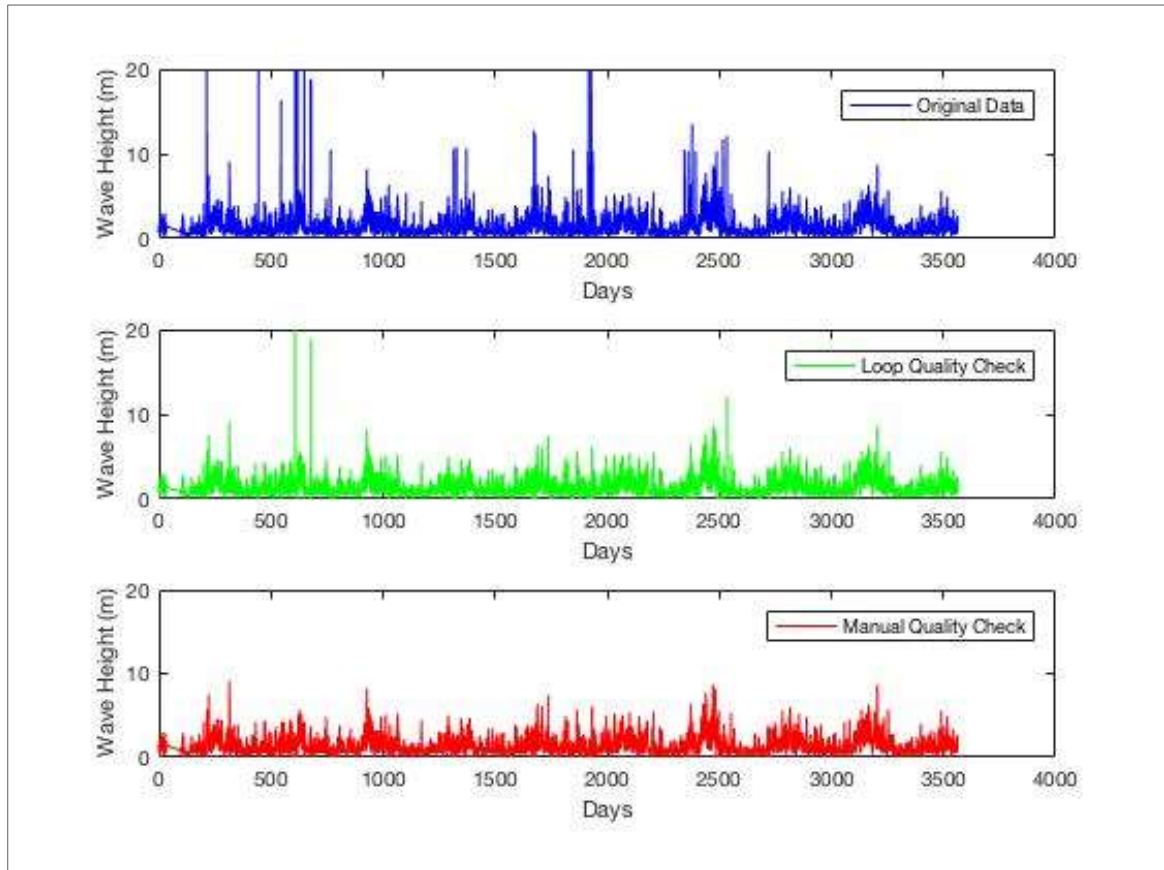


Figure 11: Quality check process

The data are analysed by a POT/GPD approach. In order to produce a suitable GPD for the data provided, the threshold stability property has been used to find the most appropriate parameters (scale parameter σ and shape parameter ξ). Looping through different threshold values on Matlab, the graph of Figure 12 has been produced. Note that, increasing the threshold there is a consequent reduction of the peaks over the threshold. The third graph shown in Figure 12 gives the variation of the 1/50-yr return period as a function of the threshold.

The more suitable threshold has been chosen according to Far & Ahmad Kahiri: *'In general, the method of work is to fit GPD for a range of thresholds, and searching for the stability of parameter estimates'* (Far & Ahmad Kahiri, 2016, p. 5).

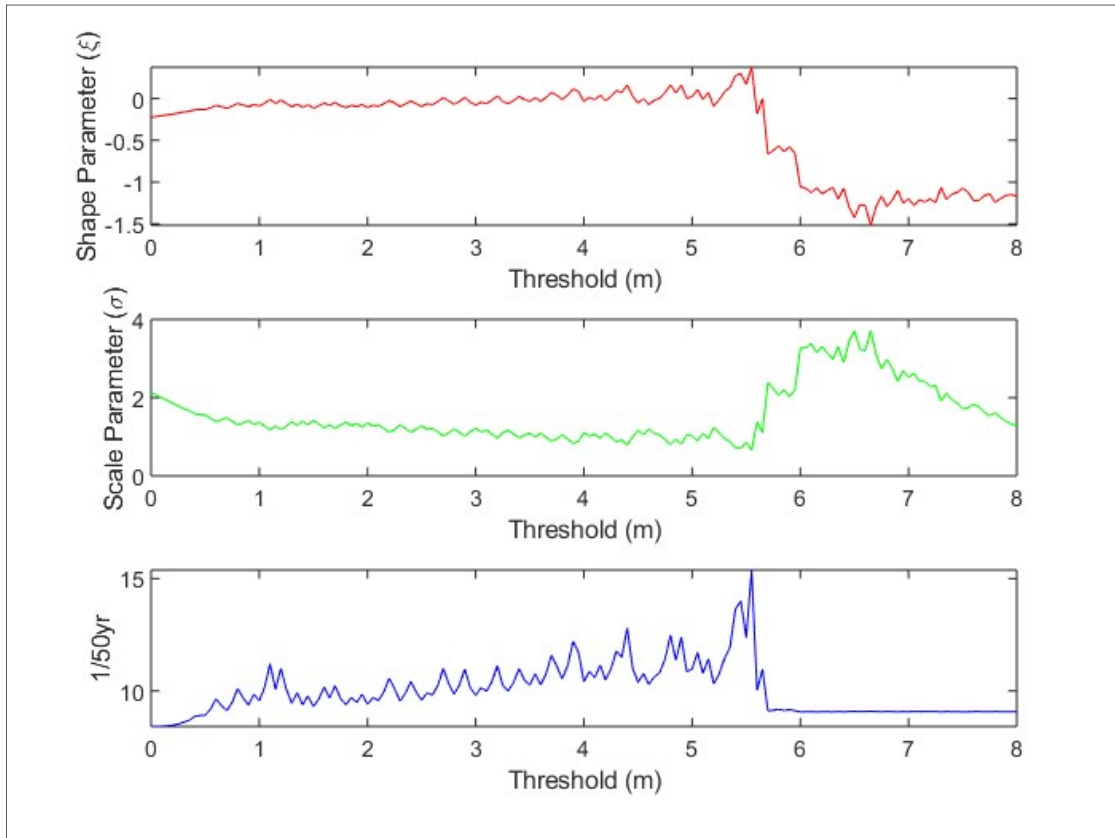


Figure 12: Variation of the estimates of σ , ξ and 1/50yr H_s return values

Finally, from Figure 13 it is possible to see how the GPD fitted to the data.

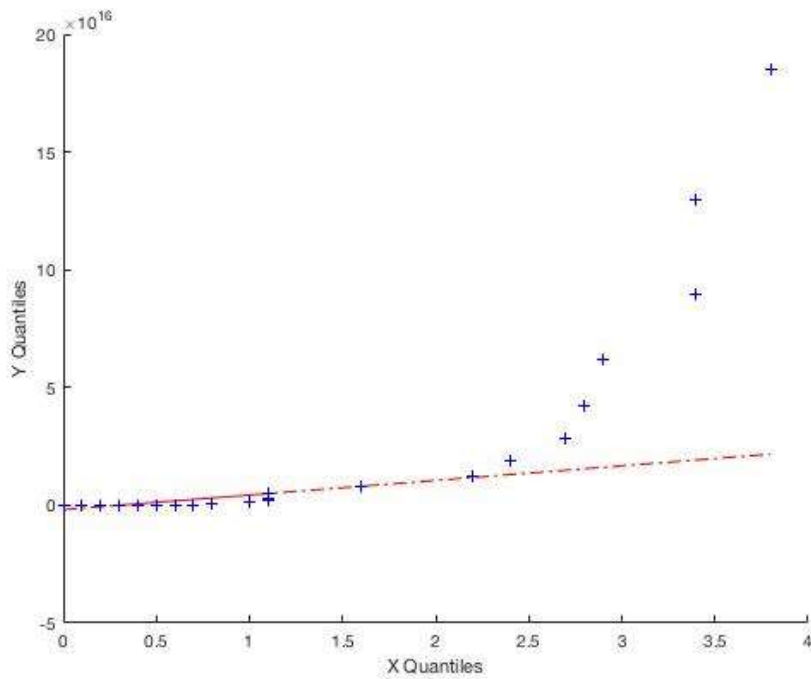


Figure 13: Empirical plot of the quantiles of the data versus the quantiles of the distribution

All necessary information of this first analysis is shown in Table 2.

Parameter	Value
Sample Size	38
Scale Parameter (σ)	0.9486
Shape Parameter (ξ)	0.0797
Threshold (u)	5.3
Return Period (T_r)	50 years
Wave Height (H_s)	11.45 meters
Period (T_s)	17.93 seconds

Table 2: Parameters estimated

CHAPTER III: THEORETICAL BASIS

3.0 Hydraulic Modelling

It is almost impossible in hydraulic research to draw a clear dividing line between basic and applied research; an extraordinary development in experimental methods and application of computational techniques have also been of great importance (Novak & al., 2010).

Many problems can be investigated using mathematical models, which consist of an equation or series of equations that represent the behavior of the system. There are situations with complex flow conditions, lack of detailed data, or difficulty determining the form of the equations; under these circumstances a three-dimensional physical model investigation may be undertaken (Hamill, 2001). The term model is used in hydraulics to describe a physical or mathematical simulation of a prototype (Novak & al., 2010). The relationship between model and prototype performance is determined by the laws of hydraulic similarity. However, hydraulic models should not be viewed as infallible calculators that automatically produce the correct answer to a problem (Hamill, 2001).

3.0.1 Dimensional Homogeneity

Dimensional analysis provides some basic information about the investigated phenomenon on the assumption that it can be expressed by a dimensionally correct equation containing the variables influencing it (Novak & al., 2010).

A general physical quantity could be expressed as product between its magnitude and a unit; for example, the kinetic energy of a body with mass m and speed u :

$$E_k = \frac{1}{2}mu^2 \quad [3.1]$$

can be written in the following way:

$$E_k = E_k^* \cdot E_{ku} \quad [3.2]$$

hence, E_k^* is the magnitude while E_{ku} is the unit.

For the International System of Measurements, all physical quantities can be expressed in terms of three “fundamental dimensions”: length, time and mass. A dimension which is expressed as association of fundamental dimensions, as E_{ku} , is called “derived dimension”.

A general system of measurement is called coherent if: a) all physical quantities of a specific type are measured with the same unit; b) equations between measurements are equal to equations between units. Therefore, for the second condition it is possible to define E_k^* with this equation:

$$E_k^* = \frac{1}{2} m^* u^{*2} \quad [3.3]$$

hence:

$$E_k^* E_{ku} = \frac{1}{2} m^* m_u (u^* u_u)^2 = \frac{1}{2} m^* m_u u^{*2} u_u^2 \quad \rightarrow \quad E_{ku} = m_u u_u^2 \quad [3.4]$$

so, the equation written before, in terms of magnitudes, is now obtained in terms of units.

3.0.2 Similarity with Froude Constant

A scaled model reproduces the natural behaviour of a phenomenon if one of the following similarities is verified:

Geometric similarity: the λ_L ratio, between correspondent linear dimensions, is constant;

Kinematic similarity: at similar points at similar times, the model must reproduce to scale the velocity and direction of flow experienced within the prototype;

Dynamic similarity: at similar points, the model must reproduce to scale all of the forces experienced within the prototype. Therefore, the λ_F ratio, between forces acting in the same point, is constant.

In order to keep the constancy of a ratio between quantities with the same unit, the dimensionless quantities are equal in the prototype as well as in the model.

In fact, in terms of speed it is possible to write:

$$\frac{u_m}{u_p} = \frac{u_m^*}{u_p^*} \cdot \frac{U_m}{U_p} \quad [3.5]$$

hence $u_m/u_p = U_m/U_p = \lambda_u$ and $u_m^*/u_p^* = 1$. This explain the importance of a dimensional analysis of the main hydraulic equations, with the aim of obtaining the same equations composed just with dimensionless parameters. In the following example we can see the dimensionless Navier-Stokes equation:

$$\frac{D\vec{u}^*}{Dt} = -\frac{1}{Fr^2} \nabla^* z^* - \frac{1}{\rho^*} \nabla^* z^* - \frac{1}{Re} \nabla^{*2} \vec{u}^* + \frac{1}{Re} \frac{1}{3} \nabla^* (\nabla^* \cdot \vec{u}^*) \quad [3.6]$$

Underlining that the Froude number and the Reynolds number are both dimensionless, if we could impose the equivalence of Froude number and Reynolds number between model and prototype, we would have their perfect analytical correspondence. Although that, this result is impossible to obtain because the equivalence among Froude numbers produces a distortion of Reynolds numbers and vice versa.

Perhaps the most common type of hydraulic model is the *Froudian model*. The Froude numbers in model and prototype must be the same. Thus $Fr_m = Fr_p$ or:

$$\left[\frac{u}{\sqrt{gL}} \right]_m = \left[\frac{u}{\sqrt{gL}} \right]_p \quad [3.7]$$

From equation [3.7] it is possible to obtain all scale sizes.

Parameter	Scale Size
Length in Direction X	λ_x
Length in Direction Y	$\lambda_y = \lambda_x/n$
Length in Direction Z	$\lambda_z = \lambda_y = \lambda_x/n$
Velocity	$\lambda_u = (\lambda_x)^{1/2}$
Time	$\lambda_t = (\lambda_y)^{1/2} \cdot (n)^{-1}$
Chezy's Coefficient	$\lambda_\chi = (n)^{1/2}$
Forces	$\lambda_f = n$
Volumetric Flow Rate	$\lambda_Q = n^{3/2} \cdot \lambda_x^{5/2}$
Non-distorted Model	$n \neq 1$
Distorted Model	$n = 1$

Table 3: Scale size factors

When a model needs to be constructed that covers a large area of shallow water, it is often necessary to distort the model so that the vertical scale is larger than the horizontal scale (Hamill, 2001). The parameter n shown in Table 3, called *distortion factor*, allows to generalize the scale size of a Froudian model, hence it allows its application also to distorted models.

Because we are assuming the constancy of Froude numbers, it is interesting to analyse how the Reynolds numbers change subsequently.

$$\text{Re}_m = \frac{U_m L_m}{\nu_m} = \frac{U_p \sqrt{L_m/L_p L_m}}{\nu_m} = \frac{\nu_p}{\nu_m} \left(\frac{L_m}{L_p} \right)^{3/2} \frac{U_p L_p}{\nu_p} = \frac{\nu_p}{\nu_m} \cdot \lambda_L^{\frac{3}{2}} \cdot \text{Re}_p \quad [3.8]$$

Before it was stated that “the equivalence among Froude numbers produces a distortion of Reynolds numbers and vice versa”. Therefore, analysing the equation [3.8] it should state that if it is imposed the equivalence between Froude numbers and Reynolds numbers, the ν_p/ν_m ratio is not equal to 1.

$$\frac{\text{Re}_m}{\text{Re}_p} = \frac{\nu_p}{\nu_m} \cdot \lambda_L^{\frac{3}{2}} = 1 \quad \rightarrow \quad \frac{\nu_p}{\nu_m} = \lambda_L^{-\frac{3}{2}} \quad [3.9]$$

Equation [3.9] means that the fluid which flows on the model needs a specific viscosity $\nu_m = \nu_p \lambda_L^{3/2}$ which is, obviously, impossible to obtain. For this reason, it is reasonable to assume that the Reynolds number of the Froudian model is always smaller than the Reynolds number which describes the real phenomenon.

For open boundary models with scales of between 1:10 and 1:100 the viscosity of the model liquid would have to be considerably less than that in the prototype (Hamill, 2001).

3.1 Progressive Small-Amplitude Waves

3.1.1 Characteristics of Progressive Waves

By convention, right-running waves are normally considered in wave mechanics problems. Considering Figure 14, the free-surface displacement caused by the wave is

$$\eta = \frac{H}{2} \cos[k(x - ct)] \quad [3.10]$$

Because the free-surface profile is sinusoidal in both time and space, the maximum displacement, or the crest, occurs when

$$k(x - ct) = 0, \mp 2\pi, \mp 4\pi, \dots \quad [3.11]$$

Consider first the case for which $t = 0$. The distance in the x -direction between two successive crests is the wavelength (λ or L). From equation [3.11] we obtain

$$k = \frac{2\pi}{\lambda} \quad [3.12]$$

The wave parameter, k , is called the wave number.

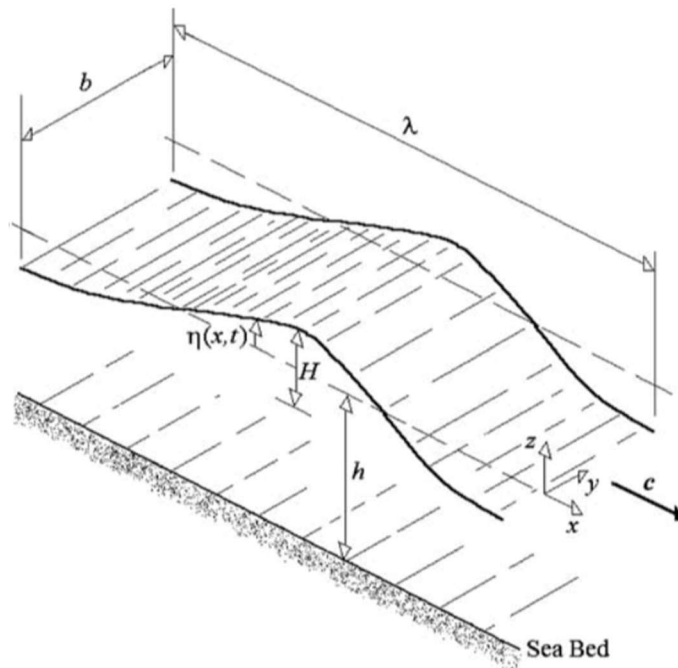


Figure 14: Progressive wave (McCormick, 2010)

Next, consider the expression [3.11] when $x = 0$. The time laps between successive crests is the wave period, T . We obtain:

$$kc = \frac{2\pi}{T} = 2\pi f \equiv \omega \quad [3.13]$$

In equation [3.13], f is the wave frequency in units of Hertz (Hz), and ω is the circular wave frequency in units of radians per second. Combining equations [3.12] and [3.13] by eliminating the wave yields the expression for the celerity or phase velocity:

$$c = \frac{\lambda}{T} \quad [3.14]$$

Finally, it is possible to identify the velocity potential of a progressive wave as

$$\phi = \frac{H}{2} \frac{g}{\omega} \frac{\cosh[k(z+h)]}{\cosh(kh)} \sin(kx - \omega t) \quad [3.15]$$

3.1.2 Kinematics of Wave Motion

Note the velocity potential, it is immediate to determine the two components of the velocity

$$u = -\frac{\partial \phi}{\partial x} \quad [3.16]$$

$$w = -\frac{\partial\phi}{\partial z} \quad [3.17]$$

whence

$$u = \frac{H g k}{2 \omega} \frac{\cosh[k(z+h)]}{\cosh(kh)} \sin(kx - \omega t) \quad [3.18]$$

$$w = -\frac{H g k}{2 \omega} \frac{\sinh[k(z+h)]}{\sinh(kh)} \cos(kx - \omega t) \quad [3.19]$$

thus, it is easy to obtain the local acceleration

$$\frac{\partial u}{\partial t} = \frac{H}{2} \omega^2 \frac{\cosh[k(z+h)]}{\sinh(kh)} \sin(kx - \omega t) \quad [3.20]$$

$$\frac{\partial w}{\partial t} = -\frac{H}{2} \omega^2 \frac{\sinh[k(z+h)]}{\sinh(kh)} \cos(kx - \omega t) \quad [3.21]$$

Examining the velocity components as a function of position, it is clear that they are 90° out of phase; the extreme values of the horizontal velocity appear at the phase positions under the crest, while the extreme vertical velocities appear where the water surface displacement is zero. In Figure 15, the velocity components are plotted for four phase positions. The accelerations are such that the maximum vertical accelerations occur as the horizontal velocities are extremes and the same is true for the vertical velocities and the horizontal accelerations.

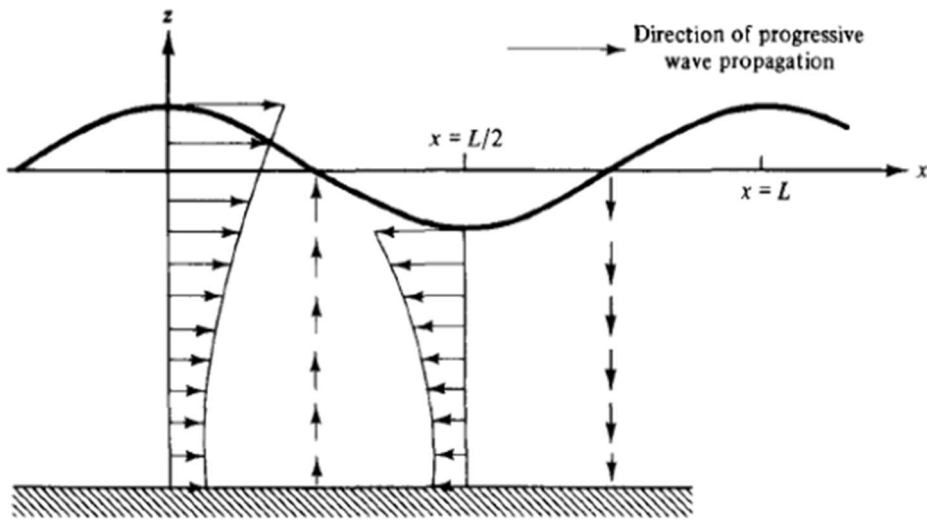


Figure 15: Water particle velocities and accelerations (Dean & Darlymple, 2008)

As we can see in Figure 16, hyperbolic functions produce an exponential decreasing of u and w with the decreasing of z . Hence, when $z \leq -L/2$ the two components of the velocity

could be ignored. Practically, if the depth h is smaller than $L/2$, the component u of the velocity is ignored at the sea bed (ideal fluid), while, for the boundary condition in a horizontal sea bed, the component w is equal to zero.

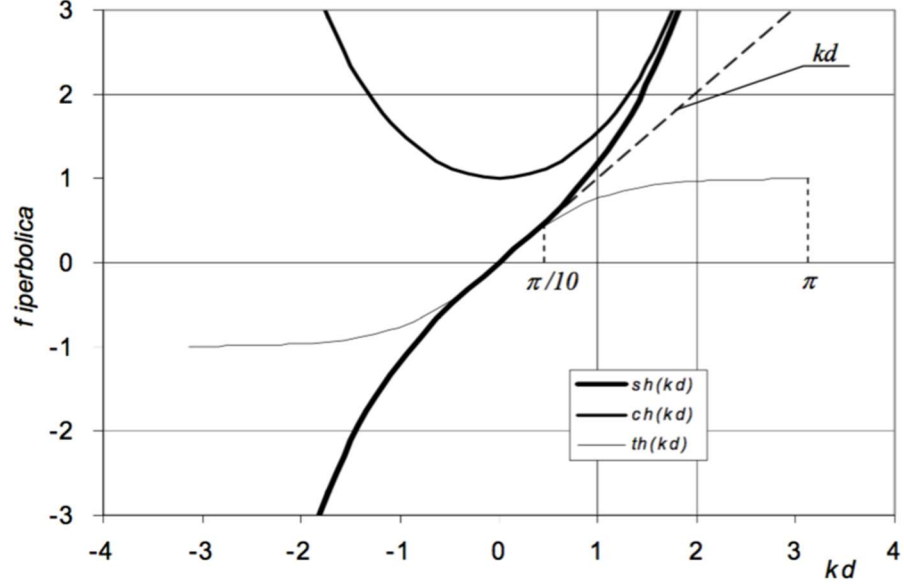


Figure 16: Variation of hyperbolic functions (Atzeni, 2011)

A water particle with a mean position of (x_1, z_1) will be displaced by the wave-induced pressures and the instantaneous water particle position will be denoted as $(x_1 + \zeta, z_1 + \xi)$. The displacement components (ζ, ξ) of the water particle can be found by integrating the velocity with respect to time.

$$\zeta(x_1, z_1, t) = \int u(x_1 + \zeta, z_1 + \xi) dt \quad [3.22]$$

$$\xi(x_1, z_1, t) = \int w(x_1 + \zeta, z_1 + \xi) dt \quad [3.23]$$

In keeping with our small-amplitude wave considerations, ζ and ξ will be small quantities and therefore we can replace $u(x_1 + \zeta, z_1 + \xi)$ with $u(x_1, z_1)$.

Integrating the equation above then yields

$$\zeta = -\frac{H g k}{2 \omega^2} \frac{\cosh[k(h + z_1)]}{\cosh(kh)} \sin(kx_1 - \omega t) \quad [3.24]$$

Thus, the displacements ζ and ξ can be rewritten as

$$\zeta = -A \sin(kx_1 - \omega t) \quad [3.25]$$

$$\xi = B \sin(kx_1 - \omega t) \quad [3.26]$$

which is the equation of an ellipse with semi-axes A and B , as shown in Figure 17.

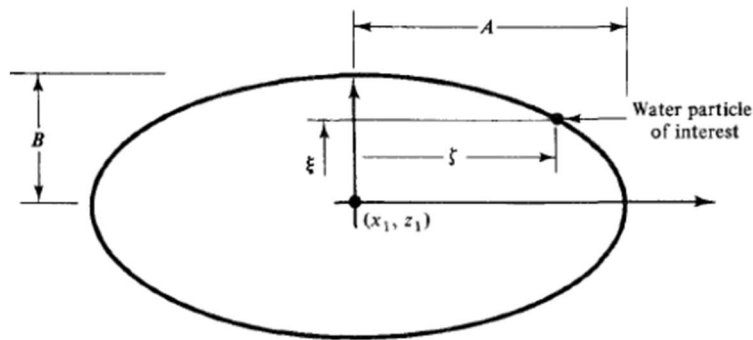


Figure 17: Elliptical form of water trajectory (Dean & Darlymple, 2008)

In *deep water* ($h/\lambda > 1/20$), it can be shown that the semi-axes simplify to $A = B$. Thus, the trajectory are circles which decay exponentially with depth. Figure 18 displays the shapes of the water particle trajectories for different relative depths.

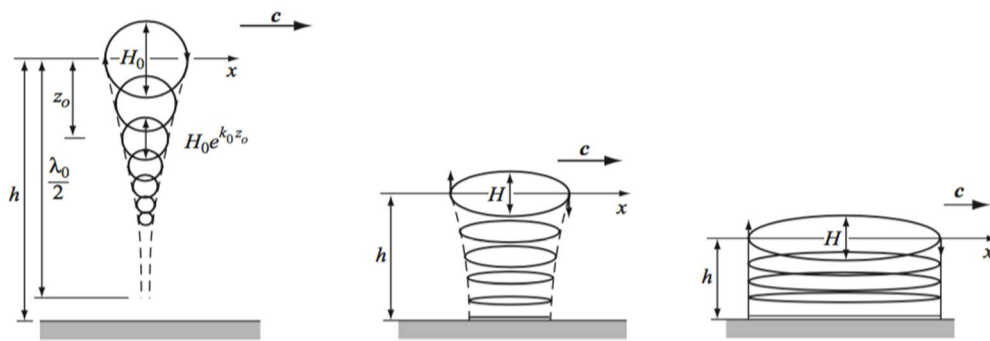


Figure 18: Particle trajectory with different depths (Dean & Darlymple, 2008)

3.2 Wave Forces

The mathematical foundations on which contemporary analyses of wave-structure interactions are based date back to the nineteenth century when Stokes (1851) demonstrated that the total force on a body in an unsteady flow consisted of two components, those being a *drag force* and an *inertial reaction* of the fluid (McCormick, 2010).

In order to obtain a first approximation for the wave force, it could be applied the potential flow approach. We integrate the pressure distribution around the piling using potential flow. For a circular piling, it is convenient to use polar coordinates (r, θ, z) in the horizontal plane (Dean & Darlymple, 2008). In this system, the Laplace equation in three dimensions is:

$$\nabla^2 \phi = \frac{\delta^2 \phi}{\delta r^2} + \frac{1}{r} \frac{\delta \phi}{\delta r} + \frac{\delta^2 \phi}{r^2 \delta \theta^2} + \frac{\delta^2 \phi}{\delta z^2} = 0 \quad [3.27]$$

and the velocity components are:

$$u_r = -\frac{\delta \phi}{\delta r} \quad u_\theta = -\frac{1}{r} \frac{\delta \phi}{\delta \theta} \quad u_z = -\frac{\delta \phi}{\delta z} \quad [3.28]$$

A solution to this equation is:

$$\phi(r, \theta) = U(t)r \left(1 + \frac{a^2}{r^2} \right) \cos \theta \quad [3.29]$$

The quantity $U(t)$ is the far-field velocity and it is considered to vary sinusoidally with the wave period T . At $r = a$, the radius of the pile, there is no-flow condition in the r direction as expected.

$$u_r(a, \theta) = \left[-\frac{\delta \phi}{\delta r} \right]_{r=a} = 0 \quad [3.30]$$

The flow around the cylinder is shown in Figure 19.

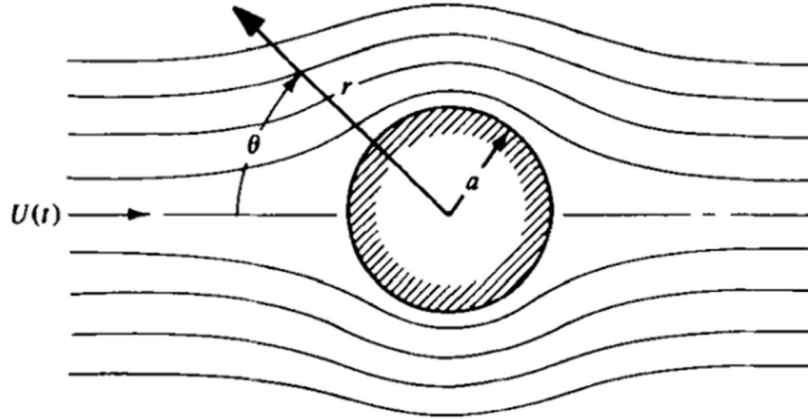


Figure 19: Potential flow around the cylinder (Dean & Darlymple, 2008)

To calculate the pressure distribution around the cylinder, the unsteady form of the Bernoulli equation is applied at the cylinder wall and far upstream at a point where $r = l$, $\theta = 0$ and $l \gg a$. With some mathematical substitutions and rearranging the equation, we obtain the equation [3.31].

$$p(a, \theta) - p(l, 0) = \rho \left[\frac{U^2(t)}{2} \cdot (1 - 4 \sin^2 \theta) + 2a \frac{dU}{dt} \cos \theta - l \frac{dU}{dt} \right] \quad [3.31]$$

In the right-hand side of the equation it is possible to identify two different contributions, the steady (*drag*) flow term, proportional to $U^2(t)$, and the inertial term due to $dU(t)/dt$.

3.2.1 Steady Flow Term

The steady pressure contribution as a function of angular position around the pile is:

$$p(a, \theta) - p(l, 0) = \frac{\rho U^2(t)}{2} \cdot (1 - 4 \sin^2 \theta) \quad [3.32]$$

From Figure 20, we can assume that the horizontal component of the pressure around the cylinder is $p_h = (pa d\theta) \cos \theta$, the analytical expression of the steady flow per unit of elevation (dF_D) is:

$$dF_D = \int_0^{2\pi} p_h d\theta = \int_0^{2\pi} \left[\frac{\rho U^2}{2} \cdot (1 - 4 \sin^2 \theta) + p(l, 0) \right] pa d\theta \quad [3.33]$$

As expected from the pressure symmetry, there is no force on the pile in ideal steady flow. Subsequently, we could assume that:

$$F_D = 0 \quad [3.34]$$

The result of the equation [3.34] is not correct and contrary to the actual results determined from real flows. This discrepancy is called D'Alembert's paradox.

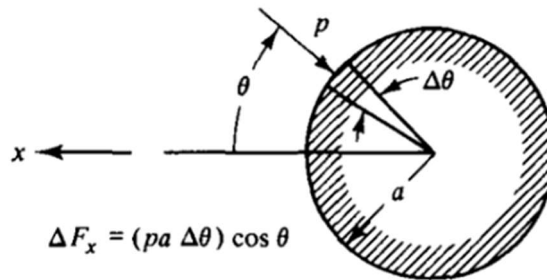


Figure 20: Calculation of the steady flow's horizontal component (Dean & Darlymple, 2008)

The real pressure distribution around a cylinder in steady flow is a function of the Reynolds number (Re). In Figure 21, Goldstein (1938) shows the measured pressure distribution around cylinders for two Reynolds numbers compared to the theoretical ideal low result. Thus, the force per unit length can be related to a function, C_D , which varies with the Reynolds number, allowing us to write the force on the pile per unit of elevation as

$$dF_D = C_D \rho D \frac{U^2(t)}{2} \quad [3.35]$$

The function C_D is called the *drag coefficient* and its variation with Reynolds number is empirically known for steady flows. In practice, C_D is generally on the order of unity and depends on piling roughness in addition to Reynolds number (Dean & Darlymple, 2008).

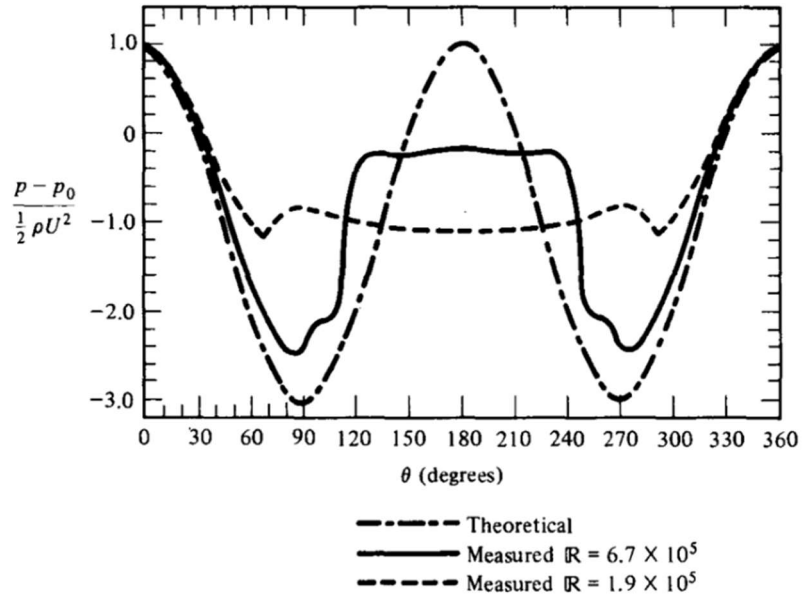


Figure 21: Measured pressure distributions around cylinders (Dean & Darlymple, 2008)

3.2.2 Unsteady Flow Term

Examining the second term of the right-hand side of equation [3.31], we obtain the following result:

$$dF_I = 2\rho V \frac{dU}{dt} \quad [3.36]$$

Generalizing the expression [3.36] for any shape of the object:

$$dF_I = C_M \rho V \frac{dU}{dt} \quad [3.37]$$

where C_M is defined as the *inertia coefficient*, which in this case is equal to 2. The general form [3.37] for the inertia force component is valid for two- and three-dimensional objects of arbitrary shapes, except that the inertia coefficient can vary with the flow direction (Dean & Darlymple, 2008).

The inertia coefficient can be assumed as the sum of two terms:

$$C_M = 1 + k_m \quad [3.38]$$

The pressure gradient required to accelerate the fluid exerts a “buoyancy” force on the object, corresponding to the unity term in equation [3.38]. An additional local pressure gradient occurs to accelerate the neighbouring fluid around the cylinder. The force necessary for the acceleration of the fluid around the cylinder yields the added mass term (k_m) (Dean & Darlymple, 2008). In fluid mechanics, the added mass is the inertia added to

a system because an accelerating or decelerating body must move some volume of surrounding fluid as it moves through it. Added mass is a common issue because the object and surrounding fluid cannot occupy the same physical space simultaneously. For simplicity, this can be modelled as some volume of fluid moving with the object, though in reality "all" the fluid will be accelerated, to various degrees.

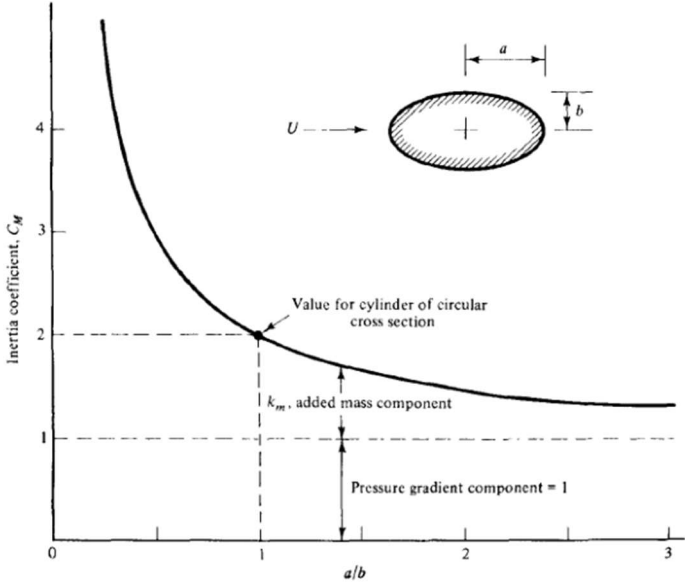


Figure 22: Inertia coefficient (Dean & Darlymple, 2008)

For two-dimensional flow about a cylinder of elliptical cross section, the added mass coefficient k_m can be shown to be: $k_m = a/b$. In Figure 22: Inertia coefficient it is possible to see the variation of the inertia coefficient for a cylinder of ellipsoid cross section.

3.2.3 The Morison Equation

Morison (1950) proposed the following formula for the total wave force, which is just the sum of the two forces, drag and inertia.

$$dF = dF_D + dF_I = \frac{1}{2} C_D \rho A u |u| + C_M \rho V \frac{Du}{Dt} \quad [3.39]$$

The first term on the right side of the equation is the time-dependent drag force, and the second term is the inertial reaction force of the fluid. Equation [3.39] is not just a sum of the previous results because some modifications occur. First, in the equation [3.35] did not account for the change in direction of the horizontal particle velocity so the absolute value of u was added. Second, the original study was directed at a circular cylinder, so the

projected area per unit length (A) was simply D . Finally, the total acceleration in equation [3.37] was originally the local acceleration du/dt .

3.2.4 Oumeraci Theory

The Morison equation [3.39] is the most commonly used for the analysis of the forces acting on slender piles, but its physical foundation has been often questioned because of the neglect of further forces, such as the wave run-up.

We are particularly interested on breaking waves because they may produce very high impact forces. A detailed investigation of breaking waves is extremely difficult, since the duration of these forces is really short. For design purposes, impact forces are taken into account by multiplying the drag force component (F_D) by a factor of 2.5.

For a better examination, the impact force (F_I) must be included as additional part of the Morison equation:

$$F = F_D + F_M + F_I \quad [3.40]$$

H. Oumeraci and J. Wienke (2005) examined the effects of breaking waves on slender cylinder as impact forces. The acting force has been divided into a quasi-static force, which varies in time, and a dynamic component.

When the water hits the cylinder, it is spread around and an impact area can be observed through the development of the splash.

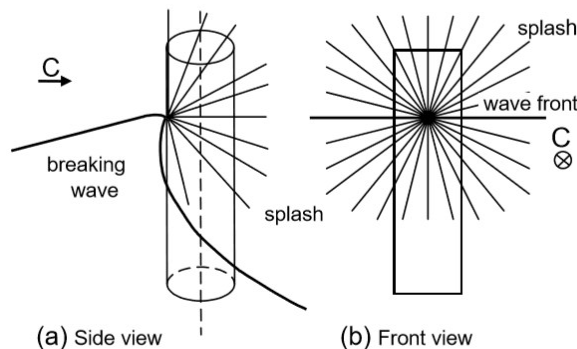


Figure 23: Splash due to breaking waves impact (Wienke & Oumeraci, 2005)

The pressure development is derived from the 2D-model identifying cross sectional planes along the splash direction. “The direction of these planes are defined by the velocity vector \vec{V} of the water mass as it hits the cylinder and a seeming vector selected arbitrarily” (Wienke

& Oumeraci, 2005). The group of planes could be represented by three cartesian axes rotated with an angle Θ .

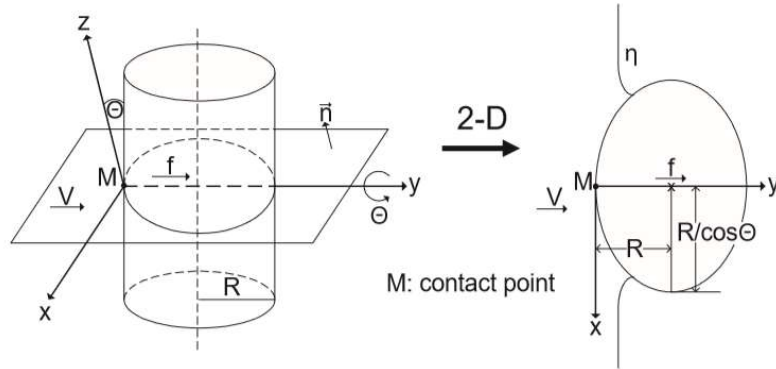


Figure 24: Definition sketch of the group of planes (Wienke & Oumeraci, 2005)

This description is true even for “oblique” impacts with the angle γ between the direction of the impact and the velocity \vec{V} . The impact force given by this theory and normal to the cylinder axis is:

$$F_t = \lambda \eta_b \rho R V^2 \cos^2 \gamma \cdot \left(2\pi - 2 \sqrt{\frac{V \cos \gamma}{R}} t \cdot \tanh^{-1} \sqrt{1 - \frac{1}{4} \frac{V \cos \gamma}{R}} t \right) \text{ with } 0 \leq t \leq \frac{1}{8} \frac{R}{V \cos \gamma} \quad [3.41]$$

$$F_t = \lambda \eta_b \rho R V^2 \cos^2 \gamma \left(\pi \sqrt{\frac{1}{6} \frac{1}{V \cos \gamma} t'} - \sqrt{\frac{8}{3} \frac{V \cos \gamma}{R}} t' \tanh^{-1} \sqrt{1 - \frac{V \cos \gamma}{R}} t' \sqrt{\frac{V \cos \gamma}{R}} t' \right) \text{ with } t' = t - \frac{1}{32} \frac{R}{V \cos \gamma} \quad [3.42]$$

As we can see in the equations [3.41] and [3.42], the impact force depends only on the velocity \vec{V} which is the velocity of the water hitting the contact point and could be called *impact velocity*.

The parameter λ , called *curling factor*, is determined experimentally and needs to be better described. After the impact force, supposed to be very short, the slender cylinder is dominated by high frequency oscillations which are a manifestation of the response of the cylinder due to its structural properties. “The longer the cylinder, the lower the frequency of oscillations is” (Wienke & Oumeraci, 2005). The curling factor included in the equations [3.41] and [3.42] is chosen such as to get the same measured and calculated value. Several values for curling factor were proposed in literature; for example (Goda, 1973):

$$\lambda = 0.1 \quad \text{for spilling breaker}$$

$$\lambda = 0.4 \quad \text{for plunging breaker}$$

Some studies of J. Wienke and H. Oumeraci show the dependency of λ on the yaw angle.

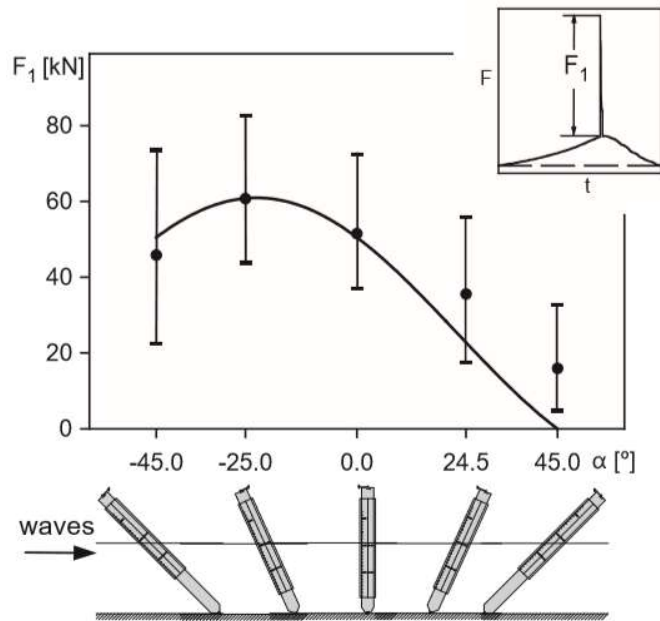


Figure 25: Curling factor λ against yaw angle α (Wienke & Oumeraci, 2005)

Thus, the equation [3.43] has been obtained.

$$\lambda = \frac{\cos(\alpha - \beta)}{\cos \alpha} \quad [3.43]$$

Considering that the slender cylinder is inclined by an angle γ , its shape is approximated with an elliptic plane (Wienke & Oumeraci, 2005) as shown in the following figure.

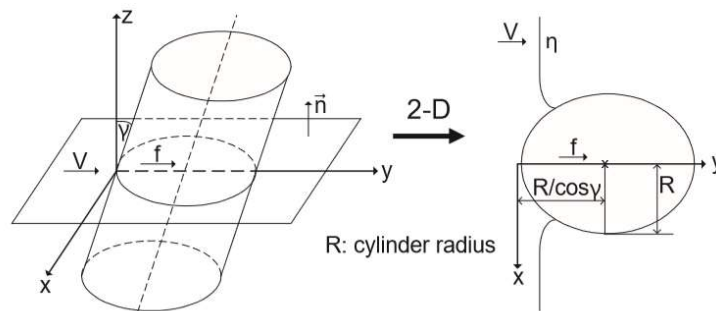


Figure 26: Oblique impact (Wienke & Oumeraci, 2005)

It has been concluded that the total duration of the impact is given by:

$$\tau = \frac{13}{32} \frac{1}{\cos \gamma} \frac{R}{V} \quad [3.42]$$

3.3 New Wave

The ocean displacement around a wave crest could be derived as a random part and a deterministic part. This method is usually applied for extreme ocean waves in design conditions. “It is essentially a linear, broad-banded wave theory in which the frequency components have amplitudes and phases such that the most probable extreme wave is obtained” (Tromans, Anaturk, & Hagemeyer, 1991).

Extreme loads always have an important responsibility during the design process, thus a good prediction and an efficient utilization is necessary. In conventional design practices, wave loads are obtained using deterministic methods and the height and the period of the wave are chosen in reference to a 100-year or a 10'000-year event. The new wave theory is based on a probabilistic analysis to estimate the most probable sea surface displacement around a crest. The ocean surface can be seen as statistically stationary over some finite area during a time interval, typically of three hours. The displacement along the vertical axis is $\eta(x, y, t)$, where x and y are coordinates in the plane at mean sea level and t is time. This variable can be written such as:

$$\eta(x, y, t) = \sum_n c_n \cdot \cos(k_n x \cos(\theta_n) - \omega_n t + \varepsilon_n) \quad [3.43]$$

where n is a large number, k_n is the wave number, θ_n is the direction relative to the mean wave direction (e.g. x), ω_n is the frequency and ε_n is a random phase.

The amplitude value is given by:

$$c_n = f(\theta_n, \omega_n) S(\omega_n) \Delta\omega \Delta\theta \quad [3.44]$$

“Extreme waves occur when many wavelets, particularly the more energetic ones, come into phase” (Tromans, Anaturk, & Hagemeyer, 1991).

The variable η at a specific point x_1, y_1 is $\eta_1(t)$; see Figure 27. A crest is present, at the time t_1 in this case, when $\frac{\partial \eta}{\partial t} = \dot{\eta} = 0$. Knowing the probability density functions (pdfs) of η , η_1 and $\dot{\eta}$, so are the joint and conditional pdfs.

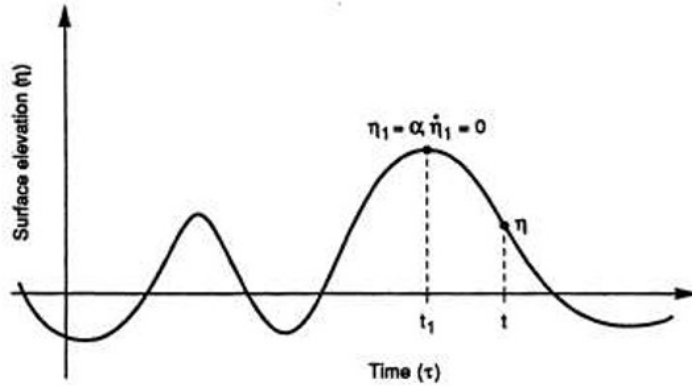


Figure 27: Ocean surface elevation at a given point (Tromans, Anaturk, & Hagemeyer, 1991)

In particular, equation [3.45] gives a better description of η on the presence of a crest of height α at time t_1 .

$$p(\eta|\eta_1 = \alpha, \dot{\eta}_1 = 0) = \frac{p(\eta, \eta_1, \dot{\eta}_1)}{p(\eta|\eta_1) \cdot p(\dot{\eta}_1)} \quad [3.45]$$

Equation [3.45] leads to:

$$p(\eta|\eta_1 = \alpha, \dot{\eta}_1 = 0) = \frac{1}{\sqrt{2\pi}\sigma_2} \cdot e^{-\frac{(\eta-m)^2}{2\sigma_2^2}} \quad [3.46]$$

which is a normal distribution with expected and most probable value:

$$m = \alpha \cdot \rho(\tau) \quad [3.47]$$

and variance:

$$\sigma_2^2 = \sigma^2 \cdot \left(1 - \rho^2 - \frac{\rho^2}{\lambda^2}\right) \quad [3.48]$$

From equation [3.47] it is possible to see that increasing the crest height value (α), the expected value (m) also increases while the standard deviation remains constant. Therefore, the displacement η around the crest can be described by the Slepian model process (Tromans, Anaturk, & Hagemeyer, 1991), such as:

$$\eta^*(\tau) = \alpha\rho(\tau) + g(\tau) \quad [3.49]$$

where $\tau = t - t_1$ and $\rho(\tau)$ is the autocorrelation function of the sea surface elevation. The expression of $\rho(\tau)$ is obtained as the Fourier transform of the surface spectrum (Tromans, Anaturk, & Hagemeyer, 1991). Thus:

$$\rho(\tau) = \frac{1}{\sigma^2} \int_0^\infty S(\omega) \cos \omega \tau \, d\omega \approx \frac{1}{\sigma^2} \sum_n [S(\omega) \cdot \Delta\omega] \cos \omega_n \tau \quad [3.50]$$

Figure 28 shows the sea surface displacement against the time, when $x = 0$, or against the position, when $\tau = 0$.

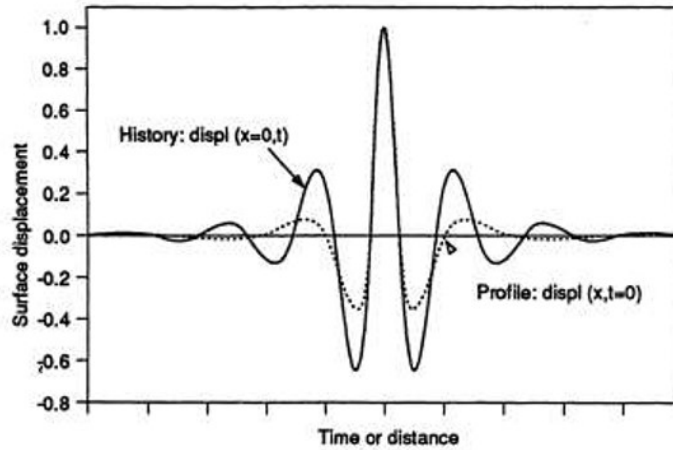


Figure 28: Most probable extreme surface displacement (Tromans, Anaturk, & Hagemeyer, 1991)

Another description is given by Figure 29.

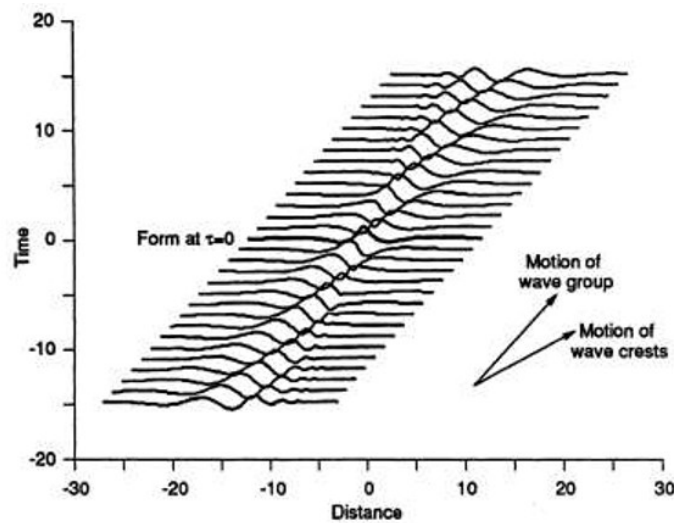


Figure 29: Evolution of the expected ocean surface elevation in space and time (Tromans, Anaturk, & Hagemeyer, 1991)

The crest height increases when the wave comes from negative x , reaches a maximum when $x = 0$, and decays when it goes to the positive x . This process of growth and decay must be taken into account especially when the theory is applied through any fluid loading software.

3.4 Methods of Data-Analysis

Commonly, all methods for data-analysis are based on linear and stationary assumptions but, unfortunately in most likely situations, the data are both non-linear and non-stationary. The Hilbert-Huang transform (HHT) is one of the latest methods, introduced by Huang et al. (1996, 1998, 1999), and suitable for non-linear and non-stationary data especially for time-frequency-energy representations. This method can be separated into two parts: empirical mode decomposition (EMD) and Hilbert spectral analysis (HSA). Although it has been extensively applied and validated only empirically, it gives much better results than traditional methods.

3.4.1 The Empirical Mode Decomposition (EMD)

As it has been said before, the empirical mode decomposition (EMD) is applied for the analysis of non-linear and non-stationary data. Figure 30 gives an example of some test data suitable for this type of process.

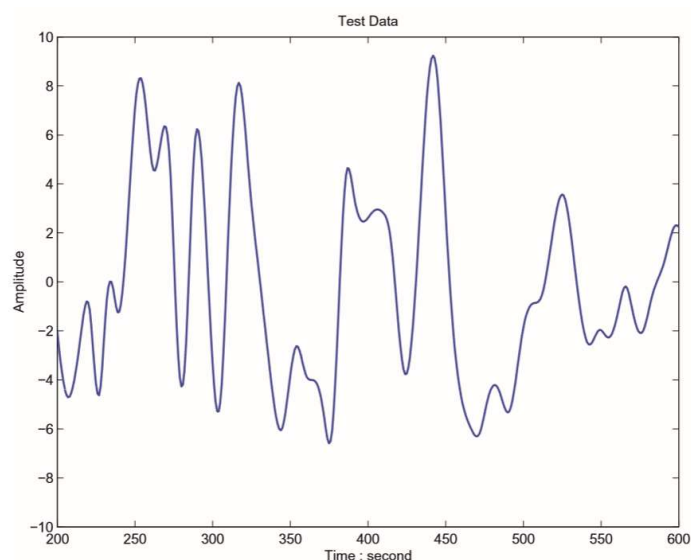


Figure 30: Example of test data (Huang & Shen, 2014)

The EMD is based on the assumption that any data is intrinsically formed by different simple modes of oscillations, linear or non-linear, and each of them characterises a simple oscillation with the same number of extrema and zero-crossings. For a generic time, all the simple oscillations can be superimposed to obtain the beginning data. Huang and Shen (2014) defines every oscillatory mode by an intrinsic mode function (IMF) with the following characteristics:

- 1) In the whole dataset, the number of extrema and the number of zero-crossings must either equal or differ at most by one;
- 2) At any point, the mean value of the envelope defined by the local maxima and the envelope defined by the local minima is zero.

The IMF provides one of the oscillatory modes but, instead of constant amplitude and frequency, it can have a variable amplitude and frequency with time. The analysis of the data is shown in Figure 31.

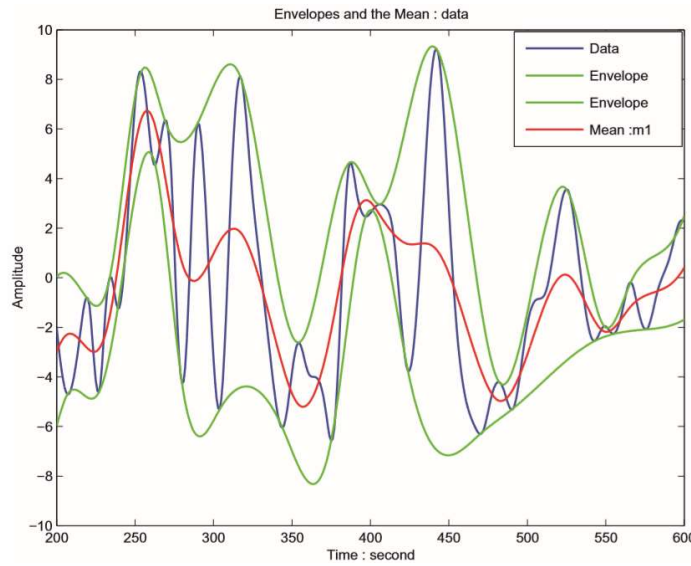


Figure 31: The data with upper and lower envelopes (Huang & Shen, 2014)

After all the local maxima and local minima are identified, they are connected by a spline line (green line in Figure 31) finding the upper and the lower envelopes. Calculating the mean value between the upper envelope and the lower envelope (m_1), which is constant with time, the first component is easily obtained:

$$h_1 = x(t) - m_1 \quad [3.51]$$

“The sifting process serves two purposes: to eliminate riding waves and to make the wave profiles more symmetric” (Huang & Shen, 2014).

The sifting is repeated several times, but from the second step the h_1 is treated as the data; then,

$$h_{11} = h_1 - m_{11} \quad [3.52]$$

After k -times, the h_{1k} is obtained:

$$h_{1k} = h_{1(k-1)} - m_{1k} \quad [3.53]$$

The next step is the definition of a stoppage criterion. Huang and Shen (2014) presents two alternative criteria. The first one (1998) is based on a Cauchy type of convergence and, specifically, the test requires that a given normalised squared difference (equation [3.54]) between two successive operations is small enough.

$$SD_k = \frac{\sum_{t=0}^T |h_{k-1}(t) - h_k(t)|^2}{\sum_{t=0}^T h_{k-1}^2} \quad [3.54]$$

If SD_k is smaller than a certain value, the process will be stopped.

Because of some shortcomings that the previous method has got, a second method is proposed (1999, 2003). A S -number is pre-selected and the process will be stopped only after S consecutive times, provided that the number of zero-crossings and extrema remains almost the same (with a maximum difference of one unit). Obviously, before selecting the S -number, a rigorous explanation is needed. Huang et al. (2003), after many tests using different values of S -number, show that it should be set between 4 and 8.

Assuming that a stoppage criterion has been adopted, the residual value (r_i) is found from each iteration; so that

$$r_1 = x(t) - c_1 \quad [3.55]$$

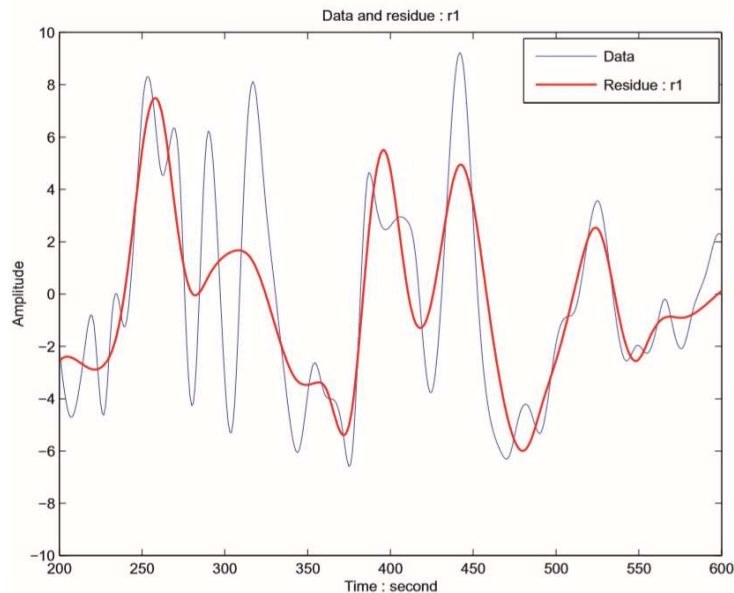


Figure 32: The original data (blue) and the residue (red) (Huang & Shen, 2014)

Since the residue still contains longer period variations in the data, it is treated as the new data and subjected to the same sifting process as before (Huang & Shen, 2014). The process keeps going until the predetermined stoppage criterion is obtained. Thus, the data have been decomposed into n -empirical modes and a final residue r_n .

Obviously, the following equation must be verified:

$$x(t) = \sum_{j=1}^n c_j + r_n \quad [3.56]$$

The final result can be shown as in the following figure, in which it is possible to see the variation in terms of frequency.

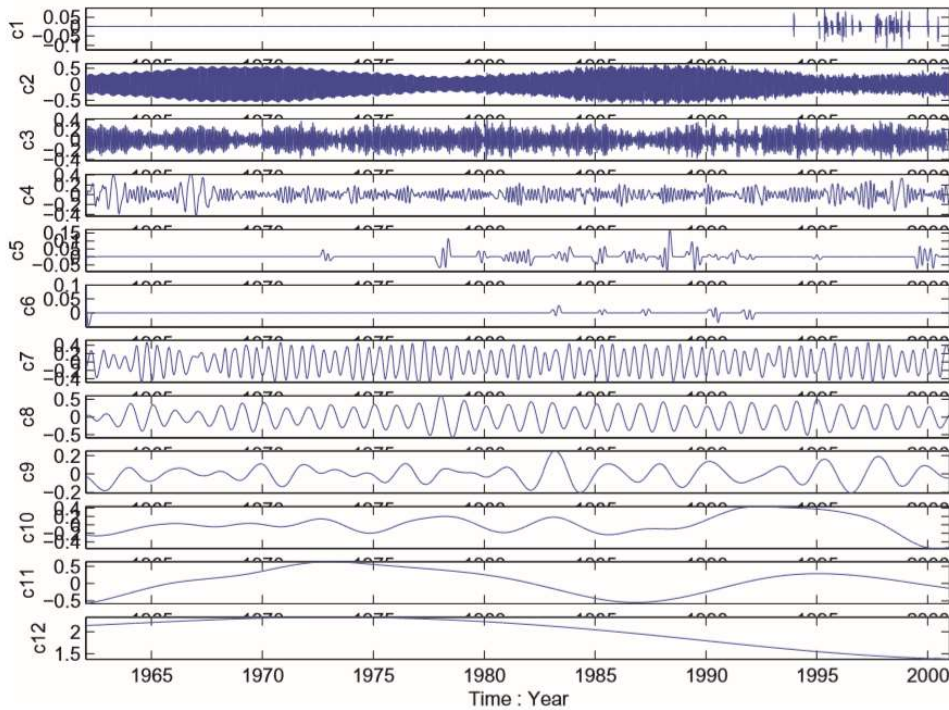


Figure 33: Representation of the n -empirical modes (Huang & Shen, 2014)

3.4.2 The Ensemble Empirical Mode Decomposition (EEMD)

The ensemble empirical mode decomposition (EEMD) takes into account the potential noise in the data set. Since EMD uses the extrema information to separate the riding “natural” wave and its reference, as described in the previous paragraph, changes in extrema locations and values due to noise may lead to significantly different results, which makes the extracted “natural” wave sometimes appear “unexpected” (Huang & Shen, 2014). This is well shown in Figure 34.

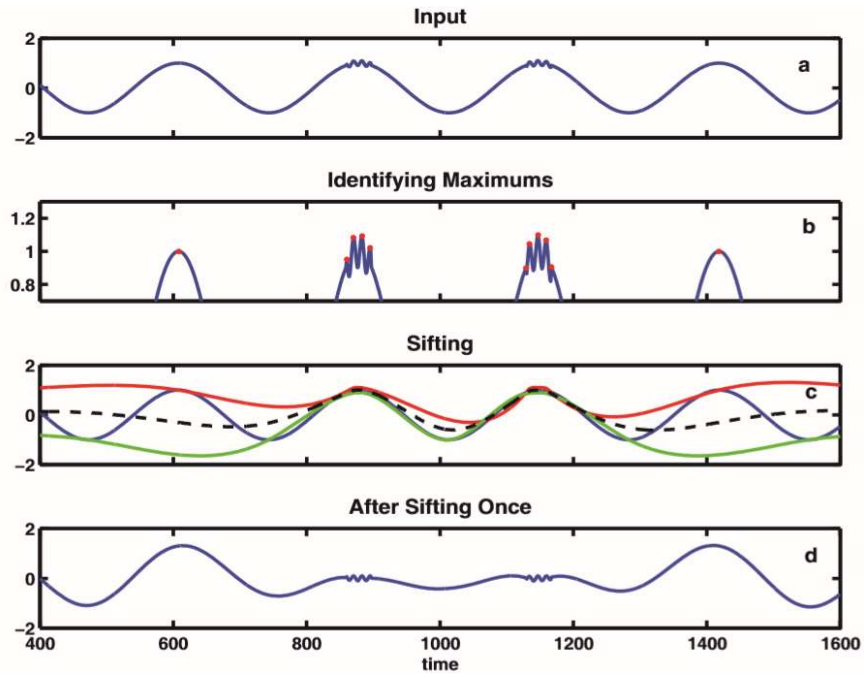


Figure 34: EMD application on data affected by noise (Huang & Shen, 2014)

Therefore, Huang and Shen (2014) present the EEMD method as a series of steps:

1. Add a white noise series to the targeted data;
2. Decompose the data with added white noise into IMFs;
3. Repeat the first and the second steps several times, but with different realisation of white noise series each time;
4. Obtain the *ensemble* means of corresponding IMFs of the decompositions as the final result.

Although the noisy is always increased every step, it is expected that it will be cancelled out in the ensemble mean of several iterations. Under such conditions:

$$c = \lim_{n \rightarrow \infty} \frac{1}{N} \sum_{k=1}^n [c_j(t) + r_k(t)] \quad [3.57]$$

The amplitude of noise is not necessary small but the ensemble number of trials has to be large, in order to cancel out the added noise.

The EMD, with this approach, is has become a more mature tool for non-linear and non-stationary time series analysis.

3.4.3 The Duhamel Integral

With the aim of finding the natural vibration of the model, several known types of impulses have been tested in the laboratory in order to obtain that one which better matches with the measured one. Thus, the cylinder has been assumed a single-degree of freedom (SDOF) system with specific mass, stiffness and damping ratio. The Duhamel integral allows the detection of the response due to the defined impact loading.

The single degree of freedom system is a spring-mass-damper system where the spring has no damping or mass, the mass has no stiffness or damping and, finally, the damper has no mass or stiffness (Gavin, 2016).

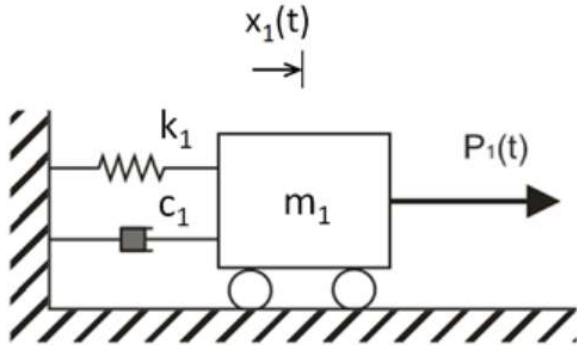


Figure 35: The prototype single degree of freedom (Fabula, 1957)

Figure 35 is a schematic illustration of the model used for the analysis. The cylinder is represented by the block where the total mass (m) is contained. All the other physical characteristics of the model are divided and discretised, such as: the elastic resistance is provided by the stiffness of the spring (k_1) and the damping is represented by the damper (c).

In order to extract the *Impulse Response Function* of the model during the laboratory experiments, it has been hit on several points and the amplitude variation with time is shown in Figure 36. A Matlab code allowed to fit a logarithmic envelope on the impulse time series.

mass	9.88 kg	damped eigen frequency	16.0533 Hz
natural frequency	15.96 Hz	damping	1.5529 Nms
damping ratio	0.0045	stiffness	2.5462e+03 Nm

Table 4: Dynamic parameters of the model

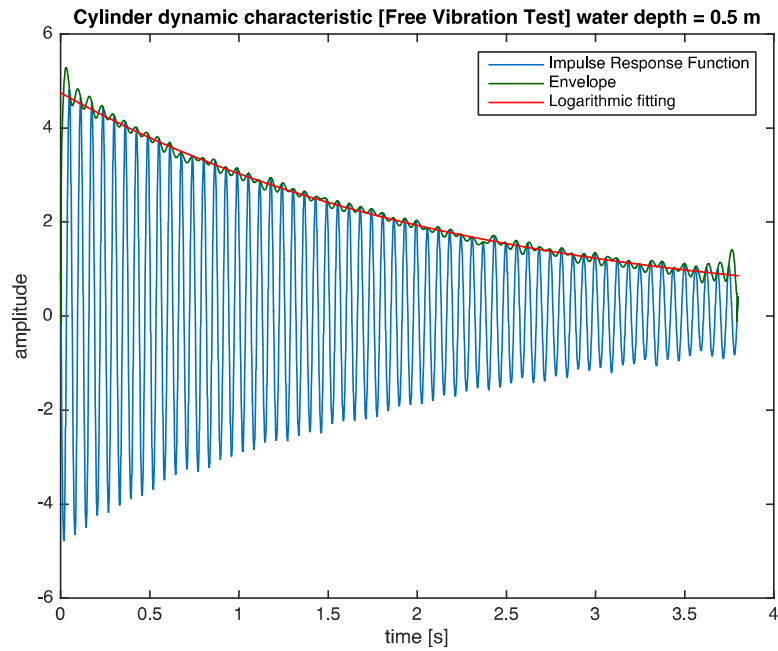


Figure 36: Free vibration of the model

As said before, for the analysis of the free vibration, the structure was hit in different point with impulse loads. An impulse load can be described as a pressure variation with a principal peak (see Figure 37)

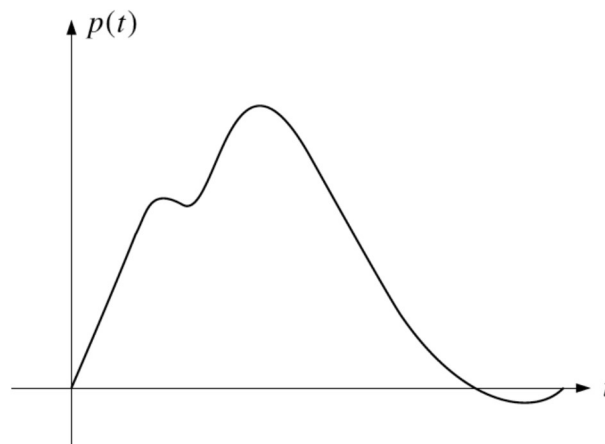


Figure 37: Generic impulse time series (Fabula, 1957)

In this case, damping has much less importance in controlling the maximum response of a structure than for periodic or harmonic loads. This is because the maximum response to a particular impulse load will be reached in a very short time before the damping forces can absorb much energy from the structure (Collados, 2011).

An impulse is commonly described with certain mathematical expressions. The first example is given in Figure 38; it is a half-sine-wave impulse and can be divided into two

parts: the first part, when the force acts, is the forced-vibration phase while the second part is the free-vibration phase.

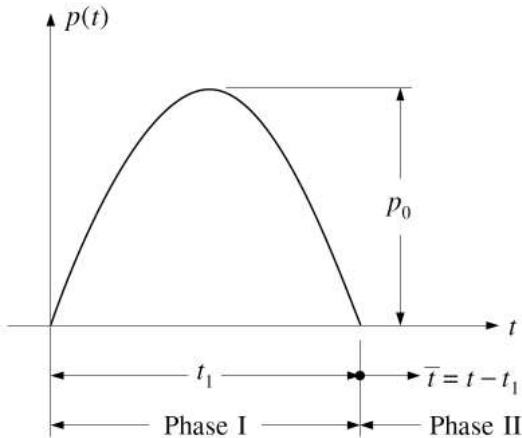


Figure 38: Half-sine wave impulse (Fabula, 1957)

The second example, shown in Figure 39, is the rectangular impulse or step loading. As said for the previous example, two phases are identified: the forced-vibration phase and the free-vibration phase.

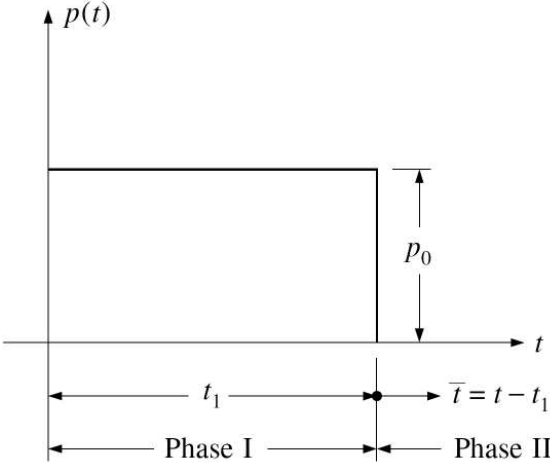


Figure 39: Rectangular impulse (Fabula, 1957)

The impulse shape that better fit the recorded force time history of a wave hitting a cylinder is the triangular one (Figure 40).

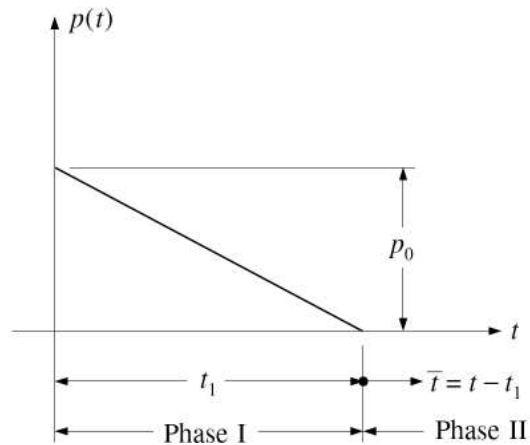


Figure 40: Triangular shape impulse (Fabula, 1957)

Once again, this case owns two phases. The loading phase, in this case, can be further divided into two additional parts, a preliminary increasing phase at the beginning, called rising phase, and a subsequent decreasing phase up to zero. The example shown in Figure 40 is reached when $t_p = 0$.

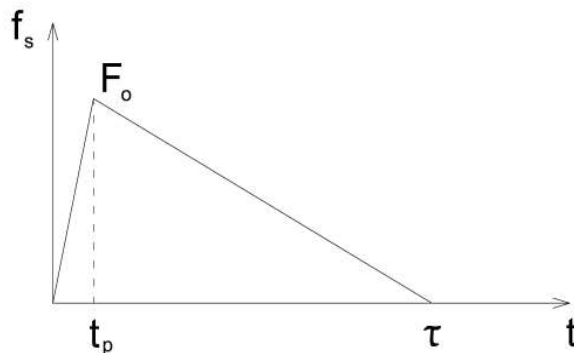


Figure 41: Generic triangular impulse shape (Fabula, 1957)

As mentioned before, the impulse loading has a very short duration thus the rising phase will be extremely short because it represents the smallest part of the total impulse. Figure 41 shows this particular case. The symbols F and F_0 have the same meaning as the symbols $p(t)$ and p_0 used in the previous figures.

Some interesting studies can be found in literature about the comparison of the various impulses described; Figure 42 is the most commonly used picture for describing the differences between the impulses in terms of maximum response ratio against the ratio impulse duration-period.

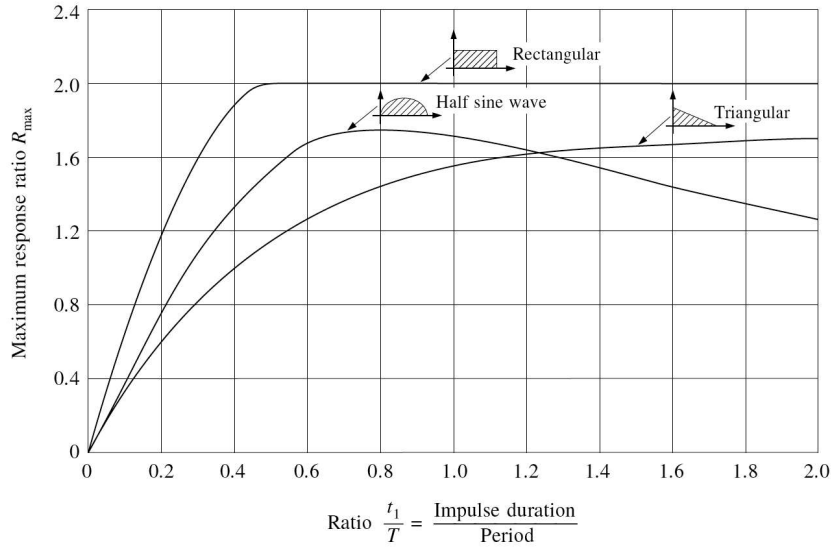


Figure 42: Impulse shapes comparison (Fabula, 1957)

From an applicative point of view, the response of a structure is calculated according to the Duhamel integral once a certain impulse shape has been assumed. Then, the calculated response is compared with the measured one and the process keeps going until a good agreement is reached. The entire loading history can be decomposed in a succession of very short impulses, each one producing its own differential response (Figure 43).

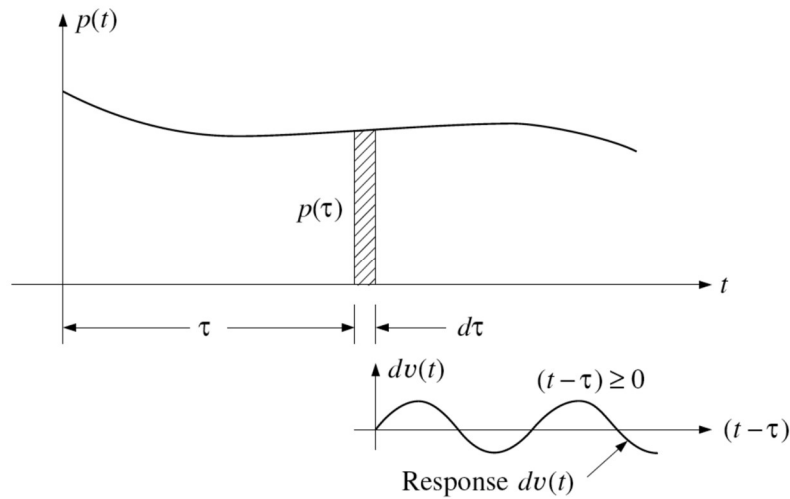


Figure 43: Description of the Duhamel integral (Fabula, 1957)

The total calculated response can be obtained by summing all the differential responses developed during the loading history.

$$R(t) = \frac{k}{m \cdot w_d} \int_0^t p(\tau) \sin w_d (t - \tau) \exp[-\xi w_d (t - \tau)] dt \quad [3.58]$$

where,

m : oscillating mass;

w_d : damped frequency of oscillation;

$p(\tau)$: impulse load applied for a very short time;

ξ : damping coefficient;

t : time.

CHAPTER IV: PHYSICAL MODELLING

4.0 Laboratory Set-up

The tests have been carried out in one of the tanks of the Plymouth University laboratory. The tanks has a flat bottom and a series of paddles at one of the extremities, at the other extremity there is a variation of the bottom slope which allows to absorb the energy of the waves generated.

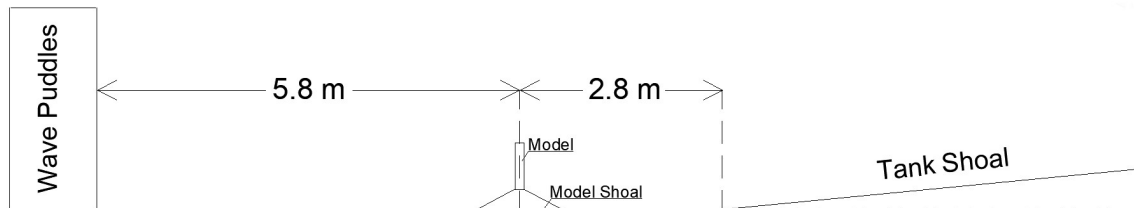


Figure 44: Wave tank cross-section scheme (not scaled)

The model was positioned in the middle of the lateral walls of the tank and 5.8 meters away from the paddles, therefore the waves has the necessary space to focus at the required position. At the same time, the inclination from the tank bottom has been taken into account to avoid excessive noises due to wave reflections. The tank was filled with 0.5 meters of water.

The shoal, placed at the bottom of the cylinder, represented one of the main part of the physical modelling. In fact, the STORMLAMP project began with some initial tests in the wave flume tank of the University of Plymouth that allowed a reduced analysis of the effects that a group of waves can have on the cylinder.

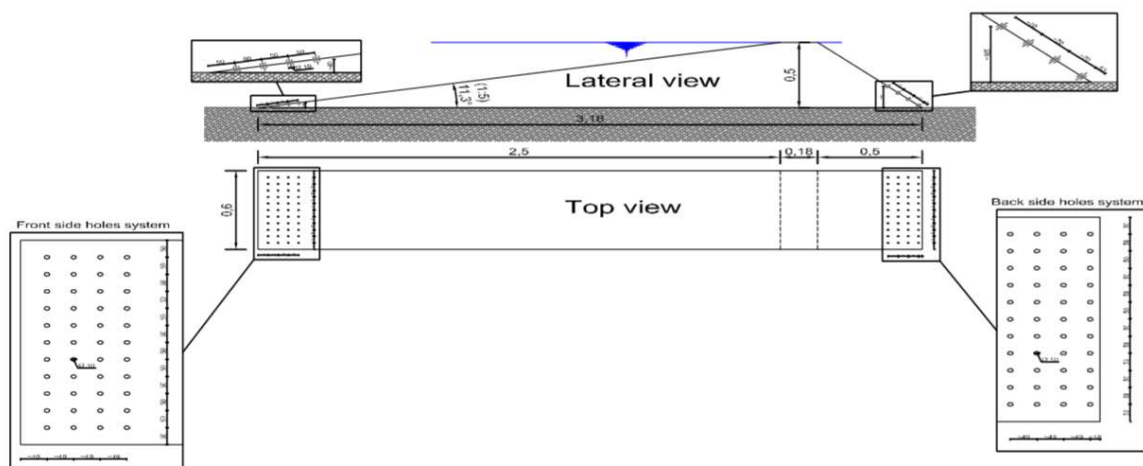


Figure 45: Shoal characteristics of the first tests carried out

Figure 45 shows the shoal realised for the first experiments. Clearly, the dimensions of the tank and its lateral walls do not allow to consider the three-dimensional effects of the shoal that raises the wave both in front of the model and laterally. Figure 46 shows the shoal realised for the new experiments (all quantities are defined in meters).

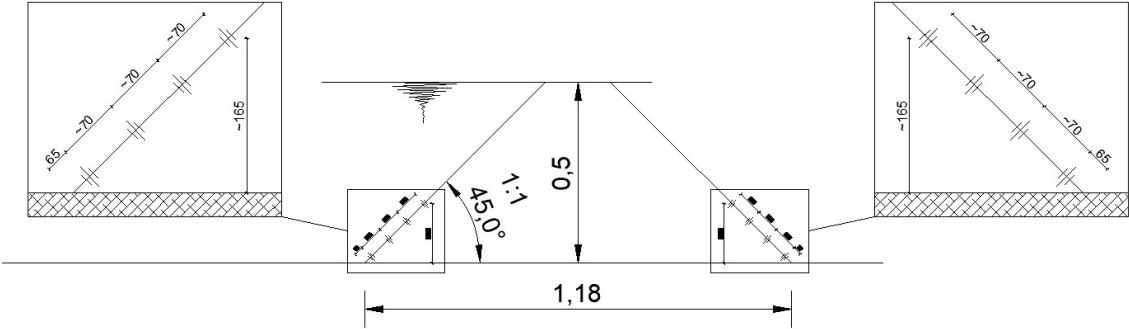


Figure 46: Shoal cross-section scheme (not scaled)

As it is possible to see in Figure 46, the shoal height is 0.5 m so the free level of water perfectly cover it.

The shoal, completely built with treated wood to avoid swelling effects, has been fixed to the bottom of the tank and suitably isolated so that water did not leak in.



Figure 47: Photo of the shoal in the laboratory tank

The model of the lighthouse was subsequently placed almost one millimetre above the shoal; in this way it was possible to consider both the effect of the real rocks where the lighthouse is based on, and to accurately measure the model's response to the acting waves. The model, shown in Figure 48, is a cylinder 25 cm high, made of steel and carefully drilled for positioning the pressure transducers.



Figure 48: Scaled model of the lighthouse

The head model has been fixed to some steel beams accurately hooked to the sides of the tank. Subsequently, the main steel beam has been reinforced and stiffened with additional beams (see Figure 49) hence its vibrations were minimised to avoid significant effects on the model's responses. It is specified that the laboratory tests treated the modelling of the wave group behaviour, so the model's response haven't been modelled but only recorded.

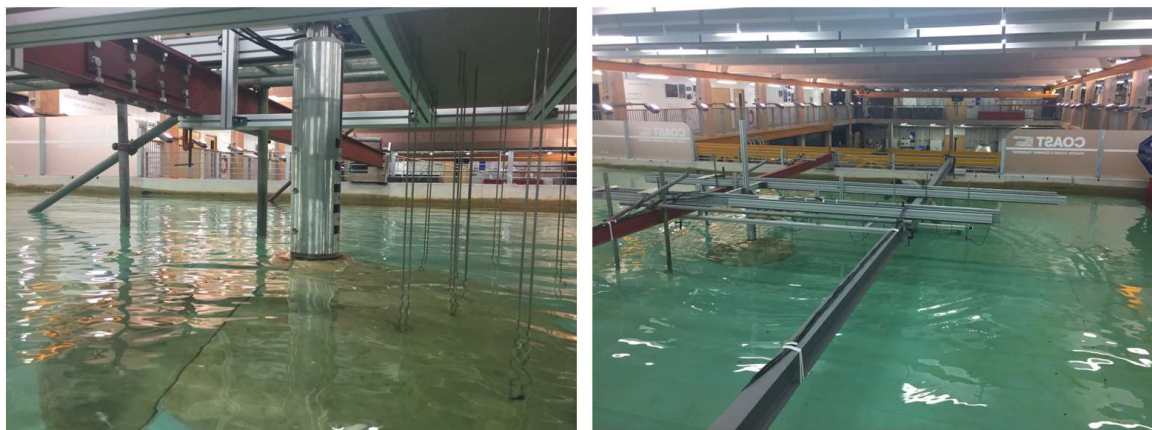


Figure 49: Photo of the model fixed with steel beams

For the wave profile recording, 13 wave gauges were place in front of the model. Precisely, 10 wave gauges were fixed to the shoal and 3 wave gauges were placed in line in front of the model and fixed to the bottom of the tank. A scheme is given in Figure 50.

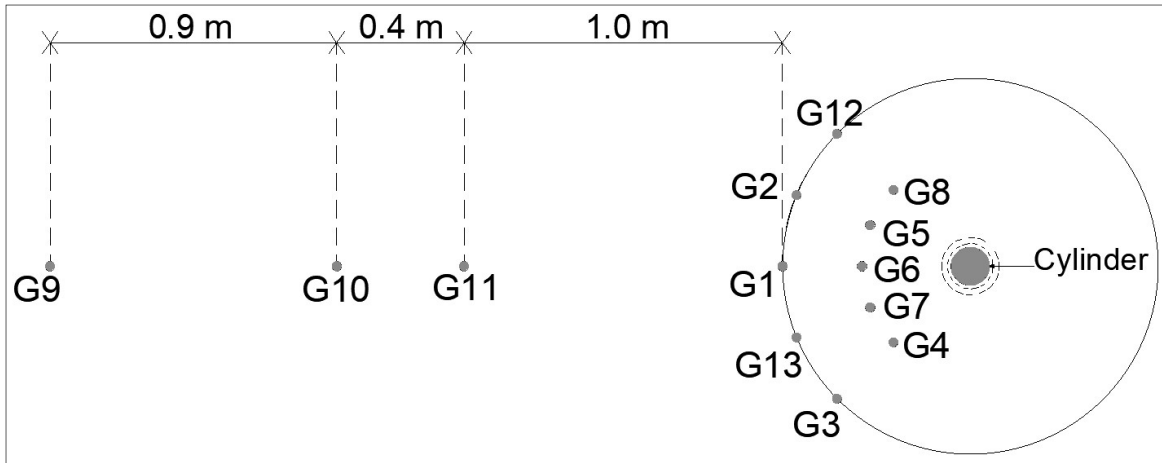


Figure 50: Wave gauges positioning scheme

The wave gauges provide an accurate wave profile record based on the measurement of electrical conductivity between two parallel rods, considering that the resistance between the rods is proportional to the immersion depth.

The wave gauges used had different characteristics, listed in

Wave Gauge	Length	Diameter
G1	1000 mm	4 mm
G2	1000 mm	4 mm
G3	1000 mm	4 mm
G4	700 mm	3 mm
G5	700 mm	3 mm
G6	700 mm	3 mm
G7	700 mm	3 mm
G8	700 mm	3 mm
G9	1000 mm	4 mm
G10	1000 mm	4 mm
G11	1000 mm	4 mm
G12	1000 mm	4 mm
G13	1000 mm	4 mm

Table 5: Wave gauges characteristics

The wave gauges were connected to a controller that sent all the information to a computer with a sample rate of 128 Hz. Some more pictures of the wave gauges installation are shown in the following figure.

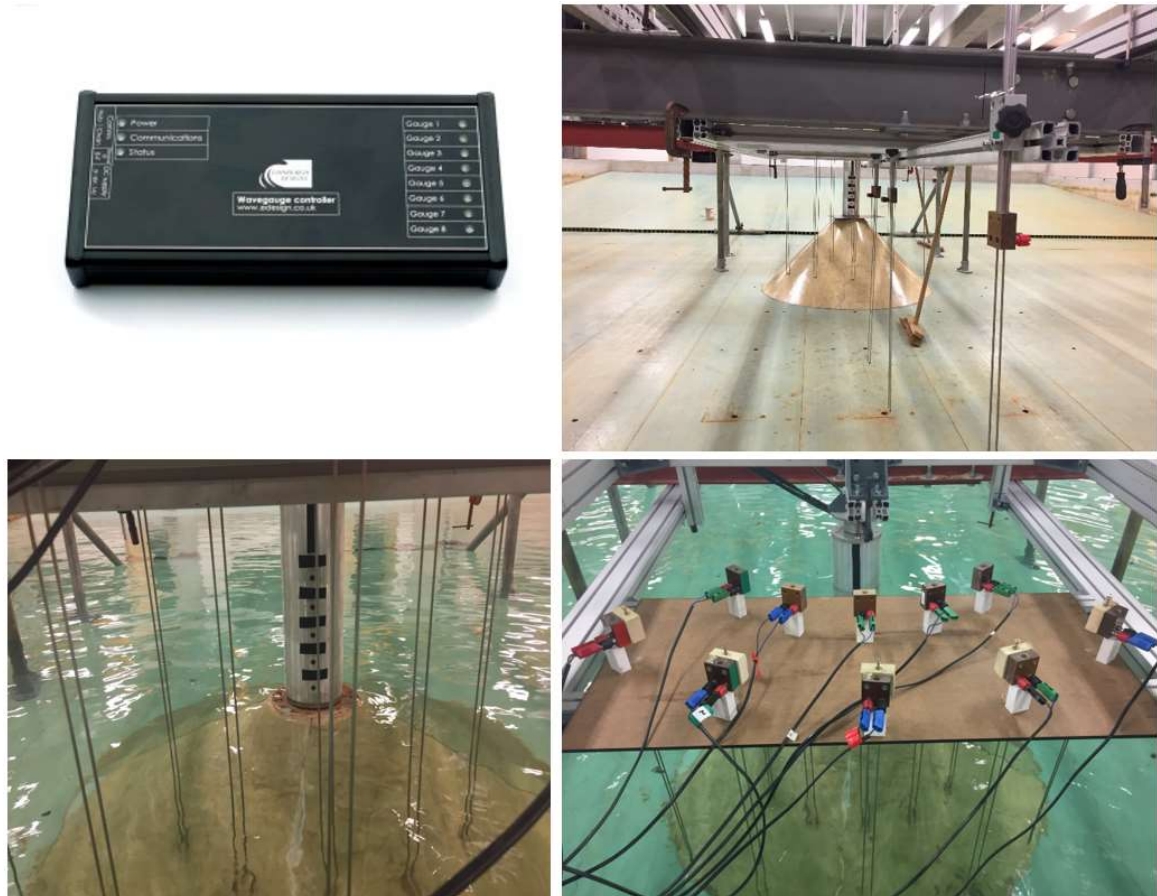


Figure 51: Photos of the wave gauges set-up

The load cell is another apparatus that had a fundamental role in the laboratory tests. A 6-Axis load cell measures forces simultaneously in 3 mutually perpendicular axes and 3 simultaneous torsions. Six full bridges provide mV/V output on 6 independent channels, thus a 36-term coefficient matrix allows to pass from V to N/Nm.

Reference	1	2	3	4	5	6
F_x in N/mV/V	-460.54	-7.23	463.09	459.99	1.13	455.95
F_x in N/mV/V	283.81	517.90	272.08	272.16	515.75	273.85
F_x in N/mV/V	-672.66	657.48	661.91	657.22	653.61	669.80
F_x in N/mV/V	17.69	-7.96	-9.34	-9.38	-7.88	17.38
F_x in N/mV/V	-1.31	-15.57	-15.64	13.65	13.80	-0.61
F_x in N/mV/V	-11.84	11.25	-12.07	11.83	-10.76	11.32

Table 6: Load cell calibration matrix

The load cell was fixed to the model head and consequently connected to the steel beam, thus the millimetre gap left between the model and the shoal allowed a correct measurement with the load cell.



Figure 52: Load cell installation above the model

For the analysis of the run-up on the model, a high speed camera has been used (Figure 53). It owns high performance CMOS sensor technology providing 3'600 fps operation at 1'024x1'024 pixel resolution and frame rate up to 500'000 fps at reduced resolution. After several attempts, a frame rate of 128 fps was set according to the light condition.



Figure 53: High speed imaging Fastcam SA4

Since the high speed camera was used for the analysis of the images and to obtain a run-up variation along the model, a geometric calibration has been necessary. The calibration consists in identifying the parameters of the lenses and the image sensors of the camera, then it is possible to correct the image distortion and provide a flat representation for geometric measurements. Camera parameters are intrinsic, extrinsic and distortion coefficients.

Thus for the calibration process, it has been necessary to compare some real points, therefore belonging to the three-dimensional space, to the same points identified by the camera in the two-dimensional representation space. This procedure was carried out by using a chessboard where the dimensions of a single square are known. Figure 54 shows one the frames obtained by the camera during the calibration.

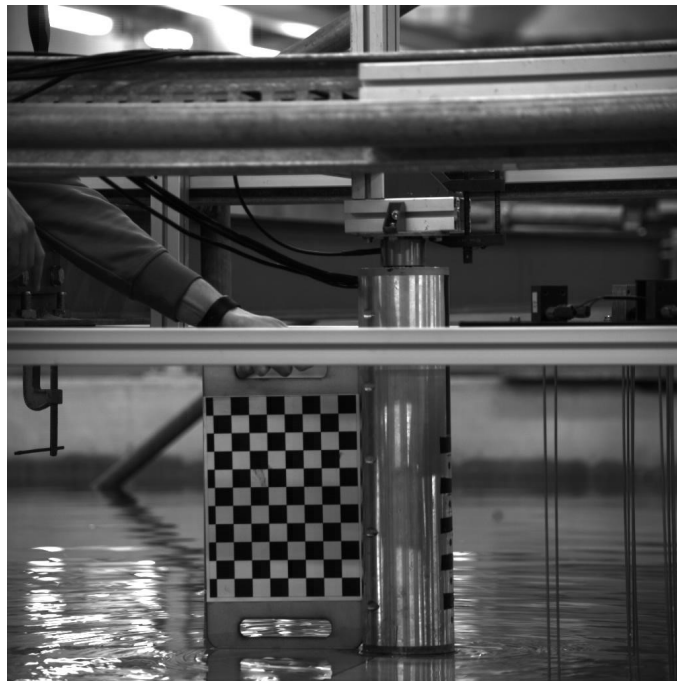


Figure 54: Frame of the calibration process with the chessboard

The Matlab calibration algorithm calculates the camera matrix using the extrinsic and intrinsic parameters. The extrinsic parameters represent a rigid transformation from the real three-dimensional coordinate system to the three-dimensional camera's coordinate system. The intrinsic parameters represent a projective transformation from the three-dimensional camera's coordinates into the two-dimensional image coordinates. The extrinsic parameters consist of a rotation, R , and a translation, t . The origin of the camera's coordinate system is at its optical center and its x - and y -axis define the image plane.

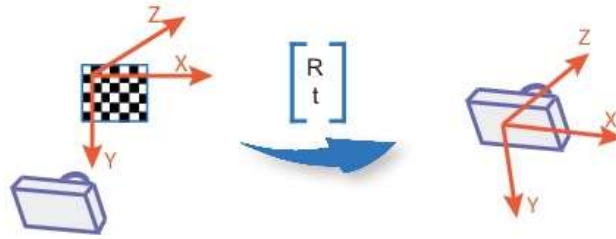


Figure 55: Intrinsic parameter transformation (Matlab)

The intrinsic parameters include the focal length, the optical centre, also known as the principal point, and the skew coefficient.

$$\begin{bmatrix} f_x & 0 & 0 \\ s & f_y & 0 \\ c_x & c_y & 1 \end{bmatrix}$$

Figure 56: Camera intrinsic matrix and pixel skew (Matlab)

where:

- $[c_x, c_y]$ – optical centre
- $[f_x, f_y]$ – focal length, $f_x = F/p_x$ and $f_y = F/p_y$
- F – focal length
- $[p_x, p_y]$ – size of the pixel
- s – skew coefficient, which is not zero if the axes are not perpendicular, $s = f_y \cdot \tan \alpha$

Subsequently, the radial and tangential distortions of the lenses were taken into account.



Figure 57: Radial and tangential distortion of the lenses (Matlab)

Radial distortion occurs when light rays bend more near the edges of a lens than they do at its optical center. The smaller the lens, the greater the distortion. The radial distortion coefficients model this type of distortion.

Points affected by radial distortion are indicated in equation [4.1].

$$\begin{aligned} x_{\text{distorted}} &= x(1 + k_1r^2 + k_2r^4 + k_3r^6) \\ y_{\text{distorted}} &= y(1 + k_1r^2 + k_2r^4 + k_3r^6) \end{aligned} \quad [4.1]$$

where:

- x and y – undistorted pixel locations, they are obtained by translating the optical center and dividing by the focal length in pixels so they are dimensionless
- k_1 , k_2 and k_3 – radial distortion coefficients of the lenses
- $r^2 = x^2 + y^2$

Tangential distortion occur when the lens and the image plane are not parallel. For this case, the tangential distorted points are indicated with the equation [4.2].

$$\begin{aligned} x_{\text{distorted}} &= x + [2p_1xy + p_2(r_2 + 2x_2)] \\ y_{\text{distorted}} &= y + [p_1(r_2 + 2y_2) + 2p_2xy] \end{aligned} \quad [4.2]$$

where:

- x and y – undistorted pixel locations
- p_1 and p_2 – tangential distortion coefficients of the lenses
- $r_2 = x_2 + y_2$

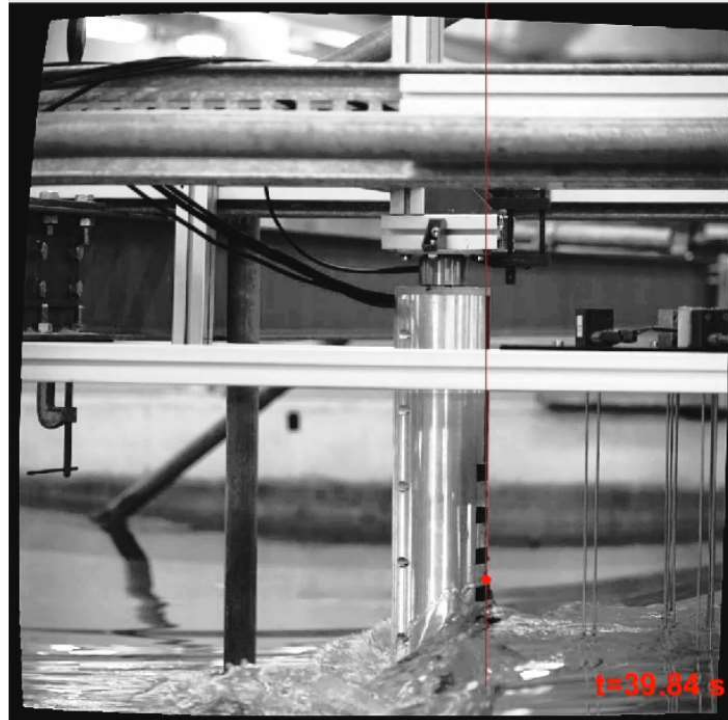


Figure 58: Undistorted frame with example of run-up on the model

Figure 58 represents a single undistorted frame where a run-up measurement were taken on the model.

4.1 Results

The tests in the laboratory were performed by varying some parameters that could significantly modify the behavior of the wave group and its interaction with the model.

According to the paragraph 3.3, a group of focused waves can be described as a sum of n sinusoidal waves that fluctuate with time (t) and space (x).

$$h(x, t) = \sum_n a_n \cos(k_n x - \omega_n t + \phi_n) \quad [4.3]$$

The phase of each individual component has been adjusted, so that the focus position had a pre-selected distance from the model. Moving away from the focus point, the amplitude and the frequency tend to decrease because of the consequent dispersion. Laboratory tests were based on four different focus positions.

ID	Description
Central Shelf	Cylinder axis
Toe Back Slope 0.5	0.5 meters after the back toe of the shoal
Toe Back Slope	Back toe of the shoal
Toe11	1 meter before the toe of the shoal

Table 7: Focus positions adopted for the tests

As already mentioned above, the spectra have been constructed according to the principles of the new wave theory but, precisely, referring to the Pierson-Moskowitz spectrum ($\gamma = 1$) and to the Jonswap spectrum ($\gamma = 3.3$). Figure 59 gives a comparison of the two spectrum parameters, especially in the third graph of each spectrum it is observable the difference in terms of propagation before and after the peak.

The first significant parameter is the *peak period* of the wave group, it has been modified according to five relevant values: 1.2 s, 1.5 s, 1.85 s, 1.96 s and 2.44 s. The significant wave height was a constant value of 0.246 m.

The tests were performed applying both a crest focus and a trough focus, although more attention was paid to the crest focus.

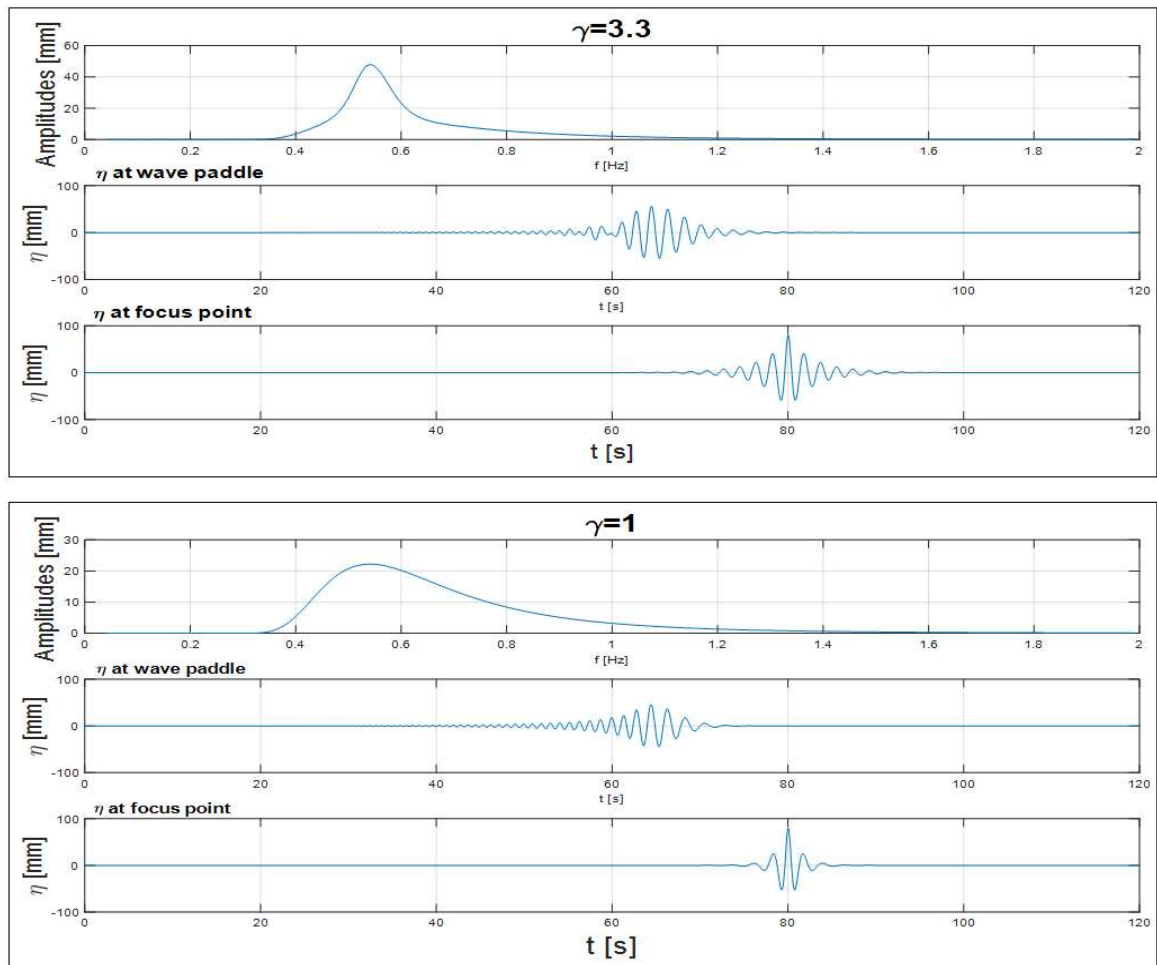


Figure 59: Comparison between Pierson-Moskowitz ($\gamma = 1$) and Jonswap spectrum ($\gamma = 3.3$)

Table 8 shows an example of the test plan made for the peak period of 1.2 seconds. Considering all the variables examined, the total amount of experiments carried out is 80 but further tests have been performed to verify the repeatability of the phenomena.

Test Name	Gamma	Peak Period	Wave Height	Focus Type	Focus Position
Run_1_1_n_01_3D	1	1.2	0.246	Crest	Central Shelf
Run_1_1_n_05_3D	1	1.2	0.246	Crest	Toe11
Run_1_1_n_09_3D	1	1.2	0.246	Crest	Toe Back Slope
Run_1_1_n_13_3D	1	1.2	0.246	Crest	Toe Back Slope 05
Run_1_1_n_01_phase180_3D	1	1.2	0.246	Trough	Central Shelf
Run_1_1_n_05_phase180_3D	1	1.2	0.246	Trough	Toe11
Run_1_1_n_09_phase180_3D	1	1.2	0.246	Trough	Toe Back Slope
Run_1_1_n_13_phase180_3D	1	1.2	0.246	Trough	Toe Back Slope 05

Table 8: Test plan for a peak period of 1.2 seconds

4.1.1 Wave Gauges and Run-Up

The wave gauges placed around the model (see Figure 50) allowed the analysis of wave propagation near the model. The incoming signal was initially corrected according to the application of a low-pass filter, then the propagation of the wave group has been analyzed in order to find the specific peak that causes the maximum run-up on the model. Figure 60 is an example of what has been obtained from the wave gauges 9, 10 and 11, which are the first three met by the wave group. It is possible to see clearly how the maximum peak is perceived as time passes, obviously the wave gauge 11 is the last one that perceives its effect because it is closer to the model.

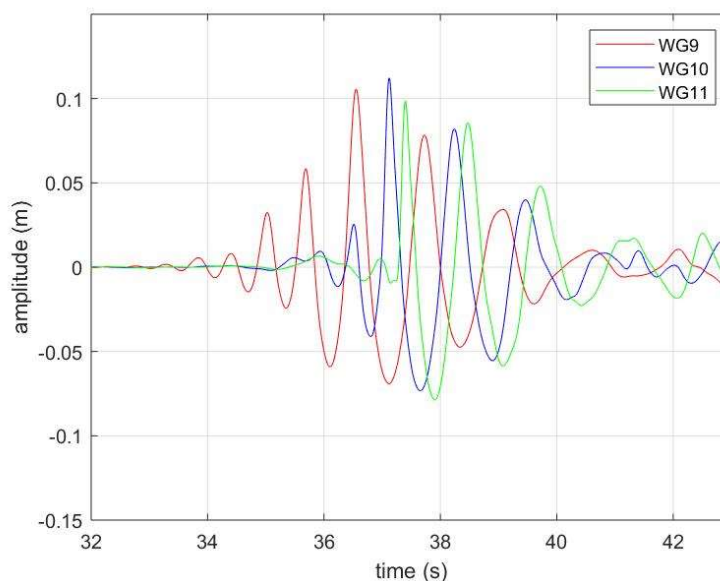


Figure 60: Comparison of wave-gauges data ($T_p = 1.2$ s, $\gamma = 1$, crest focus, central shelf)

At the same time, the images provided by the high-speed camera allowed an accurate analysis of the run-up on the model, being able to define its variation over the time and, particularly, the maximum values reached. As can be seen in Figure 61, the run-up varies with time presenting more than one peak; clearly, the maximum peak reached had a more significant role because it will be associated with the maximum force applied to the model.

Therefore, in this case, the wave gauge that played a fundamental role was the number 6, because it was the closest to the model. Starting from the variation of the water level recorded by the wave gauge 6, a comparison was made that could lead to define which peak generated the maximum run-up. This can be seen in Figure 62.

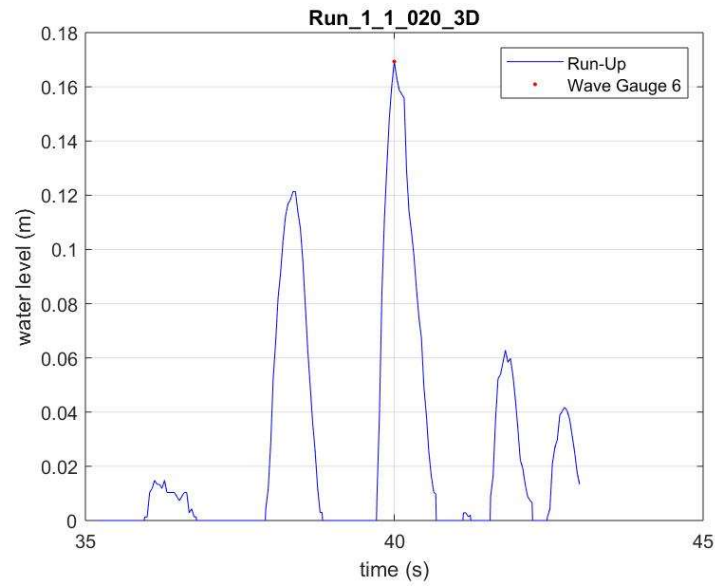


Figure 61: Run-up plot ($T_p = 1.96$ s, $\gamma = 1$, trough focus, toe11)

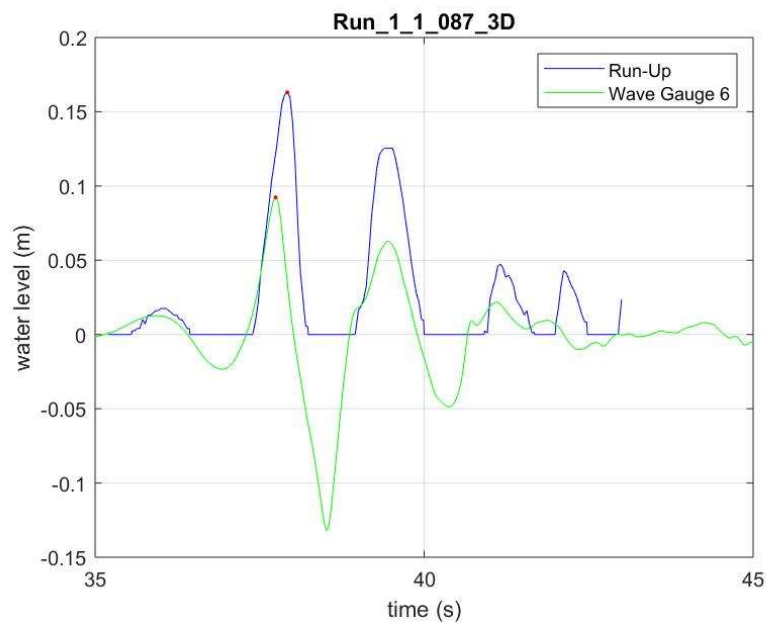


Figure 62: Comparison of run-up and WG6 ($T_p = 1.85$ s, $\gamma = 1$, trough focus, toe back slope)

This type of analysis allowed to evaluate the size of the run-up as a function of the wave group. In fact, as can be seen in Figure 62, the variation of the water level recorded by the wave gauge is very close to the run-up variation recorded on the model as well as the amplitude difference between the single peak of water level and run-up remains almost constant regardless of the amplitude.

The values obtained from the wave-gauge 6, which is the closest to the model, have been compared to the maximum run-up measured. Thus, the graph of Figure 63 has been gained.

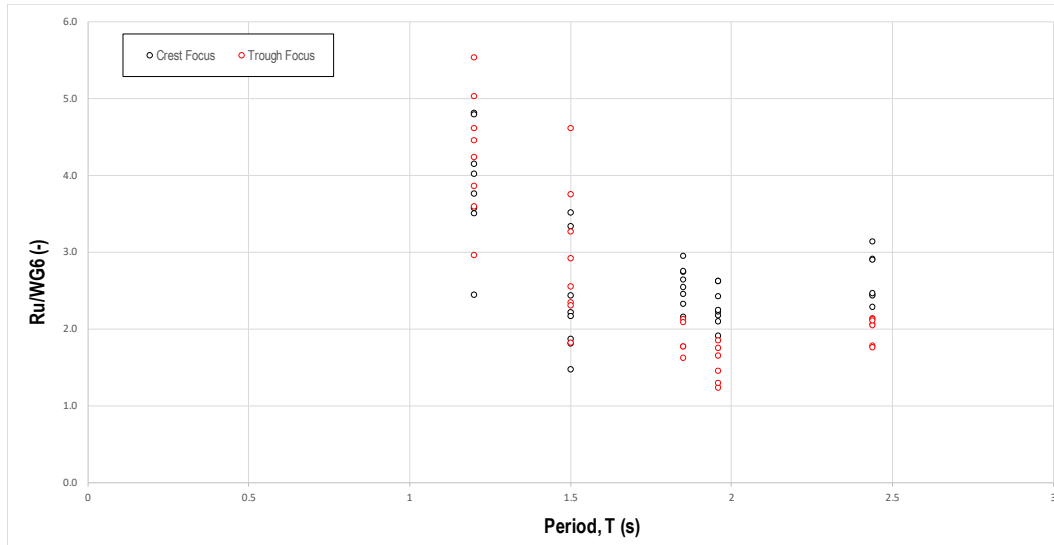


Figure 63: Comparison between run-up and wave gauge 6 against peak period

The comparison between the results shows how the intensity of the run-up tends to decrease when the period increase, this does not happen with the peak period of 2.44 s where a slight increase is obtained. This behaviour is not easy to analyse and deserves further investigations. Furthermore, it can be seen how the first two peak periods, 1.2 s and 1.5 s, the results given by the crest focus and the trough focus appear to be well mixed together without showing any particular difference. At the same time, the other three peak period appears to be separated in the middle and greater values are reached with the crest focus.

The analysis of the run-up also aimed the comparison of the results at the equation given by L. De Vos et al. (2007), which offers a mathematical relationship between run-up and wave velocity.

$$RU_{\max} = \eta_{\max} \cdot 4.45 \frac{u^2}{2g} \quad [4.4]$$

The results of the previous two-dimensional experiment seemed to better agree with the mentioned equation, confirming its validity for that case. It doesn't happen with the three-dimensional test, probably because of the effects that could not be taken into account previously. It should also be considered that in the two-dimensional analyses the trough focus was not treated, which, in this case, has a significant consequence on the arrangement of the points in the graph. To verify the expression mentioned above, the maximum run-up has been divided by the maximum wave height, given by the wave gauge 6, and compared to the ratio h/L_p (h : water depth; L_p : peak wavelength).

The following diagram (Figure 64) shows the result after the first test, where only the two-dimensional effects were considered.

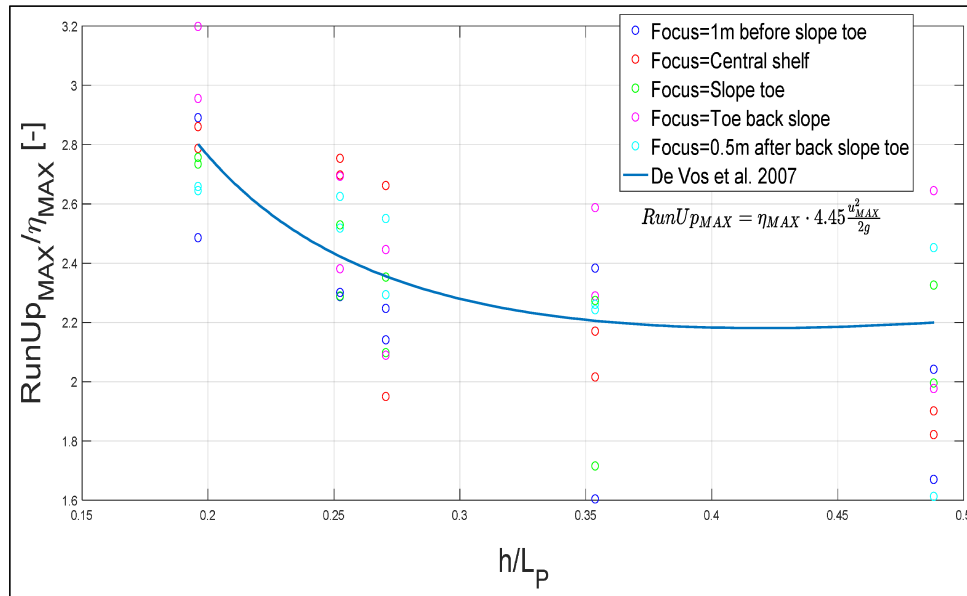


Figure 64: Run-up/maximum wave crest high vs water depth/peak wave length (2D)

The arrangement of the points in the graph seems to follow the function provided by L. De Vos et al. (2007).

Figure 65 shows the results obtained with the new tests in the tank, where the three-dimensional effects are dominant. The decreasing trend proposed by the equation [4.4] is almost completely lost.

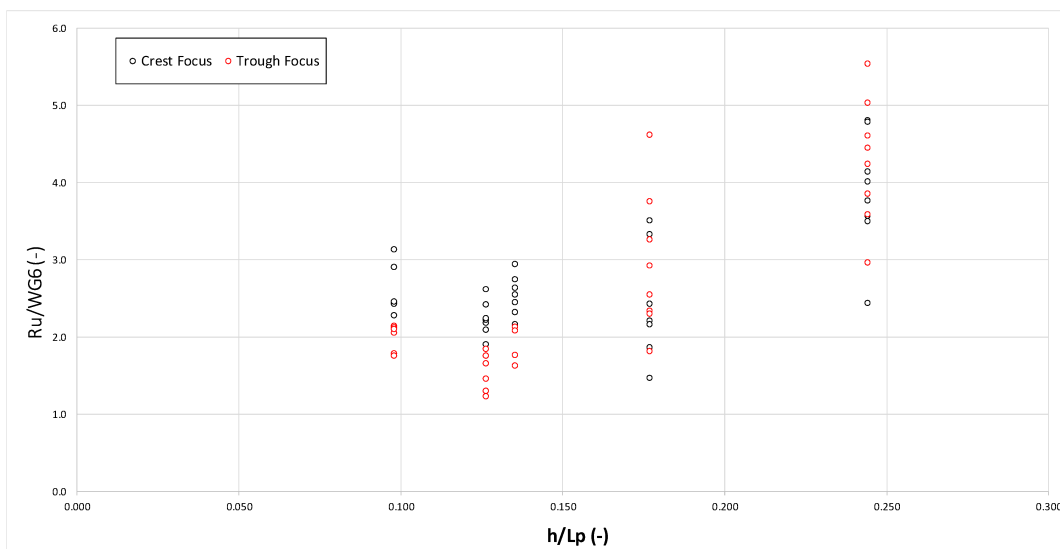


Figure 65: Run-up/maximum wave crest high vs water depth/peak wave length (3D)

4.1.2 Forces and Load Distribution

The analysis of the forces is made by the load cell described in the paragraph 4.0 and an image is given in Figure 52. It allowed the measurement of the forces along the three axes and the torsions around them. The results will be presented in the following paragraph according to some graphical representations against some main parameters that cause a significant variation.

Figure 66 is a comparison between the values provided by a wave gauge and the force F_y , or bending moment M_x , recorded by the load cell for a specific run (Run_n_01, see Table 8 for more information). In the x-axis the frequency is used as a comparison parameter.

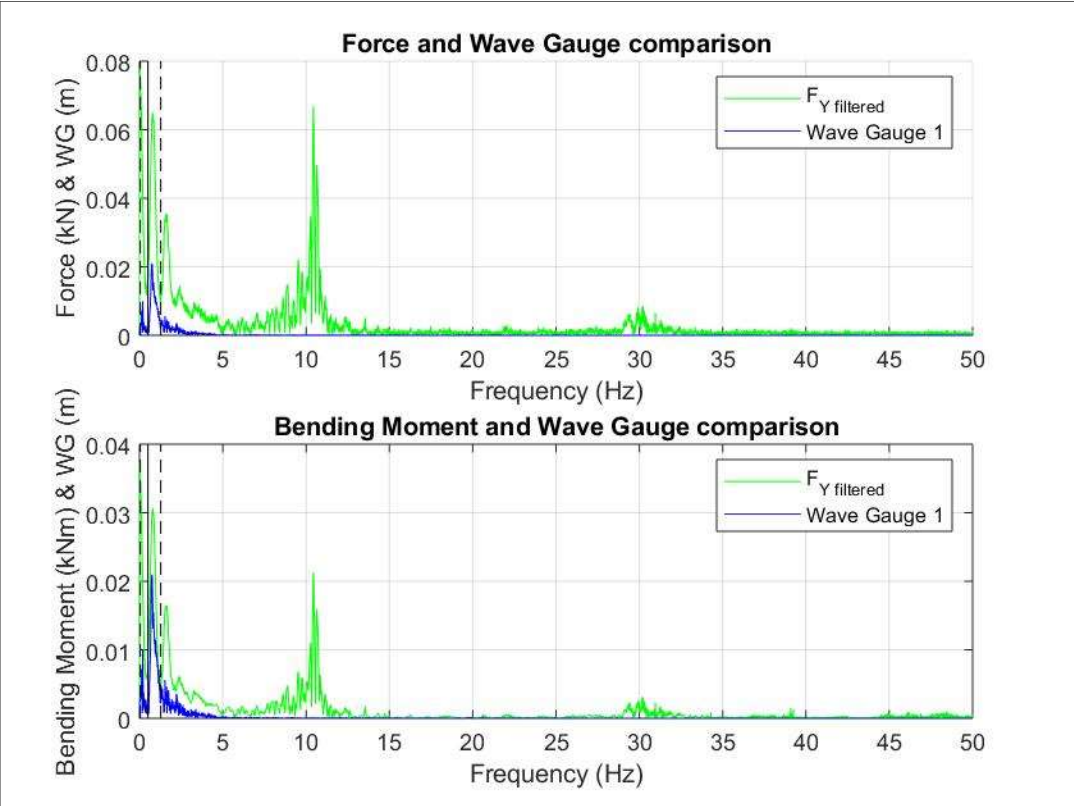


Figure 66: Run_n_01, force/moment and wave gauge against frequency

The two dashed lines represent the frequency range within the wave had been generated and it is obviously different for every run. Therefore, it is expected that everything which falls outside the range is due to “noise” or, better said, to the response of the structure. If the structure is perfectly stiff, as supposed in theory, its response must be identical to the force applied on it. The values given by the wave gauge can be seen as a single impulse concentrated in the middle of the dashed lines range. Since in reality the structure of the

model is not less rigid than it has been supposed, the response is also composed of other components on higher frequencies.

The two peaks at the frequencies of 10 Hz and 30 Hz are due to the free oscillations of the structure.

The diagram shown in Figure 67 is a simple comparison between the measurements given by the wave gauge 9 and the forces recorded with the load cell.

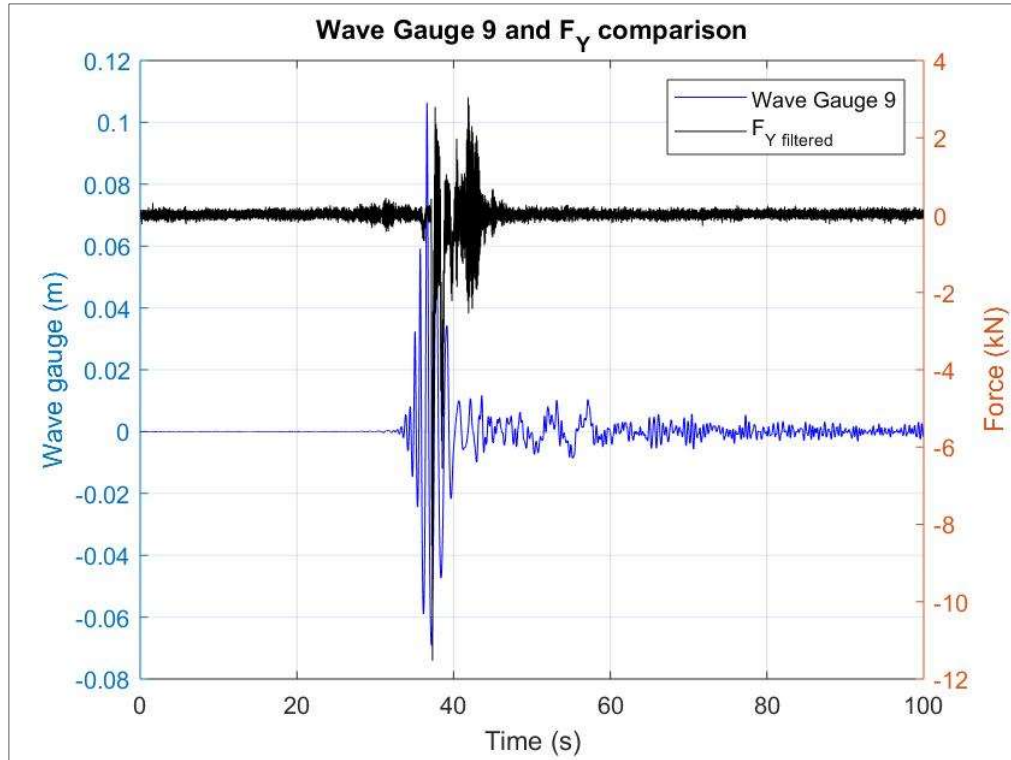


Figure 67: Run_n_01, wave gauge and force comparison

Thus, it is possible to notice the overlap of the two diagrams at almost their peaks. This is fully justified because the peak of wave amplitude is expected to correspond to a peak of force in the model. Actually, the two peaks are not perfectly superimposed because the wave gauge taken as reference is the most distant from the model.

Moreover, it is good to point out that the forces were examined after a preliminary correction. A low-pass filter of 10 Hz has been applied that could remove most of the noise recorded. The choice fell on this frequency value because, after several attempts, it shows sufficiently accurate results. An example is immediately visible in Figure 68 where the effects of the correction are shown both on the force F_y and on the bending moment M_x . The force F_y more conveyed the correction applied.

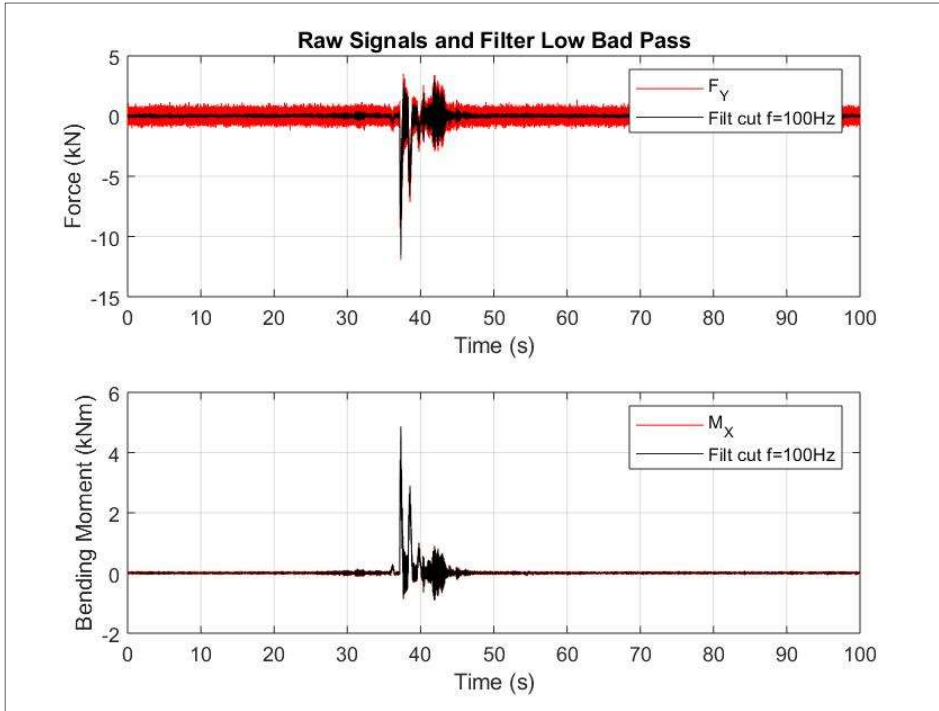


Figure 68: Run_n_01, correction applied on the force and bending moment

The signal recorded for each run has been analysed according to the theory of the Hilbert-Huang Transformation (HHT) described in the paragraph 3.4. Hence, Figure 69 is the result of the decomposition for the run 'Run_n_01'.

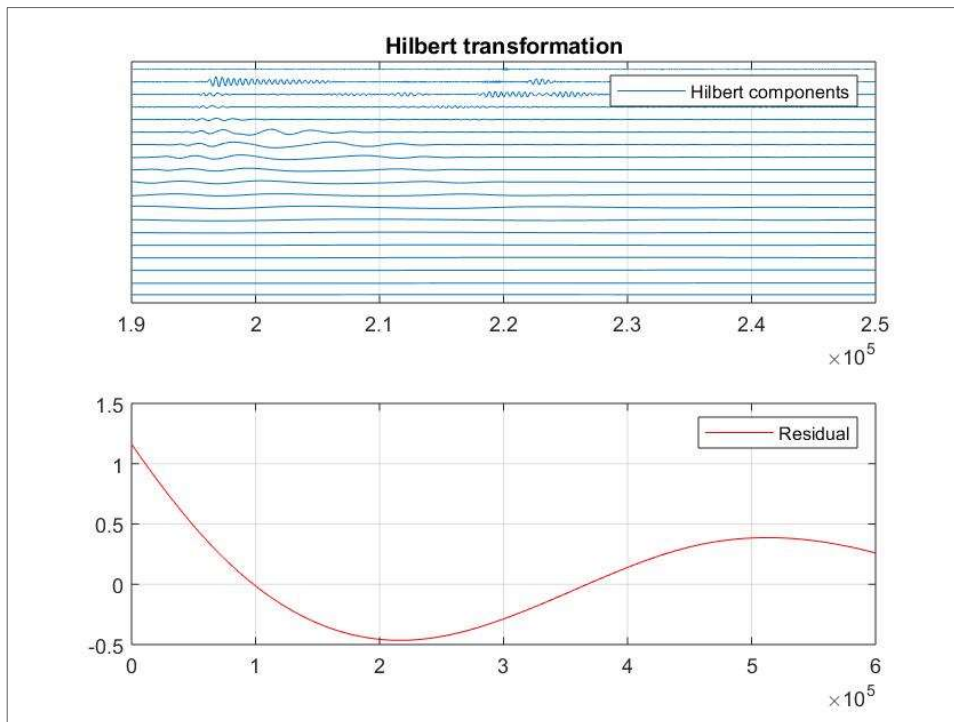


Figure 69: Run_n_01, components of the Hilbert transformation and residual signal

Note that, according to the HHT theory, a signal can be decomposed into a set of signals with an associated frequency. Therefore, the first graph is the representation of the first nineteen frequencies extracted, starting from the highest to the lowest. The second graph, instead, contains the residual signal and purified of the first frequencies.

After having performed the analysis of the spectra that make up the entire signal generated and perceived by the load cell, the analysis has been refined in order to isolate main frequencies and cancel the noise.

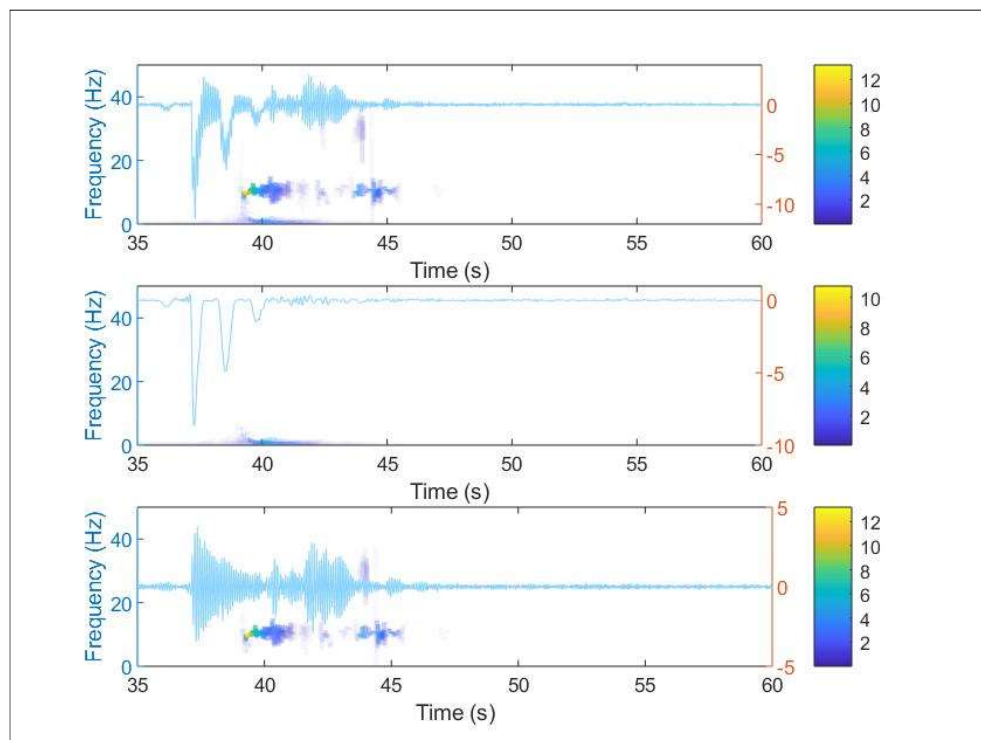


Figure 70: Run_n_01, signal decomposition according to the HHT (first attempt)

Each graph of Figure 70 can be seen as a set of one x-axis (time, in seconds) and three y-axes. The right y-axis refers to the raw signal of the forces, substantially their intensity, and its representation is the blue line above all. The left y-axis refers to the other coloured lines. The main information that is given is, basically, the indication of which exact frequency is stimulated at a specific instant of time. For example, in the first graph after almost 44 seconds both the low frequencies and high frequencies are stimulated, around about 10 Hz and 30 Hz. The third y-axis, described with a colour variation, gives the intensity of the signal at a specific instant in terms of energy.

The two graphs below are based on the same principles and they provide a representation of the signal purified from the low frequencies components, that can be associated to

external noise sources. The second graph, for example, provides the raw signal starting from the fifth Hilbert transformation, so avoiding the lowest frequencies. The last graph gives a representation of the components discarded in the previous graph, thus it is possible to notice the lines at the frequency of 10 Hz after almost 38 seconds.

In order to appreciate which components of the Hilbert transformation could better describe the signal, several attempts have been made. Figure 71 gives an example of a second attempt, in fact the second chart contains the sum of all components excluding only the first three and not the first four as done before. The best result seems to be the first one given in Figure 70, because in the second attempt it is possible to notice that some frequencies around 10 Hz were solicited after almost 43 seconds.

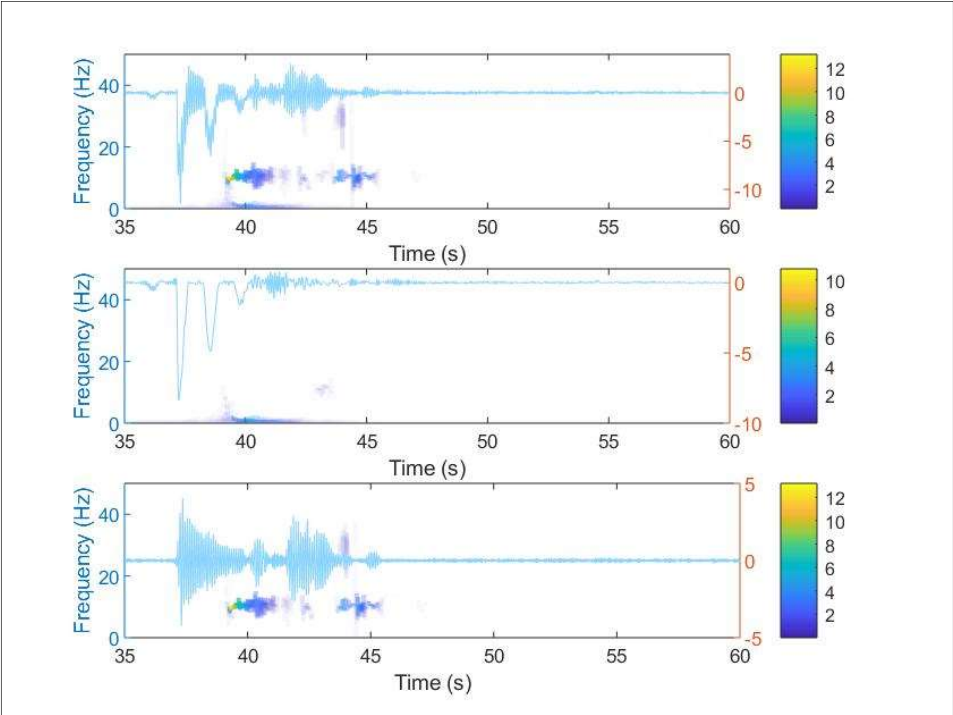


Figure 71: Run_n_01, signal decomposition according to the HHT (second attempt)

For the comparison of the results obtained with the low-pass filter initially and the HHT subsequently, a new diagram has been realised. Figure 72 is an example of what has been found. In this way, it is possible to clearly see the difference between the raw signal obtained by the simple application of the low-pass filter and the theory of Hilbert transformations.

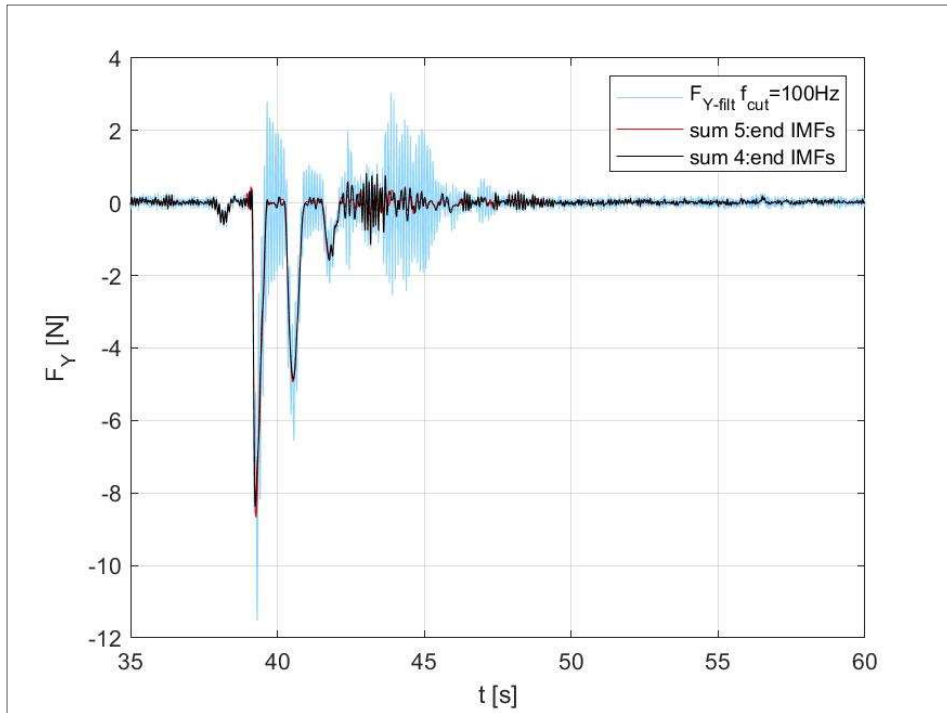


Figure 72: Run_n_01, comparison after the correction of the raw signal

CHAPTER V: CONCLUSIONS

This project covered several topics, it started with a statistical analysis of the wave conditions that characterised the examined area to conclude with the effects of the extreme wave groups that act on the lighthouse.

In chapter II, 'Wave Climate', the analysis have brought significant results although only omni-directional significant wave-heights were considered. However, it is important to point out that the wave period and direction also have an important role in wave loads. Caires and Van Gent (2008) studied a method of analysing the extreme wave values where the wave period can be taken into account. Therefore, an improvement of the analysis of the wave climate is recommended in any future studies.

According to Figure 65, the run-up values obtained perfectly follows the expectations. As shown by De Vos et al. (2007), the run-up is strongly influenced by the wave steepness (H/L_p); when the wave steepness increases, the run-up increases too. Thus, under swell sea condition, i.e. long waves coming from the ocean, the run-up could reach very high values while for short and chaotic waves the run-up has lower values. This behaviour is not perfectly showed by all tests performed, in particular the test referred to the period 2.44 seconds tends to deviate from the rest. It can be due to a possible reflection effect inside the tank. Another example is shown in Figure 63, where it is strongly evident the different trend of the highest period.

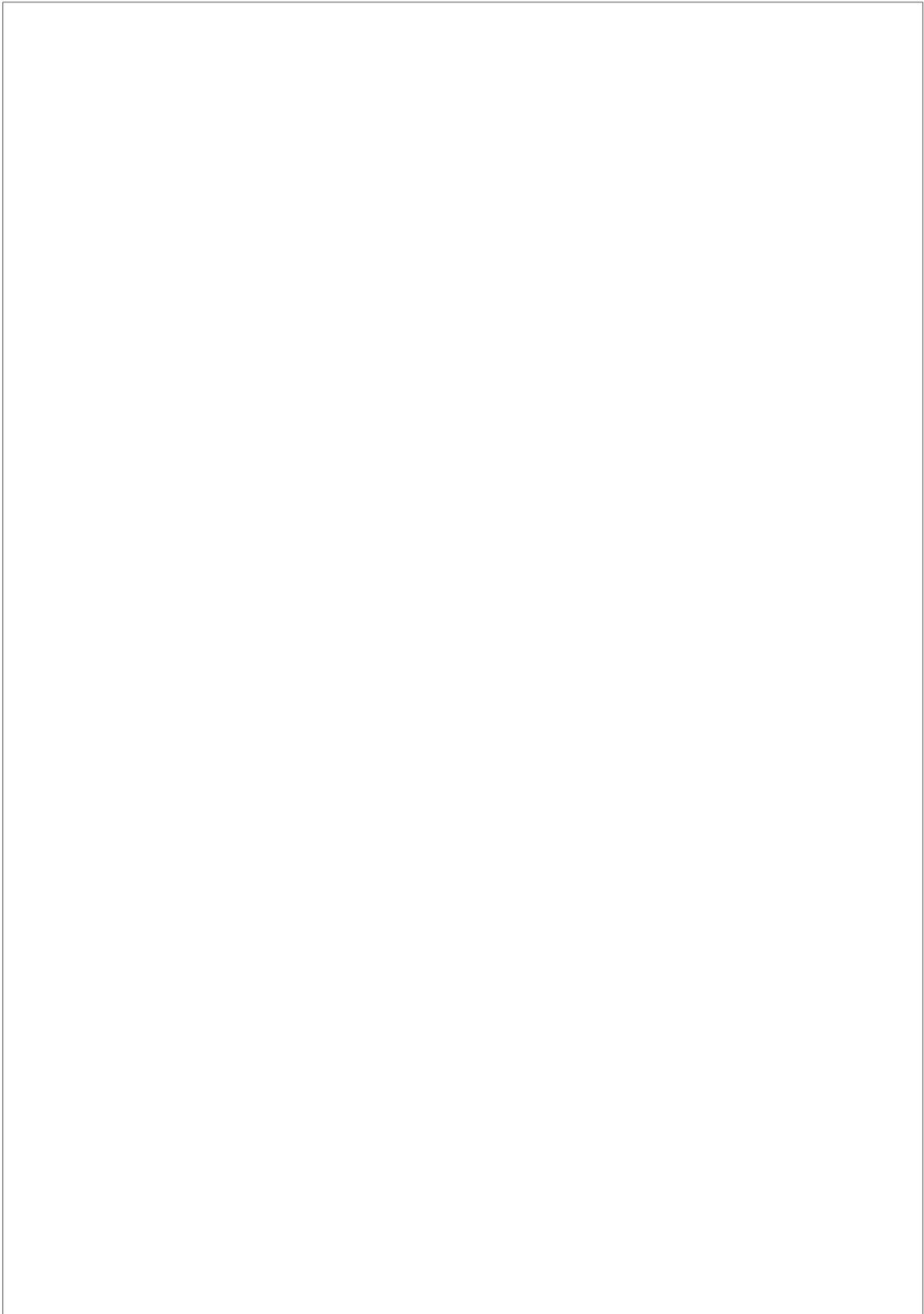
The methodology adopted for the run-up measurements has proved to be effective for this tests, but it deserves improvements. Many steps have been performed manually so it is advisable to conduct future studies with automatized procedures.

The forces analysis deserves further and future studies in order to define their variability according to the main parameters, such as: peak period, focus distance and time. the applied method showed a good applicability and an effective calculation methodology.

Bearing in mind that the present experimentation has been elaborated after an antecedent research project (see "Hydrodynamic loading and structural dynamic assessment of an offshore lighthouse", Piermodesto Caputo, 2018), the results obtained by comparing the two experiments showed some discrepancies that deserve further studies and analysis.

APPENDIX A: MATLAB CODES

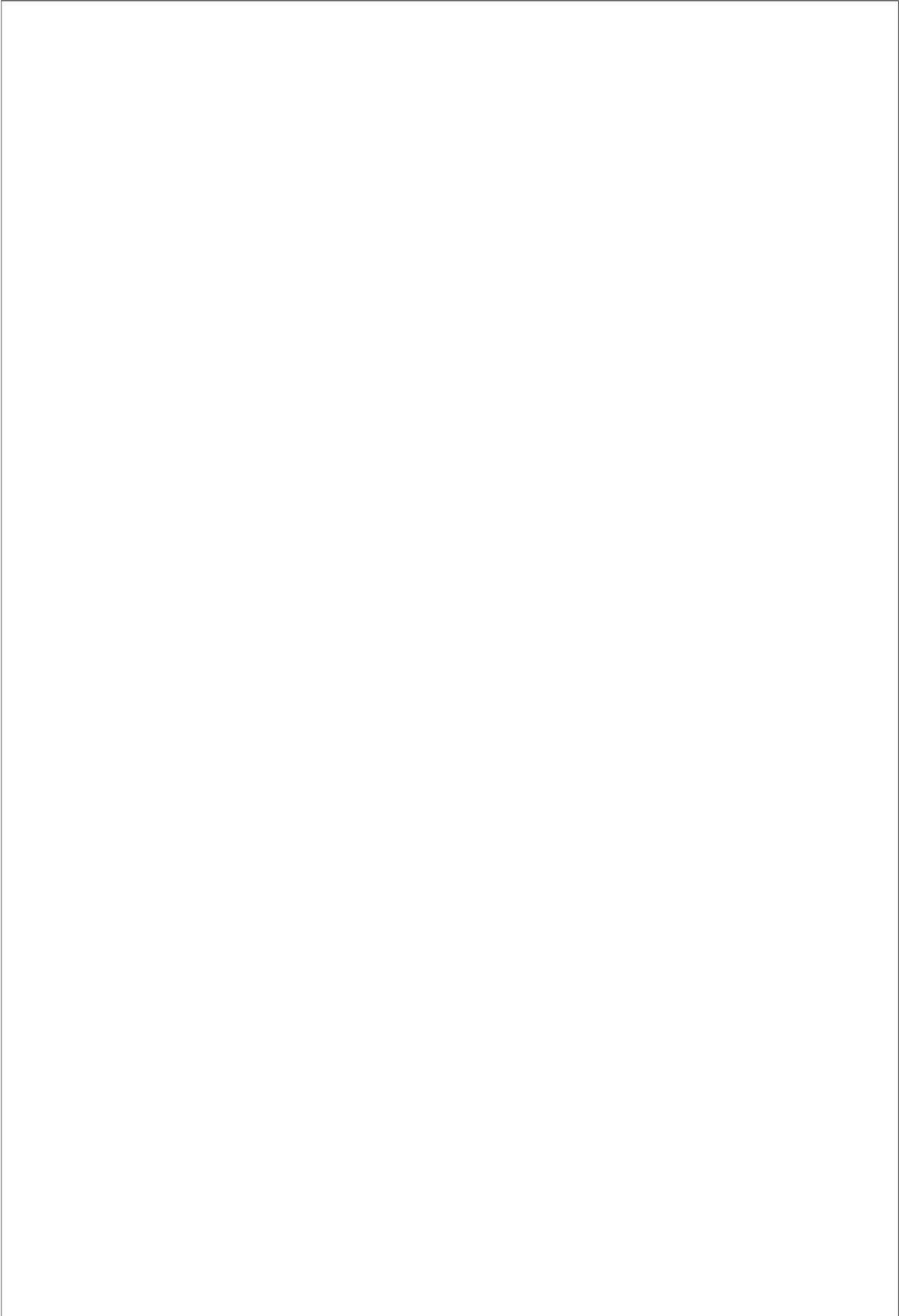
Wave gauge and run-up analysis

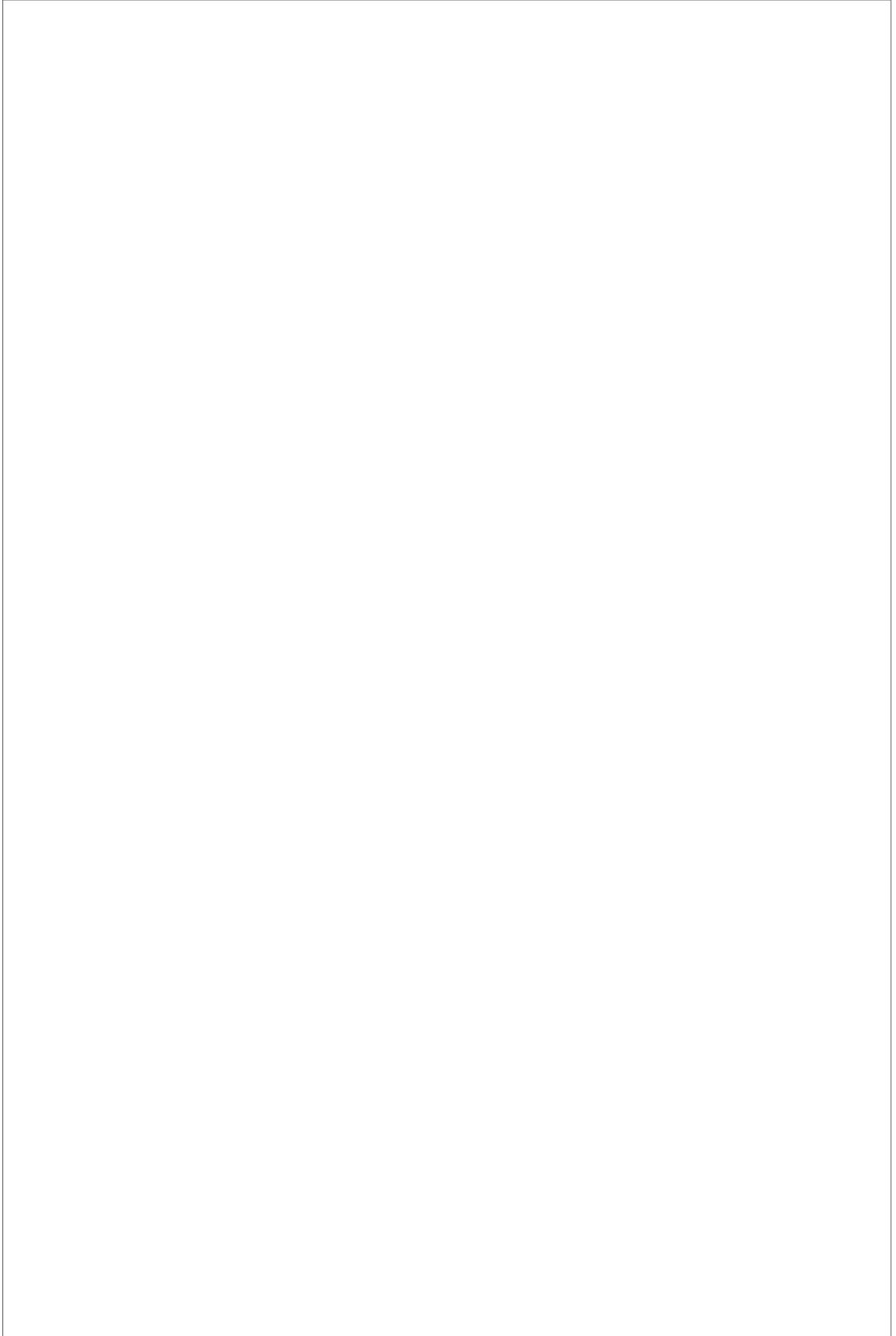




Forces analysis





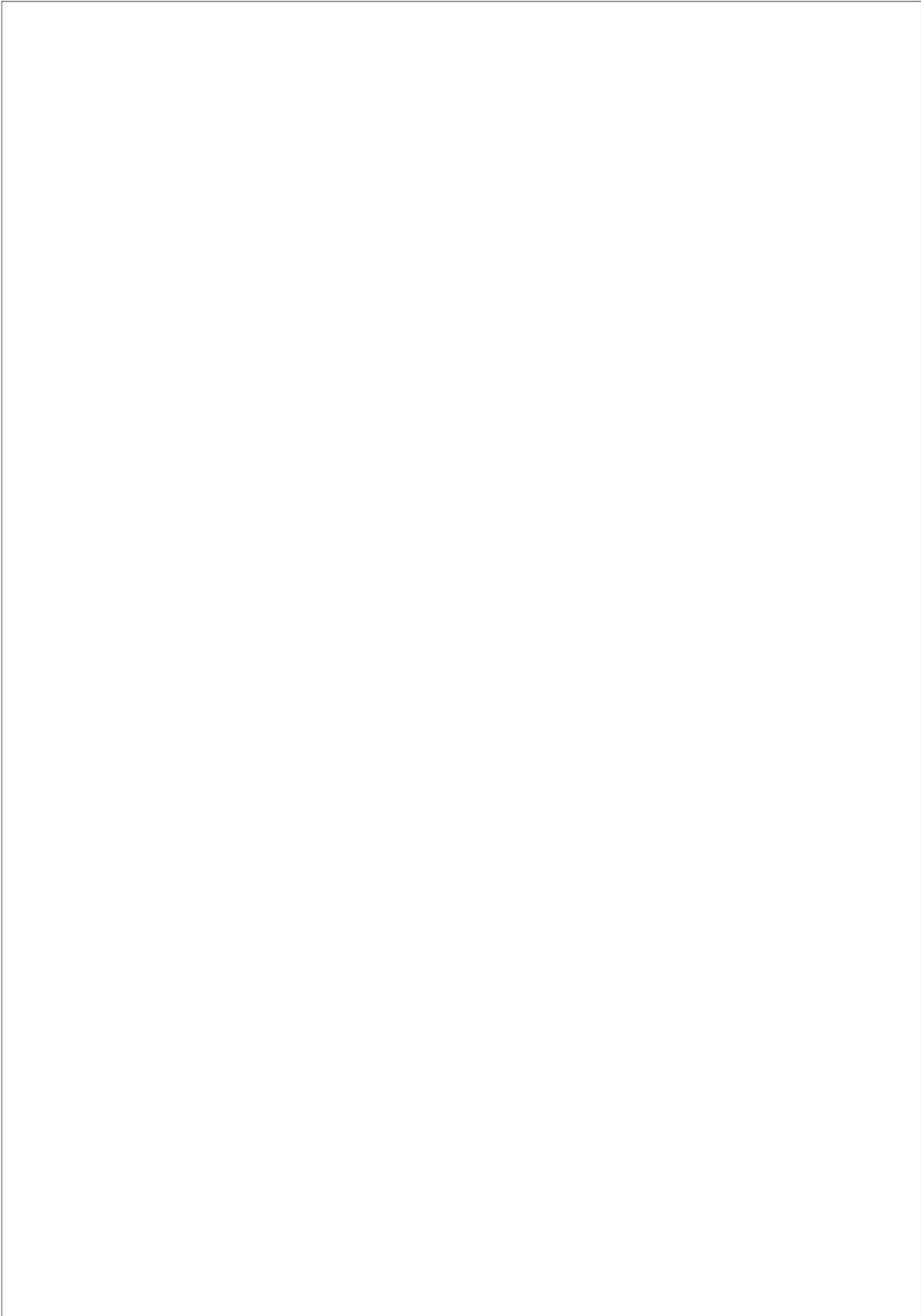




EVA Analysis (1)

A large, empty rectangular box with a thin black border, occupying most of the page. It is intended for the user to perform an EVA (Economic Value Added) analysis.

EVA Analysis (2)



REFERENCES

- Atzeni, A. (2011). *Dispense di Idraulica Marittima*. Roma: Aracne Editrice.
- Boudière, E., Maisondieu, C., Ardhuin, F., Accensi, M., Pineau-Guillon, L., & Lepasqueur, J. (2013). A suitable metocean hindcast database for the design of marine energy converters.
- Boudière, E., Maisondieu, C., Ardhuin, F., Accensi, M., Pineau-Guillon, L., & Lepasqueur, J. (2013). A suitable metocean hindcast database for the design of Marine energy converters. *International journal of marine energy*, e40-e52.
- Caires, S. (2011). *Extreme Value Analysis: Wave Data*. JCOMM Technical Report No. 57.
- Coles, S. (2001). *An Introduction to Statistical Modeling of Extreme Values*. London: Springer-Verlag.
- Collados, X. (2011). Impact forces on a vertical pile from plunging breaking waves.
- Dean, R., & Dalrymple, R. (2008). *Water Wave Mechanics for Engineers and Scientists*. World Scientific.
- Fabula, A. (1957). *Ellipse fitting approximation of two-dimensional normal symmetric impact of rigid bodies on water*.
- Far, S. S., & Ahmad Kahiri, A. (2016, July 7). *Evaluation of Peaks-Over-Threshold Method*. Retrieved from <https://www.ocean-sci-discuss.net/os-2016-47/os-2016-47.pdf>
- Ferreira, J. A., & Guedes Soares, C. (1998). An application of the Peaks Over Threshold method to predict extremes of significant wave height. *Journal of Offshore Mechanics and arctic Engineering*, 120.
- Ferreira, J., & Guedes Soares, C. (1998). An application of the Peaks Over Threshold method to predict extremes of significant wave height.
- Galvin, C. (1982). *Environment in Coastal Engineering: definitions and examples*.
- Gavin, H. (2016). *Vibration of Single Degree of Freedom*. Fall.
- Goda, Y. (1973). A new method of wave pressure calculation for the design of composite breakwaters.

- Hamill, L. (2001). *Understanding Hydraulics*. Palgrave.
- Huang, N., & Shen, S. (2014). *Hilbert-Huang Transform and Its Applications*. Singapore: World Scientific Publisher Co. Pte. Ltd.
- Luceño, A. (2006). Fitting the generalized Pareto distribution to data using maximum goodness-of-fit estimators.
- Matlab. (n.d.). *Camera Calibration tool*. Retrieved from <https://it.mathworks.com/help/vision/ug/camera-calibration.html#buvr2qb-1>.
- McCormick, M. (2010). *Ocean Engineering Mechanics*. Cambridge.
- Nicholson, C. (1988). *Rock Lighthouses of Britain*. Patrick Stephens, Cambridge.
- Novak, P., & al., e. (2010). *Hydraulic Modelling - an Introduction*. Oxon: Spon Press.
- Raby, A., & et al. (2015). Wave Loading on Rock Lighthouses. 14.
- Reeve, D., Chadwick, A., & Fleming, C. (2004). *Coastal engineering: processes, theory and design practice*.
- Tromans, P., Anaturk, A., & Hagemeyer, P. (1991). A new model for the kinematics of large ocean waves - Application as a design wave. *Research Gate*.
- Vaidya, A. M. (n.d.). *Waves & Wave Structure Interaction*.
- Wienke, J., & Oumeraci, H. (2005). Breaking wave impact force on a vertical and inclined slender pile, theoretical and large-scale model investigations.